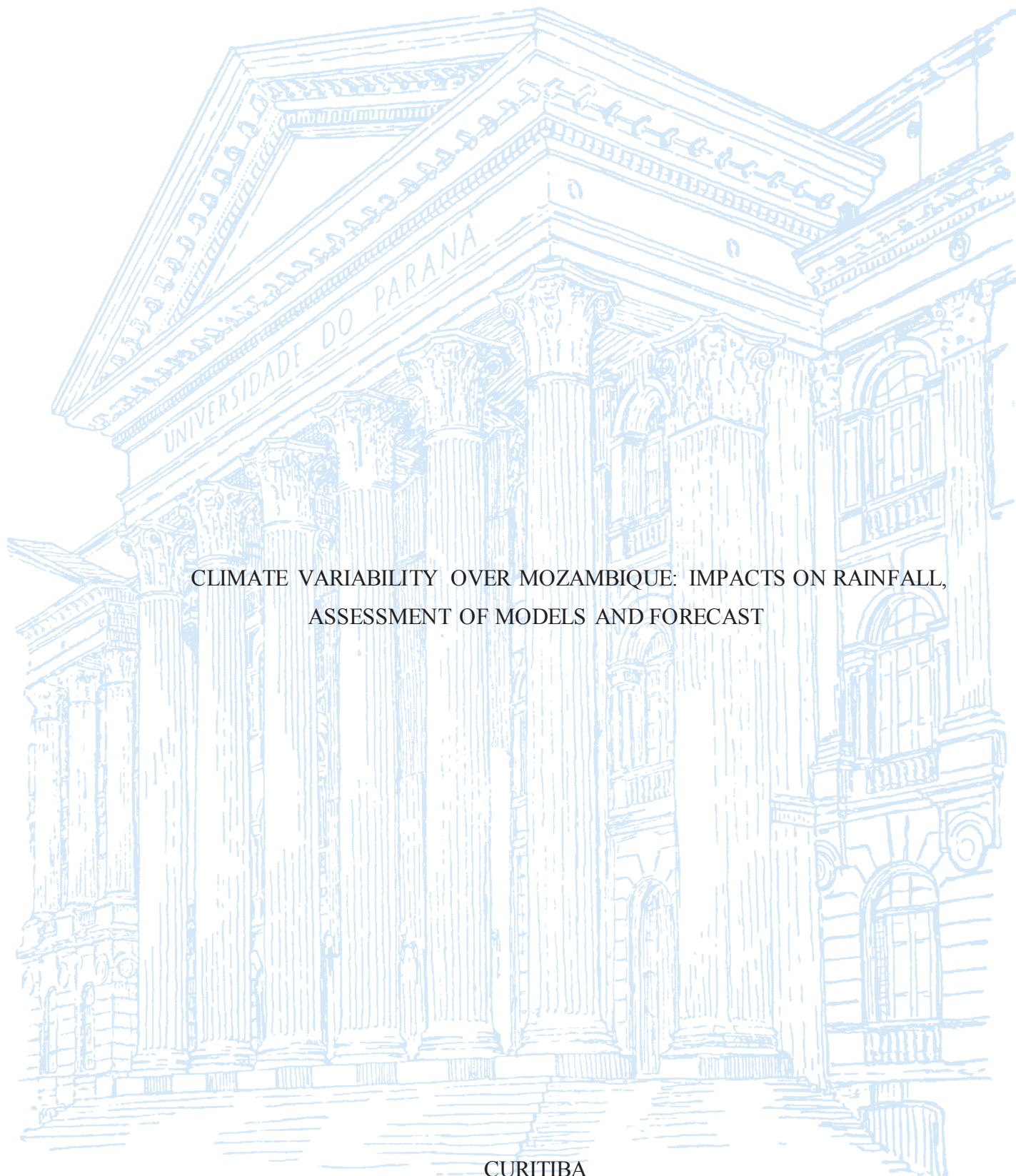UNIVERSIDADE FEDERAL DO PARANÁ

KÉNEDY CIPRIANO SILVÉRIO

CLIMATE VARIABILITY OVER MOZAMBIQUE: IMPACTS ON RAINFALL,
ASSESSMENT OF MODELS AND FORECAST

CURITIBA

2020

KÉNEDY CIPRIANO SILVÉRIO

CLIMATE VARIABILITY OVER MOZAMBIQUE: IMPACTS ON RAINFALL, ASSESSMENT OF MODELS AND FORECAST

Tese apresentada ao curso de Pós-Graduação em Engenharia de Recursos Hídricos e Ambiental, Setor de Ciência e Tecnologia, Universidade Federal do Paraná, como requisito parcial à obtenção do título de Doutor em Engenharia de Recursos Hídricos e Ambiental.

Orientadora: Profa. Dra. Alice Marlene Grimm

CURITIBA

2020

ATA Nº52

ATA DE SESSÃO PÚBLICA DE DEFESA DE DOUTORADO PARA A OBTENÇÃO DO GRAU DE DOUTOR EM ENGENHARIA DE RECURSOS HÍDRICOS E AMBIENTAL

No dia tres de junho de dois mil e vinte às 13:30 horas, na sala Plataforma Jitsi, Remoto, foram instaladas as atividades pertinentes ao rito de defesa de tese do doutorando **KÉNEDY CIPRIANO SILVÉRIO**, intitulada**: VARIABILIDADE CLIMÁTICA EM MOÇAMBIQUE: IMPACTOS NA CHUVA, AVALIAÇÃO DE MODELOS E PREVISÃO**, sob orientação da Profa. Dra. ALICE MARLENE GRIMM. A Banca Examinadora, designada pelo Colegiado do Programa de Pós-Graduação em ENGENHARIA DE RECURSOS HÍDRICOS E AMBIENTAL da Universidade Federal do Paraná, foi constituída pelos seguintes Membros: ALICE MARLENE GRIMM (UNIVERSIDADE FEDERAL DO PARANÁ), CAIO AUGUSTO DOS SANTOS COELHO (INSTITUTO NACIONAL DE PESQUISAS ESPACIAIS), ELOY KAVISKI (UNIVERSIDADE FEDERAL DO PARANÁ), MANOEL ALONSO GAN (INSTITUTO NACIONAL DE PESQUISAS ESPACIAIS), DANIEL HENRIQUE MARCO DETZEL (UNIVERSIDADE FEDERAL DO PARANÁ), ALEXANDRE KOLODYNSKIE GUETTER (UNIVERSIDADE FEDERAL DO PARANÁ). A presidência iniciou os ritos definidos pelo Colegiado do Programa e, após exarados os pareceres dos membros do comitê examinador e da respectiva contra argumentação, ocorreu a leitura do parecer final da banca examinadora, que decidiu pela APROVAÇÃO. Este resultado deverá ser homologado pelo Colegiado do programa, mediante o atendimento de todas as indicações e correções solicitadas pela banca dentro dos prazos regimentais definidos pelo programa. A outorga de título de doutor está condicionada ao atendimento de todos os requisitos e prazos determinados no regimento do Programa de Pós-Graduação. Nada mais havendo a tratar a presidência deu por encerrada a sessão, da qual eu, ALICE MARLENE GRIMM, lavrei a presente ata, que vai assinada por mim e pelos demais membros da Comissão Examinadora.

CURITIBA, 03 de Junho de 2020.

Assinatura Eletrônica
09/06/2020 09:16:57.0
ALICE MARLENE GRIMM
Presidente da Banca Examinadora

Assinatura Eletrônica
08/06/2020 15:50:50.0
CAIO AUGUSTO DOS SANTOS COELHO
Avaliador Externo (INSTITUTO NACIONAL DE PESQUISAS ESPACIAIS)

Assinatura Eletrônica
10/06/2020 15:34:51.0
ELOY KAVISKI
Avaliador Interno (UNIVERSIDADE FEDERAL DO PARANÁ)

Assinatura Eletrônica
09/06/2020 12:46:18.0
MANOEL ALONSO GAN
Avaliador Externo (INSTITUTO NACIONAL DE PESQUISAS ESPACIAIS)

Assinatura Eletrônica
08/06/2020 15:59:49.0
DANIEL HENRIQUE MARCO DETZEL
Avaliador Interno (UNIVERSIDADE FEDERAL DO PARANÁ)

Assinatura Eletrônica
12/06/2020 14:48:47.0
ALEXANDRE KOLODYNSKIE GUETTER
Avaliador Interno (UNIVERSIDADE FEDERAL DO PARANÁ)

Centro Politécnico, Bloco V - CURITIBA - Paraná - Brasil
CEP 81531-990 - Tel: (41) 3361-3210 - E-mail: ppgerha@ufpr.br
Documento assinado eletronicamente de acordo com o disposto na legislação federal Decreto 8539 de 08 de outubro de 2015.
Gerado e autenticado pelo SIGA-UFPR, com a seguinte identificação única: 43115
Para autenticar este documento/assinatura, acesse https://www.prppg.ufpr.br/siga/visitante/autenticacaoassinaturas.jsp
e insira o codigo 43115

TERMO DE APROVAÇÃO

Os membros da Banca Examinadora designada pelo Colegiado do Programa de Pós-Graduação em ENGENHARIA DE RECURSOS HÍDRICOS E AMBIENTAL da Universidade Federal do Paraná foram convocados para realizar a arguição da tese de Doutorado de **KÉNEDY CIPRIANO SILVÉRIO** intitulada: **VARIABILIDADE CLIMÁTICA EM MOÇAMBIQUE: IMPACTOS NA CHUVA, AVALIAÇÃO DE MODELOS E PREVISÃO**, sob orientação da Profa. Dra. ALICE MARLENE GRIMM, que após terem inquirido o aluno e realizada a avaliação do trabalho, são de parecer pela sua APROVAÇÃO no rito de defesa.

A outorga do título de doutor está sujeita à homologação pelo colegiado, ao atendimento de todas as indicações e correções solicitadas pela banca e ao pleno atendimento das demandas regimentais do Programa de Pós-Graduação.

CURITIBA, 03 de Junho de 2020.

Assinatura Eletrônica
09/06/2020 09:16:57.0
ALICE MARLENE GRIMM
Presidente da Banca Examinadora

Assinatura Eletrônica
08/06/2020 15:50:50.0
CAIO AUGUSTO DOS SANTOS COELHO
Avaliador Externo (INSTITUTO NACIONAL DE PESQUISAS ESPACIAIS)

Assinatura Eletrônica
10/06/2020 15:34:51.0
ELOY KAVISKI
Avaliador Interno (UNIVERSIDADE FEDERAL DO PARANÁ)

Assinatura Eletrônica
09/06/2020 12:46:18.0
MANOEL ALONSO GAN
Avaliador Externo (INSTITUTO NACIONAL DE PESQUISAS ESPACIAIS)

Assinatura Eletrônica
08/06/2020 15:59:49.0
DANIEL HENRIQUE MARCO DETZEL
Avaliador Interno (UNIVERSIDADE FEDERAL DO PARANÁ)

Assinatura Eletrônica
12/06/2020 14:48:47.0
ALEXANDRE KOLODYNSKIE GUETTER
Avaliador Interno (UNIVERSIDADE FEDERAL DO PARANÁ)
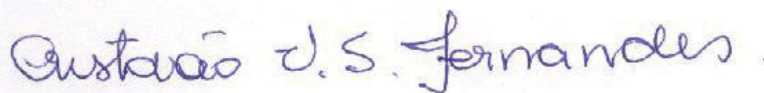
EXTRATO DE ATA

1

2

3 **Ata da 252ª Reunião do Colegiado do Programa de Pós-Graduação em Engenharia de Recursos Hídricos e**
4 **Ambiental,** com início às onze horas e trinta minutos do dia dezessete de julho de dois mil e vinte, por
5 videoconferência, pela plataforma Jitsi. Presentes: Coordenação do PPGERHA: Cristovão Vicente Scapulatempo
6 Fernandes e Daniel Costa dos Santos; Representante do Departamento Hidráulica e Saneamento: André Luiz Tonso
7 Fabiani; Representantes da área de Engenharia Ambiental Heloise Garcia Knapik , Regina Kishi; Representantes da
8 área de Recursos Hídricos e Ambiental: Daniel Detzel ; Representante Discente do Mestrado: Henrique Degraf e
9 Arthur H. R. Ferreira, os convidados e demais interessados. Aberta a sessão, passou-se para a Ordem do dia:...

10 **2) Alteração de Título da Tese de Kénedy Cipriano Silvério:** Foi aprovado, por unanimidade, a alteração de título
11 da Tese de Doutorado do aluno Kénedy Cipriano Silvério. Esta passa de "Variabilidade climática em Moçambique:
12 impactos na chuva, avaliação de modelos e previsão" para "Climate variability over Mozambique: impacts on rainfall,
13 assessment of models and forecast ", pois a mesma foi escrita em inglês...Nada mais havendo para tratar, o Professor
14 Cristovão Vicente S. Fernandes, deu por encerrada a sessão, da qual, para constar, eu Thalita Nishimoto, lavrei a
15 presente ata.

16 Curitiba, 17 de julho de 2020
17
18

19
20
21   **Prof. Dr. Cristovão Vicente Scapulatempo Fernandes**
22   **Coordenação do PPGERHA**
23
24

UFPR - Setor de Tecnologia – DHS – Programa de Pós Graduação em Engenharia de Recursos Hídricos e Ambiental
Caixa Postal 19011 – Jardim das Américas – 81531-990 – Curitiba – Paraná – fone- (41) 361 3210 - fax 41-361 3143
http//www.tecnologia.ufpr.br/pos_dhs.br – pos.dhs@ufpr.br

Publications

The results of this thesis have been published as:

Kénedy C. Silvério and Alice M. Grimm (2020). Southern Africa monsoon: Intraseasonal variability and monsoon indices. Submitted manuscript to Climate Dynamics

Kénedy C. Silvério and Alice M. Grimm (2020). Multiweek prediction skill of southern Africa monsoon anomalies in the subseasonal to seasonal (S2S) project database. Manuscript in preparation

Silvério, K.C., Grimm, A.M. Impact of intraseasonal variability of Mozambique summer monsoon rainfall on water resources availability across the country. In: XXIII Simpósio Brasileiro de Recursos Hídricos (SBRH), 2019, Foz do Iguaçu. Anais do Simpósio Brasileiro de Recursos Hídricos (SBRH), 2019

Silvério, K.C, Grimm, A.M. The skill of monsoon rainfall multiweek prediction over Mozambique in the Subseasonal to Seasonal (S2S) Project database. In: II Simpósio do PPGERHA, 2019, Curitiba. Anais do II Simpósio do PPGERHA, 2019, Curitiba

Silvério, K.C, Grimm, A.M. Intraseasonal variability of summer monsoon rainfall over Mozambique. In: XX Congresso Brasileiro de Meteorologia, 2018, Maceió. Anais do XX Congresso Brasileiro de Meteorologia, 2018

Silvério, K.C, Grimm, A.M. Intraseasonal rainfall variability over Mozambique during the austral summer season and its possible relationship with monsoon circulation. In: I Simpósio do PPGERHA, 2018, Curitiba. Anais do I Simpósio do PPGERHA, 2018, Curitiba

In memory of my mother

Laurinda Mizé Chachane

Acknowledgements

"What you get by achieving your goals is not as important as what you become by achieving your goals
Henry David Throreau"

RESUMO

As chuvas de monção, que na África Austral (SAF) geralmente ocorrem durante o verão austral (dezembro–fevereiro, DJF) variam em diferentes escalas de tempo. Neste estudo, a ênfase foi dada à sua variabilidade intrassazonal (ISV), que é de grande importância para a produção agrícola, gerenciamento de recursos hídricos e previsão subssazonal. O estudo foi dividido em duas partes: observacional e avaliação de modelos, cujos resultados foram baseados em dados diários de precipitação observada (1979–2005) e previsões retrospectivas semanais de modelos do *subseasonal to seasonal (S2S) prediction Project* (1999–2010), respectivamente. Na primeira parte, modos rotacionados de ISV foram determinados sobre leste da SAF. Verificou-se que um destes modos exibe forte distribuição espacial na região com precipitação mais intensa de monção sobre o interior do subcontinente, além deste estar associado a variações na circulação de monção. Suas oscilações mais significativas em diferentes bandas de frequência da ISV exibiram períodos em torno de 12, 22–24 e 50 dias, também encontradas anteriormente na ISV de chuvas de monção sobre América do Sul (SA). A oscilação de 12 dias pareceu estar associada à oscilação quase-bissemanal, originada das ondas de Rossby no cinturão extratropical de ventos de oeste e se propagando para a SAF. As anomalias compostas para as defasagens positivas e negativas associadas às fases positiva e negativa do modo em alusão na faixa de 20 e 90 dias confirmaram um modo de 24 dias e a influência da oscilação de Madden-Julian (OMJ). Além disso, indicaram a influência de anomalias convectivas sobre a SA através da propagação de ondas atmosféricas deste continente (SA) para a SAF. Um índice de precipitação de monção (MPI), bem como alguns índices de circulação de monção, calculados como anomalias diárias padronizadas sobre uma determinada área, foram propostos para ajudar a caracterizar, monitorar e prever a ISV de monção (períodos ativo e inativos). Ambos índices de precipitação e circulação de monção se mostraram refletir adequadamente a variabilidade da precipitação na região núcleo de monção sobre o subcontinente (20°S–13,75°S; 32°E–38°E), onde sua previsão apresenta grande utilidade. Na segunda parte, usando o MPI e um dos índices de circulação de monção sugeridos, foi avaliada a habilidade preditiva de todos os 11 modelos do projetos S2S em simular períodos ativos e inativos de monção sobre a SAF. Embora os modelos prevejam as anomalias locais de vento zonal em larga escala para antecedências superiores a 3 semanas, a habilidade preditiva de anomalias de precipitação de monção parece se limitar à uma única semana. A classificação dos modelos mostrou ECMWF, JMA, UKMO, CNRM, KMA e NCEP como sendo os melhores modelos pra prever a monção da SAF. Os períodos ativos observados de monção foram verificados estarem associados a um trem de ondas se propagando para a SAF, que parece ser produzido por convecção anômala sobre a SA e o Oceano Atlântico. Todos os modelos selecionados mostraram uma tendência em reproduzir as anomalias convectivas associadas aos períodos ativos observados de monção, embora nem todos estes modelos reproduzem as anomalias de circulação associadas a esses períodos ativos observados de monção. Isto parece estar provavelmente associado a erros relacionados a deficiências dos modelos em representar as teleconexões.

Palavras–chave: Chuvas de monção na África Austral, Variabilidade Intrassazonal, Oscilação de Madden–Julian (MJO), modelos do projeto S2S, Teleconexão entre América do Sul e África Austral

ABSTRACT

Southern African monsoon rainfall that usually occurs during December-January-February (DJF) season varies over a range of timescales. Here the emphasis was placed on its intraseasonal variability (ISV), which is of great importance for agricultural production, water resources management, and subseasonal prediction. The study was divided into two parts: diagnosing analysis and modeling assessment, whose results were based on daily rainfall gauge data (1979–2005) and weekly subseasonal to seasonal (S2S) prediction project models reforecast data (1999–2010), respectively. In first part, rotated modes of ISV were determined over eastern southern Africa (SAF). One of the leading modes was found to exhibit strongest factor loadings over the region with most intense monsoon precipitation over land and be associated with variations in the monsoon circulation. Its most significant oscillations in different ISV frequency bands were found to exhibit periods around 12, 22–24 and 50 days, also found previously in ISV of monsoon rainfall over South America (SA). The 12-day oscillation appeared to be associated with the quasi-biweekly oscillation originated from Rossby waves in the extratropical westerly belt propagating into SAF. The lead-lag composite anomalies keyed to positive and negative phases of the mode in the 20–90 day band confirmed a 24 day mode and the influence of the Madden Julian Oscillation (MJO). Besides, they indicated the influence of convective anomalies over SA through propagation of atmospheric waves from this continent (SA) to SAF. A monsoon precipitation index (MPI) as well as some monsoon circulation indices, computed as area averaged daily standardized anomalies, were proposed to help characterizing, monitoring and predicting monsoon ISV (active and break periods). Both MPI and monsoon circulation indices were found to reflect adequately the variability of the precipitation in the SAF core monsoon region over land (20°S–13.75°S; 32°E–38°E) where its prediction is more useful. In second part, using the MPI and one of the suggested monsoon circulation indices, the predictive skill of all 11 S2S project models in simulating monsoon active and break periods over SAF were assessed. Although the models appeared to predict the local large-scale zonal wind anomalies for lead times beyond 3 weeks, predictive skill of monsoon precipitation anomalies was found to be limited to a week. The model's rank showed ECMWF, JMA, UKMO, CNRM, KMA and NCEP as the top scoring ones for predicting monsoon in SAF. The observed monsoon active periods were found to be associated with an eastward propagating wave train that seems to be produced by convection over South America and the Atlantic Ocean. All selected models showed a tendency to reproduce the convective anomalies associated with observed monsoon active periods, although not all reproduce their associated circulation anomalies. This was found to be likely associated with errors related with model deficiencies in representing teleconnections.

Key-words: Southern Africa Monsoon Rainfall, Intraseasonal Variability, MJO, S2S project Models, Teleconnections between South America and southern Africa.

List of figures

List of tables

List of acronyms

AL	Angola Low
AR	Annual range
BH	Botswana High
BoM	Australian Bureau of Meteorology
CA	Composite analysis
CAB	Congo Air Boundary
CAPES	Coordenação de Aperfeiçoamento de Pessoal de Nível Superior
CMA	China Meteorological Administration
CMIP	Coupled Model Intercomparison Project
CNRM	the Centre National de Recherches Météorologiques of Météo-France
CPC	Climate Prediction Center
DJF	December-January-February
DRC	Democratic Republic of Congo
ECCC	Environment and Climate Change Canada
ECMWF	European Centre for Medium-Range Weather Forecasts
ENSO	El Niño Southern Oscillation (ENSO)
EOF	Empirical orthogonal function
GPCC	Global Precipitation Climatology Centre
GPCP	Global Precipitation Climatology Project
GPH	Geopotential Height (Altitude) in meters
HEST	Higher Education Science and Technology project
HMCR	Hydrometeorological Centre of Russia
ICTP	International Centre for Theoretical Physics
INAM	Instituto Nacional de Meteorologia
INE	Instituto Nacional de Estatística
INGC	Instituto Nacional de Gestã doe Calamidades
IDV	Interdecadal variability
ISAC	National Research Council Institute of Atmospheric Sciences and Climate of Italy
ISV	Intraseasonal variability

ISPS	Intituto Superior Politécnico Songo
ITCZ	Inter-tropical convergence zone
JMA	Japan Meteorological Agency
IPO	Interdecadal Pacific oscillation
MCT	Mozambique Channel Trough
MCTESTP	Ministério da Ciência e Tecnologia, Ensino Superior e Técnico Profissional
MH15	Marshall and Hendon (2015)
MJJAS	May-June-July-Agost-September
MJO	Madden-Julian Oscilation
MPI	Monsoon precipitation index
NCAR	National Center for Atmospheric Research
NCEP	National Centers for Environmental Prediction
NEM	Northeasterly monsoon
NDJFM	November-December-January-February-March
NH	Northern Hemisphere
NOAA	National Oceanic and Atmospheric Administration
NWM	Northwesterly monsoon
NW-SE	Northwest-Southeast
OCHA	United Nations Office Coordination of Humanitarian Affairs
OLR	Outgoing long-wave radiation
PC	Principal component
PCA	Principal component analysis
PCC	Pearson correlation coefficient
PDO	Pacific decadal oscillation
PPGERHA	Programa de Pós-graduaçào em Engenharia de Recursos Hídricos e Ambiental
PSD	Power spectral density
PSI	Stream function
PSIZA	Zonally asymmetric PSI
QDV	Quasi-decadal variability
REOF	Rotated empirical orthogonal function
SA	South America

SACZ	South Atlantic convergence zone
SAF	Southern Africa
SAFM	SAF monsoon
SAH	Subtropical south Atlantic High
SD	Standard deviation
SETW	Southeast trade winds
S2S	Sub-seasonal to Seasonal
SG20	Silvério and Grimm (2020)
SH	Southern Hemisphere
SICZ	Indian Ocean convergence zone
SIOD	Subtropical Indian Ocean dipole
SIH	Subtropical South Indian High
SST	Sea surface temperature
SWIO	Southwest Indian Ocean
TTTs	Tropical temperate troughs
UFPR	Universidade Federal do Paraná
USD	United States dollar
WCRP	World Climate Research Program
WWRP	World Weather Research Program

List of symbols

σ	Standard deviation
ρ	Firrst-order autocorrelation
π	Mathematical constant (3.14159)
Δt	Temporal interval between one term and other in time series
υ	Degree of freedom
χ	Chi square

Contents

1 Introduction

1.1 Background

Climate variability, defined as the variations in the mean state of climate, is one of the most important climate system features. It can strongly impact the lives and economy of any world region. Southern Africa (SAF), defined here as the Africa subcontinent poleward of 10°S (Fig. 1a), where Mozambique is located (Fig. 1a), is not an exception.

SAF, with exception of its southwest and southcoastal portions (where it rains more in winter or all year round), experiences generally maximum rainfall during summer months (October-March) with a peak occurring between December and February (DJF) months (Fig. 1b).
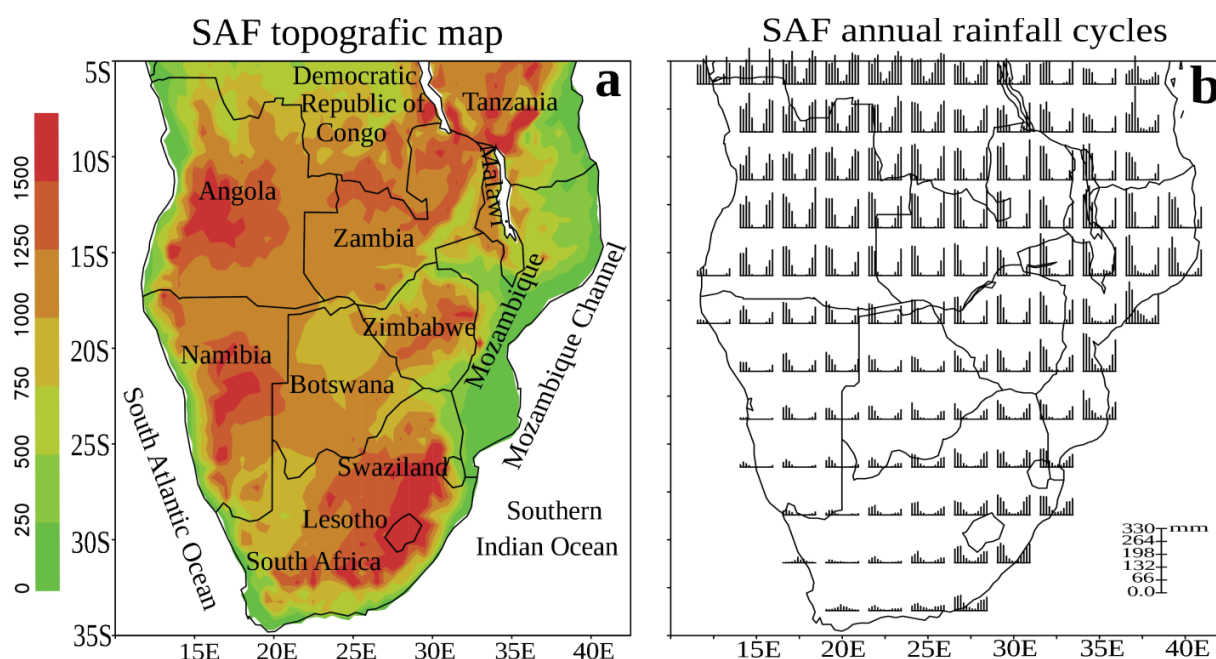
Figure 1 – (**a**) Southern Africa (SAF; the land area south of 10°S) domain and its topography (in meters) at 0.5° grid resolution, obtained from the International Centre for Theoretical Physics topographic data (ICTP; http://clima-dods.ictp.it/regcm4/). (**b**) The annual rainfall cycles over SAF obtained from the Global Precipitation Climatology Centre (GPCC) data (SCHNEIDER et al. 2016) for the period 1979–2005.

Although this seasonal peak in summer is a typical monsoon feature, most of SAF was for a long time not considered a monsoon region. This is because Ramage (1971) considered a monsoon regime only that characterized by a seasonal reversal of prevailing low-level winds. This definition, although accepted by the meteorological community worldwide for almost 3 decades, was contested by Zhou and Lau (1998) and Webster et al. (1998), who qualified the Americas as monsoon regions in terms of rainfall. The contemporaneous monsoon definition suggested by Zhou and Lau (1998) and Webster et al. (1998) characterized by a seasonal contrast in multiple meteorological variables (e.g., precipitation, wind's components, etc) lead recently Wang and Ding (2008) and Yim et al. (2014) to consider most of SAF as one of the eight world monsoon domains (Fig. 2).
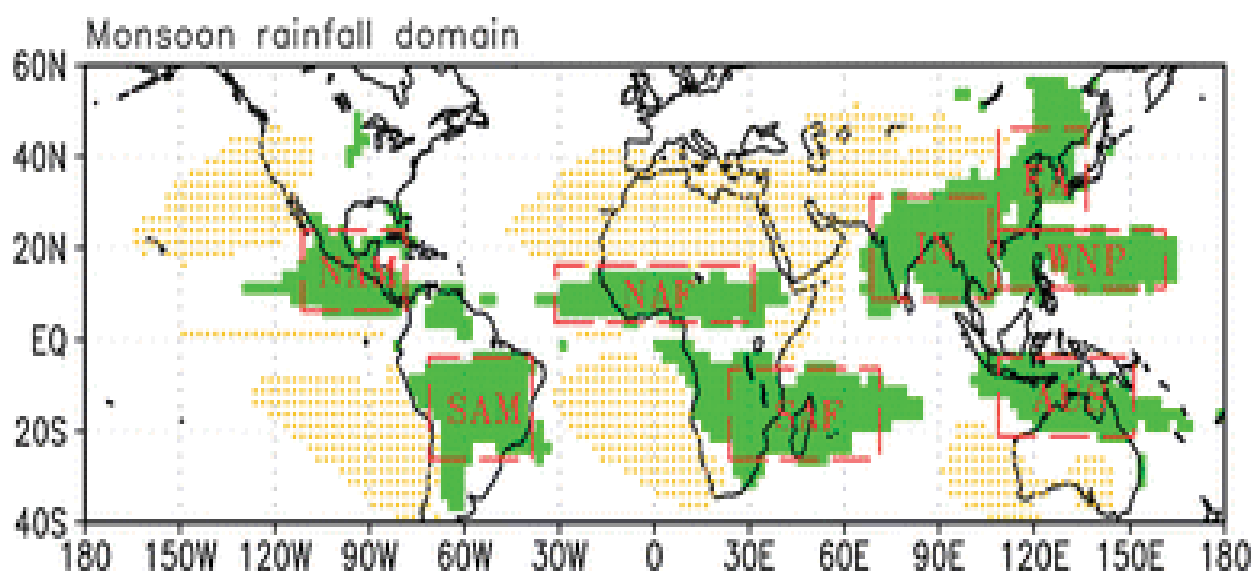
Figure 2 – Regional monsoon precipitation domains (shaded, green) defined by the regions in which the (a) annual range (AR) of precipitation rates exceeds 2 $mm\ day^{-1}$ (or 300 mm per season) and (b) the local summer precipitation exceeds 55 % of the total annual rainfall. Here the AR is defined as May through September (MJJAS) precipitation minus November through March (NDJFM) precipitation in the Northern Hemisphere (NH) and NDJFM minus MJJAS precipitation in the Southern Hemisphere (SH). Also shown are the approximate rectangular domains of regional monsoons and their names. The threshold values used here distinguish the monsoon climate from the adjacent dry regions where the local summer precipitation is less than 1 $mm\ day^{-1}$ (stippled, yellow). The Climate prediction center Merged Analysis of Precipitation–Global Precipitation Climatology Project (GPCP) data were used. Figure extracted from Yim et al. (2014).

Currently, these eight regional monsoon domains (Fig. 2) contain more than 70% of the world's population (WANG et al., 2012; ZHISHENG et al., 2015). The economies and livelihood of most people in these regions highly depend on rain-fed activities, such as agricultural and hydropower productions, just to name a few. The success of these activities relies on water resources whose availability mostly depends on occurance of monsoon rainfall. However, monsoon rainfall by nature exhibits significant variability on wide range of time scales, which sometimes results in extreme events (either floods or droughts) with tremendous negative impacts in the regions where the monsoon rainfall occurs and even in non-monsoon regions as the monsoon rainfall through its latent heat release can influence atmospheric general circulation over the globe (ZHANG and WANG, 2008). A good example of the impacts of monsoon variability includes the devastating floods occurred over Mozambique during February 2000 (REASON and KEIBEL, 2004), January 2013 (MANHIQUE et al., 2015), January-February 2015 (OCHA, 2015), and March 2019 (INAM, 2019; INGC, 2019), which together claimed aproximately 1750 deaths and an accumulated property damages exceeding 3 billion USD. Other example includes the long-lasting droughts observed in most SAF during 2014–2016 years (ARCHER et al., 2017).

Although results of a number of climate projection studies differ from one study to another regarding the occurrence and frequency of extreme events under the warming climate in the near future over SAF, there are converging evidences suggesting that,their intensity is likely to be greater (LI et al., 2015; PINTO et al., 2016). In this perspective, and given the high vulnerability of SAF to extreme events (REASON et al., 2006), an investigation of regional climate variability, especially that related with summer monsoon rainfall is needed not only for the purpose of understanding its causes, but also to be able to predict its occurrence.

In the literature review presented in section 2 there are evidences of considerable number of studies carried out during the most recent 3–4 decades, which have helped disclosing many important mechanisms associated with regional seasonal rainfall. However, most of those have focused on processes responsible for variability at synoptic (1–10 days) and interannual (2–8 years) to longer (>8–10 years) timescales, with less attention to subseasonal (intraseasonal) variability, despite its highly relevance for decision making, as actions to support water resource allocations, disaster risk reduction, and crop management often take place on this time horizon.

In an attempt to fill this gap, this study investigates (1) the intraseasonal variability (ISV) of regional summer rainfall with focus on Mozambique and (2) the prediction of this variability by Subseasonal to Seasonal (S2S) prediction Project models (VITART et al., 2017).

S2S project is a 5-year international collaborative research initiave launched jointly by the World Weather Research Program (WWRP) and the World Climate Research Program (WCRP) in 2013 (VITART and ROBERTSON 2018), which in 2019 was extended for an additional 5 years. The main goal of this initiative is to improve forecast skill and understanding of the predictability sources at this time range, and to promote its uptake by operational centers and exploitation by the applications communities (http://www.s2sprediction.net/).

Predictive skill of operational global state-of-the-art models participating in this project has been assessed for different meteorological variables at different spatial scales. The results derived from these assessments appear overall encouraging as it has been shown that the onset, evolution and decay of some large-scale extreme events that occurred in the past might have been predicted several weeks ahead, possibly associated with Madden-Julian Oscillation (MJO) teleconnections (VITART and ROBERTSON 2018; ROBERTSON et al. 2018).

Since these results document the prediction quality at sub-seasonal lead time, they can help to put together forecasting scheme of extremes events, to which SAF is highly prone, and hence minimize their impacts on the region.

This thesis builds upon the hypothesis that the subseasonal monsoon precipitation anomalies over SAF, particularly Mozambique are in part modulated by the MJO, the primary source for subseasonal predictability. Therefore, it is valid to test the subseasonal predictions generated by S2S models in order to verify their performance and possibly increasing the forecasts lead time of the extreme events over Mozambique, including neighbouring countries in the region, by selecting most skilful models.

The present thesis is divided into seven chapters. Chapter 2 is a background summary on SAF climate variability. The first two sections describe features that influence the the day-to-day weather and rainfall annual cycle over the region, while the last two sections discuss notable fators influencing regional rainfall on scales from submonthly to seasonal and interannual to decadal or longer. The description of the data and methods used in this study is given in Chapter 3.

Chapters 4 and 5 present the results of this study in the form of two manuscripts which together address the proposed research objectives as outlined in section 1.3. Before each paper a synopsis and text are presented to provide the cohesive storyline of the work.

Chapter 4 (paper01) focuses on diagnosing the intraseasonal leading modes in the Mozambique gauge monsoon rainfall and their associated circulation patterns. A monsoon precipitation index (MPI) defined over SAFM core region located over central Mozambique and several circulation indices associated with the MPI are proposed to facilitate the prediction and monitoring of rainfall ISV, characterized by active and break monsoon episodes.

In Chapter 5 (paper02), the ability of the S2S prediction project models in reproducing the observed subseasonal SAFM precipitation anomalies using the monsoon indices derived in Chapter 4 is assessed. This assessment is made at multiweek lead times, out to 4 weeks, using retrospective forecast (called also hindcasts) data over the S2S models commom period (1999–2010).

In Chapter 6 the summary and concluding remarks of overall research are outlined, while the caveats and recommendations for the future works are presented in Chapter 7.

As a result, we hope that the findings of this thesis have not only helped improving our knowledge about the country's climate variability at intraseasonal timescales, but also that it has helped identifying strengths and weaknesses of the S2S models and, consequently, their adequacy for operational forecasting over Mozambique and other countries in the SAF region.

1.2 Statement of the problem

Due in part to the predominantly rain-dependent economies in the region, and the high degree of variability, the nature of SAFM rainfall has long been the subject of studies on wide range of timescales (TODD et al., 2004). Most of those studies have, however, emphasized the variability at synoptic and interannual to longer scales ignoring largely the subseasonal one.

Although those studies have yielded invaluable knowledge that culminated with the development of seasonal forecasts for the region (MASON et al., 1996), resulting in increased preparedness with significant economic savings and societal benefits, there are some fundamental problems that call for additional studies. The forecast end users (e.g., regional farmers) are actually more interested in knowing the onset, duration and intensity of either active

(wet) or break (dry) periods during the rain season instead of having just a forecast of seasonal average conditions. This information is, however, only possible if the national operational meteorological services across SAF turn to development of predictions at subseasonal timescale. Although the predictions at this timescale are at a relatively early stage of development, they actually are routinely issued experimentally/operationally by at least eleven international meteorological centres across the globe (WHITE et al., 2015), and the results derived from them (forecasts) appear overall encouraging, since they have shown, for specific case studies, that the onset, evolution and decay of some large-scale extreme events occurred in the past might have been predicted several weeks ahead, possibly associated with the MJO teleconnections (ROBERTSON et al., 2018; VITART and ROBERTSON, 2018). As it does not mean that similar results will be obtained for SAF, it is worth evaluating the applicability of these predictions for this region.

This study is, thus, proposed to advance our understanding on observed subseasonal SAFM anomalies and, their prediction by the S2S project models.

In doing so, it is hoped that the results derived from this research will (1) add some knowledge to existing one on SAFM variability and, (2) contribute to the S2S Monsoon Prediction Subproject, for which a comparison of monsoon prediction skill across several models is undergoing (http://www.s2sprediction.net/) and (3) stimulate similar works across the countries in the region. Our models evaluation results are also hoped to assist the modeling developer communities with information about the strengths and weaknesses of their models, which can help them to further improve these models in future.

1.3 Aims and objectives of the study

1.3.1 Aims

1. To investigate rainfall intraseasonal variability (ISV) over southern Africa and the mechanisms behind this variability;
2. To assess the ability of the Sub-seasonal to Seasonal (S2S) Prediction Project models (VITART et al., 2017) in reproducing this variability.

1.3.2 Objectives

In order to consistently achieve these aims, the following objectives have been addressed:

1. Document the leading patterns of observed rainfall ISV over Mozambique and their associated physical mechanisms, giving particular emphasis on unexplored questions such as atmospheric teleconnection patterns at this time scale;

2. Propose monsoon indices for characterization, monitoring, and prediction in an easier way of the broad-scale SAF monsoon rainfall variability and its associated circulation;

3. Evaluate the ability of the S2S project models in reproducing the observed monsoon variability over Mozambique using the defined monsoon indices.

2 Climate variability in southern Africa: literature review

2.1 Study region and its topographical features

Topographically, SAF is characterized by complex features that affect the climate of the region. These features include the costal plains and mountains, Zambezi River, Niassa Lake (between Malawi and Mozambique and Tanzania), and other water bodies, and the neighboring oceanic regions (Figs. 1a, 3a). The highlands regions play localized role in generating upslope circulation that triggers convection, responsible for high amounts of rainfall where these mountains occur. A good example is the Niassa plateau in northern Mozambique, where the mean annual rainfall exceeds 2000 mm (GAVRILOV et al., 1986). The presence of large water bodies in the region (e.g., Niassa Lake) and their associated circulations also alter the local rainfall amounts (DIALLO et al., 2018; NICHOLSON et al., 2014).
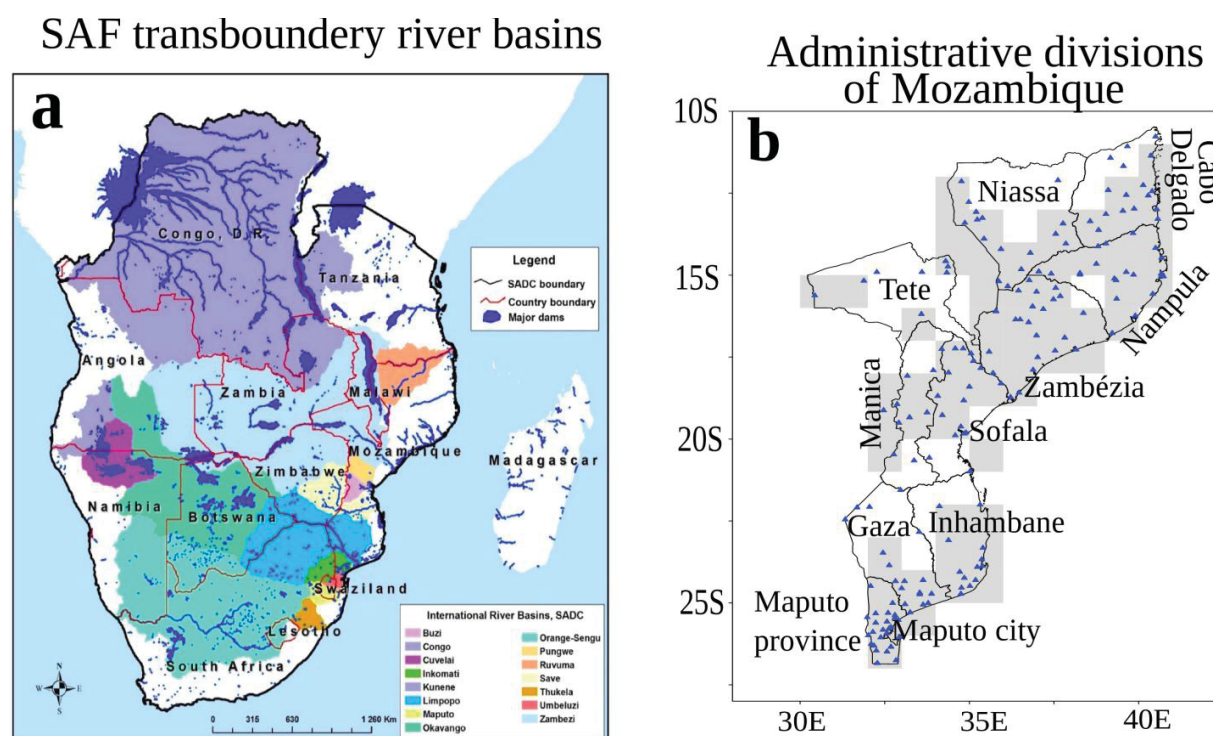
Figure 3 – (**a**) Most prominent river basins over SAF (from Mabhaudhi et al. (2016)). (**b**) Administrative divisions of Mozambique. The triangles represent the country's meteostations whose data are used in the analysis described in section 4. Shading in gray indicates grid points in which the meteostations have less than 30% of missing data (see the description in section 3).

The present research study focuses on Mozambique (801,537 km^2), a country in eastern SAF (Fig. 1a), with aproximatelly 28 million inhabitants in 2018, 65% of whom living in rural areas and whose subsistence heavily relies on agriculture (INE, 2019). The country is bounded by Swaziland to the south, South Africa to the southwest, Zimbabwe to the west, Zambia and Malawi to the northwest, Tanzania to the north and Indian Ocean to the east (Fig. 1a). Mozambique is divided into 11 states (provinces), namely, Niassa, Cabo Delgado, Nampula, Zambezia, Tete, Manica, Sofa, Inhambane, Gaza, Maputo Province and Maputo City (Fig. 3b).

2.2 The main factors affecting the day-to-day regional rainfall variability

Since the climatological mean pattern of regional seasonal rainfall and its associated circulation in terms of the main air flows is described in section 4, referred to as the paper01, here the description of other atmospheric factors influencing the day-to-day weather is presented to avoid the duplication of information. These include the existence of high pressure systems (anticyclones) on both sides of the subcontinent, with seasonally varying positions and intensities. These anticyclones (South Atlantic and South Indian Oceans Subtropical Highs) play an important role in moisture transport onto the interior, which may lead to ascending movements and hence rainfall in the region. Over the region also occur heavy rains associated sometimes with the passage of tropical cyclones across the coastal margins of Mozambique and eastern South Africa (MASON and JURY, 1997). The westerly waves and associated incursions of extra-tropical cyclones, easterly waves, and frontal systems (particularly cold) play an important role in the formation of tropical temperate troughs (TTTs), which are considered as the main summer synoptic rain-producing systems in the region (HARRISON, 1984; WASHINGTON and TODD, 1999). The TTT systems form when a tropical low (Angola Low, AL) is coupled to a temperate westerly (Rossby) wave via a subtropical through (Fig. 4a), forming the short-lived (typically 3–7 days), northwest–southeast (NW–SE) tilted convective cloudbands along the leading edge of the westerly throughs which link the mid-latitudes disturbunces to the tropical convergence zone (HARRISON, 1984; HART et al., 2010; MACRON et al., 2014). In absence of midlatitude influence, the TTTs are just simple throughs rather than elongated ones (JURY, 1997). The total rainfall associated with an individual TTT event depends upon the availability of atmospheric moisture and stability, the strength of upper-

level divergence and the speed of the movement of the through (e.g., HARRISON, 1984).
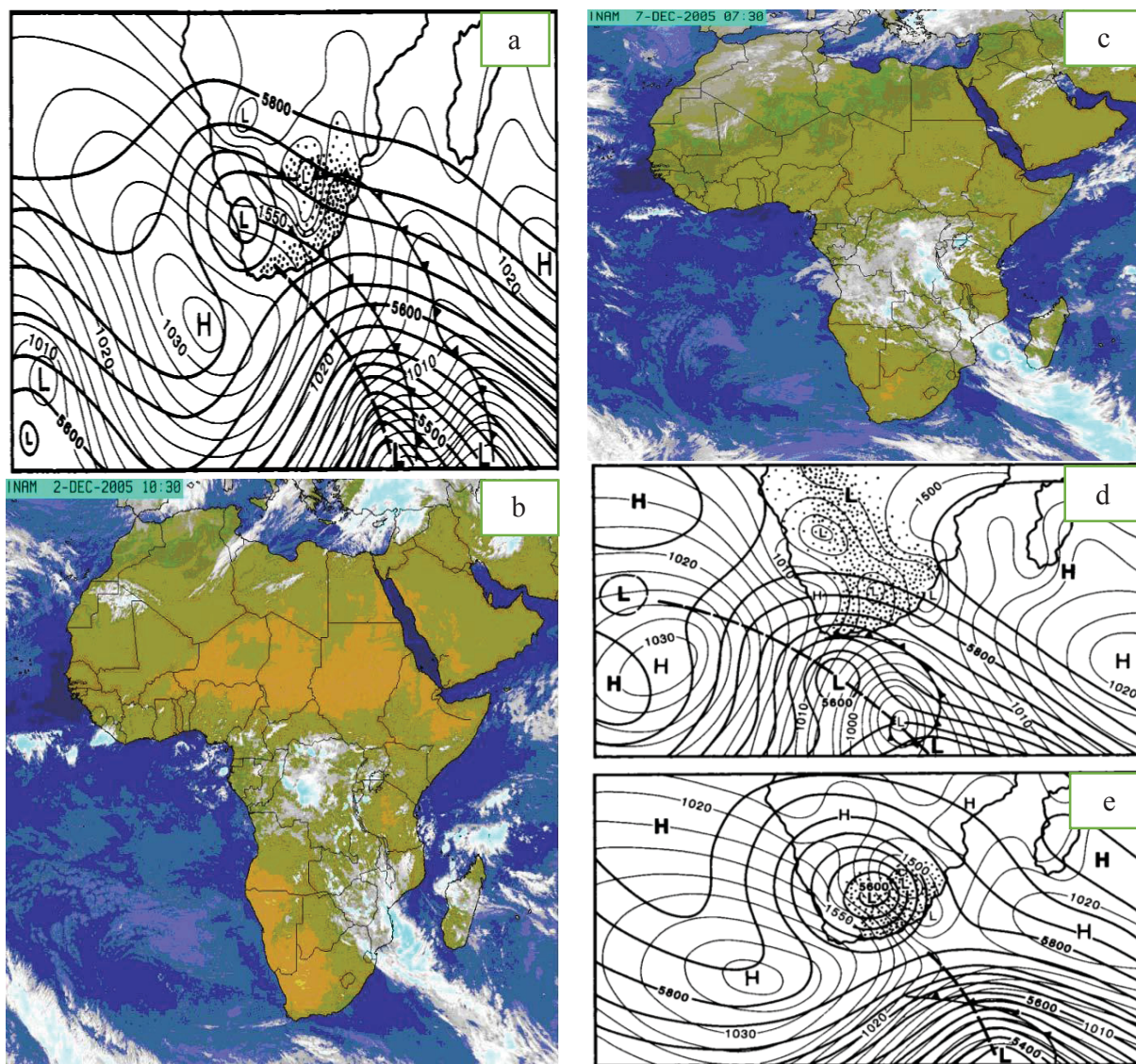
Figure 4 – Synoptic chart for (a) 23 January 1981, showing the formation of a TTT; (b) and (c) show TTT satellite images and its associated cloudbands over SAF on 2nd and 7th December 2005, respectively. (d) 27 August 1970, showing the formation of cut-off low; and (e) 9 September 1981, showing the formation of a cut-off low and ridging anticyclone. In the panels a, d and e, light lines show isobars at mean sea level (hPa) over the oceans and contours of the 850 hPa surface (gpm) over the land; heavy lines show contours of the 500 hPa surface (gpm). Areas receiving precipitation are stippled. The letters H and L in these panels denote centers of High and Low pressure, respectively. Panels (b) and (c) were courtesy of Mozambique National Institute of Meteorology (INAM). Figures a, d and e were extracted from Mason and Jury (1997), whereas. b-c have been extracted from Manhique (2008)

The TTT events are usually responsible for floodings during the second half of the suumer (February–March months; e.g., LINDESAY and JURY, 1991; WALKER and LINDESAY, 1989), whereas during early summer (November–December months) they are generally associated with shorter lived light rainfall because of enhanced baroclinic westerly shear from the upper troposphere of the tropical Atlantic Ocean, whereas low-level moisture is advected from the central Indian Ocean (BARCLAY et al., 1993; MAKARAU and JURY, 1997).

Acoording to Cook (2000), the TTTs and their associated cloudbands collectively form the South Indian Ocean convergence zone (SICZ), an austral summer land-based convergence zone (Fig. 4b-c) whose position and intensity acoording to that author is partially determined by surface conditions over SAF and the neighboring southwestern Indian Ocean.

Although subtropical throughs through SICZ contribute to widespride summer monsoon rainfall over much of the region, the heaviest falls are usually associated with cut-off lows (MASON and JURY, 1997), which usually form in conjuction with an anticyclonic ridge to the south of the subcontinent during the transition seasons when meridional temperature and pressure gradients are strongest (Fig.4d-e; Van LOON, 1971). Cut-off lows are more important in early and late-season rainfall, i.e, transition seasons (TALJAARD, 1986).

More regionally, in northeastern South Africa, southern Mozambique, and Botswana, mesoscale convective complexes can contribute up to 20% of summer rainfall during the late summer (BLAMEY and REASON, 2013).

As the nature of occurrence of these factors changes throughout the year, their influence on regional rainfall also varies over the year. Furthermore, the influence of these factors can also be modulated by the occurrence of longer scale climate variability modes (e.g., El Niño Southern Oscillation, ENSO) by either amplifying or supressing the impacts of these factors on regional rainfall variability. For fuller details on description of these (day-to-day) mechanisms, we refer the readers to Jackson (1951), Mason and Jury (1997), Silvério and Grimm (2020), Taljaard (1986), Torrance (1972), Tyson and Preston-Whyte (2000), just to name a few.

2.3 Impacts of intraseasonal variability modes on regional rainfall

Intraseasonal variability (ISV) refers to cycles operating between time scales beyond synoptic weather (>10 days) and shorter than a season (<90 days).

As the total (10–90 days) ISV involves fluctuation operating on both higher (10–30 days) and lower (30–90 days) frequencies, there is need to get deeper into the processes governing different frequencies, and hence, rainfall ISV.

Variability at timescale between 30 and 90 days is attributed to the Madden-Julian Oscillation (MJO), a well-known intraseasonal leading mode of tropical atmospheric variability (MADDEN and JULIAN, 1971). It involves significant variations in the tropical convective activity and tropospheric large-scale circulation with coherent signals in many other variables, all propagating eastward across the equatorial Indian and Pacific Oceans, which alter rain every 30–90 days in the tropics and other parts of the globe throughout the year (Fig. 5).

The MJO impacts on various weather/climate phenomena across the globe have been reported in numerous studies, and those studies have also shown that it plays an important role in the coupled atmosphere-ocean system (ZHANG, 2005, 2013).

Although the MJO strongest activity coincides with austral summer season (DJF), suggesting a potential chance for skillful subseasonal prediction of SAFM rainfall anomalies, its impact on rainfall over the region (SAF) is thought to be of lesser importance (e.g., MACRON et al., 2016; OETTLI et al., 2014; POHL et al., 2007; ZAITCHIK, 2017). This can be explained in part by the smaller number of strong statistical significant spectral peaks at MJO time band (30–90 days) compared to those at 10–30-days band, as reported in most studies on regional rainfall ISV (e.g., LEVEY and JURY, 1996; MAKARAU, 1995; SILVÉRIO and GRIMM, 2020). This corroborates the results reported in a comprehensive study on MJO impacts across the region by Pohl et al. (2007), who found relatively weak MJO influence on regional rainfall, explained by 35–40% of all intra-seasonal variance in the outgoing long-wave radiation (OLR), used often as a proxy for convective activity. Furthermore, in the subsequent study by Pohl et al. (2009) the TTTs have been found equally likely occurring during any MJO phase, suggesting that they are an independent mode of variability at MJO timescale (ZAITCHIK, 2017). Other factors supporting these findings include the impacts of local features (e.g., topography, water bodies

and valleys) associated with rainfall variability in the region on the influence of large-scale systems including MJO (e.g., MACRON et al., 2016).

Although the MJO influence on SAFM rainfall anomalies appear weaker compared to those at 10–30-days band as suggested in many previous studies including that by Silvério and Grimm (2020; hereafter referred to as SG20), one can affirm that it does affect regional rainfall via the teleconnection mechanisms associated in part with MJO-related convective activity over South America (SA) and neighbouring Atlantic Ocean, as reported by Grimm (2019). According to Silvério and Grimm (2020), the pattern of rainfall anomalies few days before they hit northeast SAF resemble the anomalies associated with MJO phase 1, suggesting that teleconnection mechanisms between SA and SAF favor MJO impacts on monsoon anomalies over the latter subcontinent. This implies that a better understanding of the mechanisms involving MJO impacts on regional rainfall depends in part on desclosing fairly well the processes governing the variability of SA monsoon system that seems to be of high importance for some climate processes occurring over SAF. This issue although interesting is not a matter of this thesis as it is being done fairly well by the SA research community.

On the order hand, the 10–30-days fluctuations which have been found in many intraseasonal regional studies appear as a major contributor to the total 10–90-day intraseasonal variability in regional rainfall (e.g., LEVEY and JURY, 1996; MAKARAU, 1995; SG20). For instance, Makarau (1995) found in SAF observed rainfall cycles operating at 10–25 days and 40–50 days using spectral analysis. According to that author, wet spells associated with those cycles were related to troughs extending from Angola in the northwest to the Mozambique Channel in the southeast. Similarly, Levey and Jury (1996) found a combination of 20–30- and 40–60-day oscillations in SAFM rainfall. These authors found the MJO prevalent in wet years, while the 20–30-day ISV seemed more dominant in dry years. About one-third of the rainfall oscillations according to Levey and Jury (1996) were found to arise locally from stationary modes linked to TTTs, with two fast intraseasonal fluctuations ''inside'' a slower MJO. Another one-third of intraseasonal fluctuations were found to propagate eastward in sympathy with midlatitude and equatorial waves.

A combination of 10–30- and 40–60-day oscillations was also reported recently in SG20 who found enhanced rainfall in the region to be associated with eastward propagating wave

Rainfall (shading) and PSIZA850 (contours) OLR (shading) and PSIZA200 (contours)
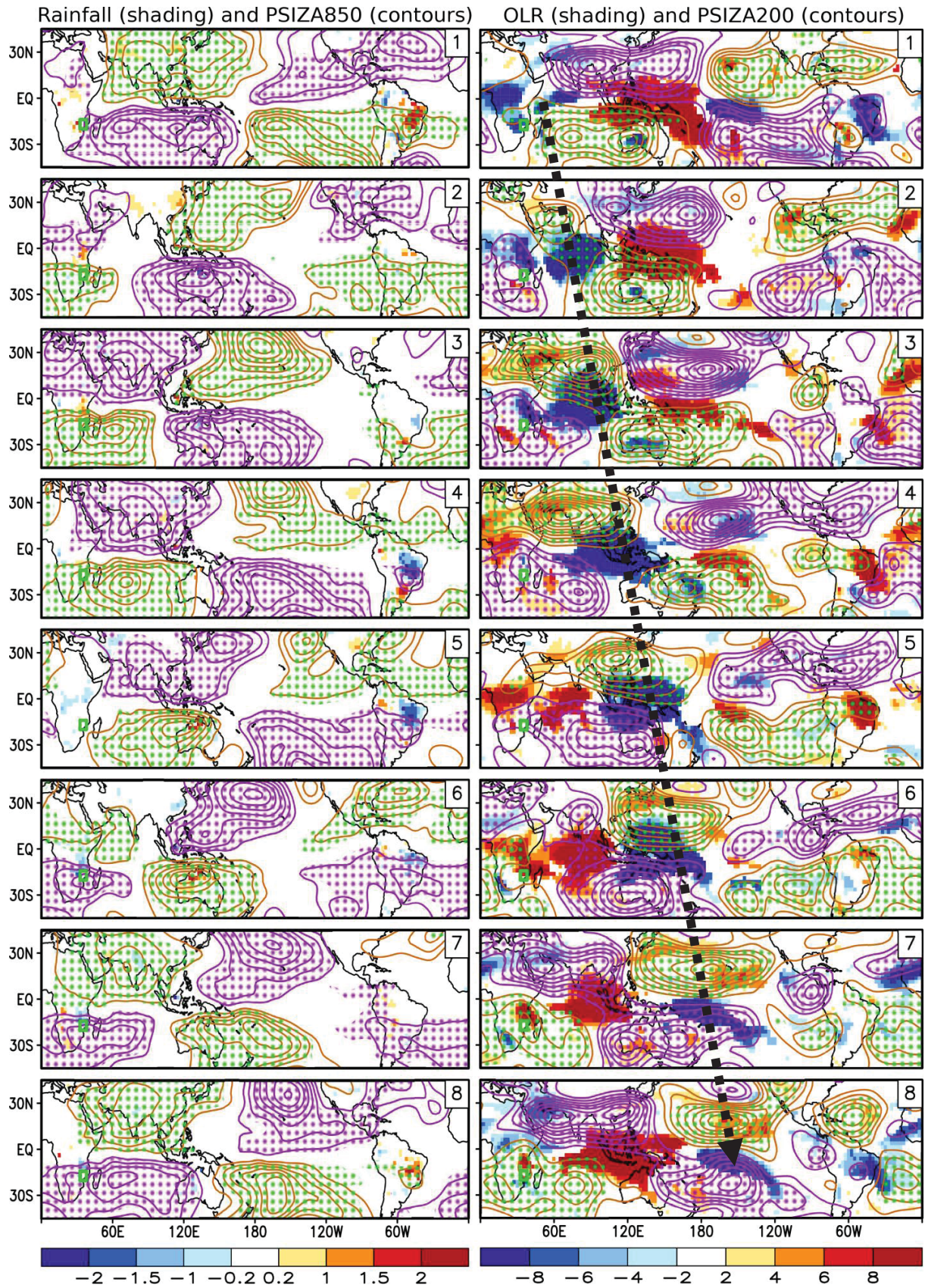
Figure 5 – Composite anomalies of (left panel) precipitation and 850 hPa zonally asymmetric streamfunction (PSIZA850) and (right panel) outgoing long-wave radiation (OLR) and PSIZA200 in each phase of the MJO for DJF season over the 1979–2005. Contour interval is 1.0 x 10^{-6} m^2 s^{-1}, and zero contour is omitted. Dark yellow (purple) contours represent positive (negative) values, with stippled areas indicating anomalies significant with confidence level above 95%. Rainfall (OLR) anomalies are indicated in the bottom colour bar. Only anomalies with confidence level above 95% are shown. The eastward propagating MJO activity as representd by dipole of enhanced (negative OLR) and supressed (positive OLR) convection is illustrated by dotted black line with arrow at end

trains which passing over southeastern SA and the neighbouring Atlantic Ocean and are modulated by convective activity there whereby creating favorable condictions for an enhanced rainfall over SAF days later. Obviously, the MJO impacts on SAF countries are not as extensive as over SA due to the different local features over each SAF country. A good example of that is Mozambique, a country whose rainfall variability mechanisms have been reported to be a little bit different to most of SAF countries, given its coastal location, facing always the warm Indian Ocean, and its long latitudinal extension that makes the country to be affected by both tropical and subtropical weather systems or the interaction of both systems (MANHIQUE, 2008).

2.4 Oceanic factors affecting the variability of regional rainfall

SAFM rainfall has marked variability on timescales ranging from daily (synoptic) to intraseasonal and interannual to interdecadal and longer scales. Many important physical mechanisms associated with the variability on each aforementioned timescale have been disclosed in a number of studies carried out during the most recent 3–4 decades or so.

As the variability of SAFM at interannual scale is currently deemed to be fairly well understood (e.g., MAKARAU, 1995; MANHIQUE, 2008), we here provide only a brief description of it to give the readers some idea of how low-frequency modes can affect the high-frequency ones.

On interannual timescale, SAFM rainfall variability has been attributed to a number of factors, chief among them being ENSO, especially since the late 1970s (RICHARD et al., 2000). During the positive (negative) ENSO phases, referred to as an El Niño (La Niña) episodes, seasonal SAF rainfall tends to be below (above) normal. The dry conditions over the region during an El Niño event is associated with an eastward shift in the SICZ (where preferentially

develop the TTTs) in response to warm sea surface temperature (SST) anomalies over the western Indian Ocean (NICHOLSON and KIM, 1997) or to atmospheric Rossby waves (COOK, 2001), that modifies the regional mid-tropospheric vertical motions and hence precipitation anomalies over SAF (HOELL et al., 2017). El Niño events also lead to northward shift of the subtropical highs which is associated with anticyclonic anomalies over the subcontinent, restricting wind inflows toward SAF, and hence suppression of convection or decrease in precipitation relative to the average in the region (HOELL et al., 2015; REASON and JAGADHEESHA, 2005). Despite the connection between ENSO and SAF rainfall, it is important mentioning that not all El Niño events lead to dryness in SAF (FAUCHEREAU et al., 2009; LYON and MASON, 2007). A good example of such nonlinearity is the 1997–1998 super El Niño, whose expected widespread drought conditions over SAF failed to materialize, as the seasonal rainfall in some SAF regions have been observed to be near or above average (RICHARD et al., 2001). This calls for further investigations in order to better understand the causes by which, in the recent years, some El Niño episodes have not been accompanied by droughts over SAF. Although interesting, this is not the issue of the present thesis.

(Multi)decadal variability, such as the interdecadal Dyer–Tyson cycle (18 years; DYER and TYSON, 1977) and the quasi-decadal cycle (10 years; TYSON, 1981) have also been identified in SAF seasonal rainfall, and those have been interpreted as a chaotic resonance of interannual variability (MASON, 1990; REASON and ROUAULT, 2002), implying that decadal forcing may appear similar to that driven by ENSO at the interannual scale.

More recently, using the Climate Reasearch Unit time series data version 3.23 (HARRIS et al., 2014), Dieppois et al. (2016) have revisited the long scale variability leading modes in SAF rainfall. Those authors have identified through the wavelet analysis three significant timescales of variability during both austral summer and winter seasons: interannual variability (2–8 years), quasi-decadal variability (QDV; 8–13 years), and interdecadal variability (IDV; 15–28 years), the two latter are similar to Dyer–Tyson cycles mentioned above. While the first time scale confirms the predominant influence of ENSO (e.g., REASON et al., 2000), QDV and IDV were found to exhibit ENSO-like patterns interpreted as the signature of the interdecadal Pacific oscillation (IPO) and the Pacific decadal oscillation (PDO), respectively. The large-scale forcings associated with the aforementioned variability modes act to shift the SICZ in an

abnormally eastward location under warm conditions in the Pacific, and hence modifying the TTTs preferential location (DIEPPOIS et al., 2016).

In addition to the remote influence of these large-scale climate variability modes, SAFM rainfall is also influenced by variability modes located in the Atlantic and Indian Oceans (NICHOLSON and KIM, 1997). In the Atlantic Ocean, off Angola and northern Namibia, the so-called Benguela Niños, which seem to be forced in response to an anomalous convection over SA (GRIMM and REASON, 2011), can influence regional seasonal rainfall (HERMES and REASON, 2009; REASON and SMART (2015). In the Indian Ocean, the subtropical Indian Ocean dipole (SIOD; BEHERA and YAMAGATA, 2001) is also related to SAF rainfall (HOELL et al., 2017; REASON, 2001, 2002). The Indian Ocean on its own can also modulate SAF rainfall (WASHINGTON and PRESTON, 2006), especially the nearby southwest Indian Ocean (SWIO; REASON, 1998; REASON and MULENGA, 1999). The SST anomalies over the Indian and Atlantic Oceans, acting individually or in concert can be affected by ENSO episodes, which in turn modulate the effects of the former on regional seasonal rainfall (e.g., HOELL et al., 2017; NICHOLSON and KIM, 1997; REASON et al., 2006). For instance, Hoell et al. (2017) argued that when the SIOD and ENSO are in opposite phases, the SIOD complements the ENSO-related atmospheric response over SAF by strengthening the regional equivalent barotropic Rossby wave, anomalous mid-tropospheric vertical motions and anomalous precipitation. The opposite is true when the SIOD and ENSO are in the same phase. Similarly, Nicholson and Kim (1997) have early reported that atmospheric teleconnections during La Niña (El Niño) are more sensitive to SST forcing over the Atlantic (Indian) Ocean.

The impacts of these low-frequency variability modes on high-frequency ones are now undogoing rigorous scrutiny and some important and encouraging results are just emerging. These include the findings suggesting modulation of ENSO impacts on TTTs and its associated cloudbands by (multi)decadal climate variability modes (DIEPPOIS et al., 2016; DYER and TYSON, 1977; MASON and JURY, 1997; POHL et al., 2018). This knowledge is likely to improve that at subseasonal through the categorization of the number of dry/wet days within the season that can be used as indicators of monsoon dry/wet episodes.

3 Data and methods used in this study

3.1 Data

As stated in the introduction chapter, the results of this thesis are organized in form of two papers which together address the proposed research objectives as outlined in sections 1.3. In this context, some datasets used in the first paper are not used in the second paper and vice-versa. To put it clear, the description of overall datasets used in this thesis is presented into two subsections, one for the first paper, on intraseasonal variability of southern Africa monsoon rainfall and monsoon indices (subsection 3.1.1), and the other one for the second paper, on subseasonal prediction skill assessment of SAFM anomalies (subsection 3.1.2).

3.1.1 Data used in first paper (hereafter referred to as paper01)

The gauge daily rainfall (closed blue triangles in Fig. 3b), provided by Mozambique National Institute of Meteorology (INAM), is used as the basic data for determining intraseasonal variability modes for the period 1979–2005. These data were initially submitted to quality control process for identification and removal of spurious values, following the procedures described in Grimm and Saboia (2015) and Liebman and Allured (2005). One of these procedures includes identifying in each station series the days with either blanks or negative values, which are replaced by the missing data code (777.7). After that, these data were then interpolated on a 1° x 1° grid resolution, in the center of which were located the average daily rainfall time series, obtained from all available stations with at least 70% of nonmissing data within the considered grid box. Notwithstanding a slight spatial smoothness introduced in the data by the interpolation, this method produces a dataset, distributed more evenly over the study area.

In the composite analysis whose definition is given in the method section (2.3), the daily Climate Prediction Center (CPC) unified gauge-based precipitation dataset at 0.5° grid resolution (CHEN et al., 2008) is used to provide a larger scale picture and the origin of the rainfall anomalies before they reach their maximum values in Mozambique, since the INAM data do not cover all SAF. The CPC dataset is a blended product, composed of daily summary files from the

Global Telecommunication System, and the CPC unified daily station data across the globe. Since the CPC data do not cover oceans regions from where rainfall anomalies may also originate, additionally, the OLR retrieved from the National Oceanic and Atmospheric Administration (NOAA) polar-orbiting series of satellites with daily temporal resolution and 2.5° horizontal resolution (LIEBMANN and SMITH, 1996) is used.

Seasonal mean summer rainfall over the SAF is obtained with 0.5° grid resolution monthly Global Precipitation Climatology Center (GPCC) data, extending from 1891 to 2016 (SCHNEIDER et al., 2016). This dataset is based on data over 75,000 stations globally and includes extensive quality control and weather-dependent corrections for gauge undercatch. The use of GPCC instead of CPC precipitation in SAF summer climatology description is due the fact that the former exhibits a realistic maximum over Mozambique monsoon core region, corroborating that shown in Mchugh and Rogers (2001) and the pattern of annual mean rainfall, displayed in Nicholson (2000).

For circulation analysis we use 2.5° gridded daily zonal (U) and meridional (V) wind components at lower (850–hPa) and upper (200–hPa) levels, both derived from the National Centers for Environmental Prediction (NCEP)/National Center for Atmospheric Research (NCAR) Reanalysis products (KALNAY et al., 1996).

Additionaly, the stream function (PSI), which is computed from both U and V is also considered here for assessment of the global rotational circulation response to anomalous heat sources in the atmosphere. Here we display only the zonally asymmetric part of PSI (PSIZA), which is obtained by removing the zonal mean (averaged on each latitude). The PSIZA enhances the wave-like structures in propagating Rossby waves (Hsu and Lin 1992; Held et al. 2002). The PSIZA considered here is that at 200 hPa (PSIZA200), the level in which the wave-like patterns are clearer and more intense.

The data just described and those presented in next subsection (3.1.2) are used in the form of anomalies in all analyses presented, except in that of mean climatology pattern.

The daily anomalies at each grid point are calculated following similar procedures used in Grimm (2019) and SG20. The procedures consist in calculating at each grid point, the average daily values for January 1st through December 31st, which are then smoothed with a 31-day moving average to produce the smoothed climatological annual cycle, since there is much spurious variance in nonsmoothed annual cycle of average daily values due to the relatively short

sample. It is worthy mentioning here that in climatological annual cycle the smoothness of the first (last) 15 days in January (December) is made using partly the days from December (January). Then, the smoothed climatological annual cycle at each grid point is subtracted from the daily raw values in the corresponding grid box, to obtain the anomalies.

3.1.2 Data used in second paper (hereafter referred to as paper02)

In this paper, the period used for the S2S models reforecast and observed (reference) data is their common period 1999–2010 of reforecasts.

To avoid repeating information, the description of these data is presented in the paper02 (Chapter 5). However, it is worthy mentioning here that due to the need to make the S2S analysis for a larger sample (1999–2010), rather than a smaller one (1999–2005), and hence, increase the reliability of the study in paper02, the 0.5° grid resolution CPC daily rainfall is considered as observed precipitation due to unavailability of Mozambique gauge precipitation after 2005 to the authors. The use of CPC among all other alternative gridded datasets is due the fact that it shows a relatively good correspondence with Mozambique gauge precipitation (SG20).

In Fig. 6 the illustration of the location of contributing centers to S2S database and the main features of this project data is provided, whereas the summary of the data described in sections 3.1.1 and 3.1.2 is given in Table 1.
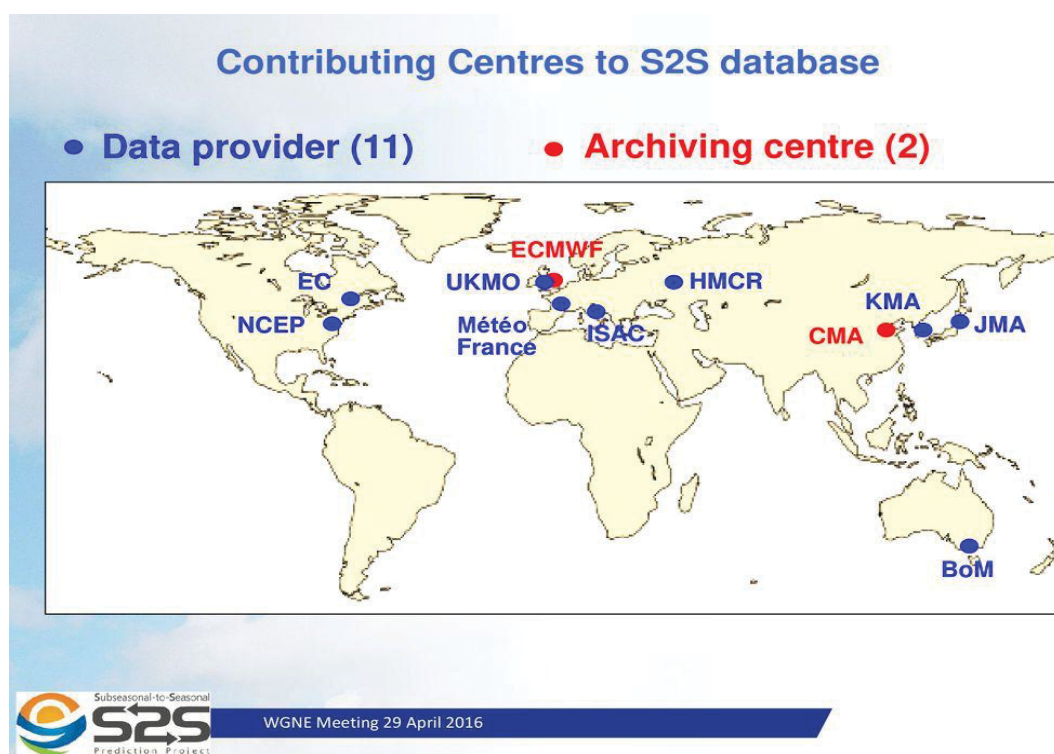
Figure 6 – Map illustrating the location of the contributing centers to S2S database

Source: Vitart (2016, personal communication, https://slideplayer.com/slide/13038775/)

Table 1 A summary of data used in the present thesis

Data	Variables	Spatial resolution	Temporal resolution	Period	Origin/source	Papers 01	02
Gauge	P	1° x 1°	daily	1979–2005	INAM	x	
GPCC	P	0.5° x 0.5°	monthly	1979–2005	Schneider et al. (2016)	x	
CPC	P	0.5° x 0.5°	daily	1979–2010	Chen et al. (2008)	x	x
NOAA	OLR	2.5° x 2.5°	daily	1979–2010	Liebmann; Smith (1996)	x	x
NCEP/NCAR	V(u,v)	2.5° x 2.5°	daily	1979–2010	Kalnay et al. (1996)	x	x
S2S outputs	V(u,v), OLR, P	1.5° x 1.5°	daily	1999–2010	Vitart et al. (2017)		x

P denotes precipitation. It is given in $mm\ d^{-1}$ for INAM, CPC, and S2S data, whereas for GPCC in $mm\ month^{-1}$. V(u,v) and OLR are given in $m\ s^{-1}$ and $W\ m^{-1}$, respectively. The letter "x" indicates that the data was used either in paper01 (1979–2010) or paper02 (1999–2010) or in both papers.

3.2 Methods

Although the datasets used in both papers are not identical, the methods applied for the analyses are almost similar. Some of these methods include Lanczos band-pass filter, principal component analysis (PCA), power spectral density (PSD), Pearson correlation coefficient (PCC or r) analysis and composite analysis (CA). The both latter were applied in both papers, while the formers in paper01.

3.2.1 Lanczos band-pass filter

As this study focuses on ISV, the extraction of different intraseasonal bands in rainfall anomalies (see their description in section 3.1.1) was made using the Lanczos band-pass filter (DUCHON, 1979). The main goal of the Lanczos filter is to transform an input data sequence x_t (where t is time) into newer (an output) data sequence y_t using a linear relationship (1):

$$y_t = \sum_{k=-\infty}^{+\infty}(w_k\, x_{t-k}) \tag{1}$$

in which the w_k indicates suitably chosen weights or the weight function.

The relationship between the input (X(f)) and output data (Y(f)), where f is frequency, is obtained by taking the Fourier transform of (1). As a result, we get the following relationship (2):

$$Y(f) = R(f).X(f) \tag{2}$$

in which R(f) denotes the frequency response.

The w_k and R(f) comprises a Fourier series transform pair such that:

$$R(f) = \sum_{k=-\infty}^{+\infty} w_k\, exp(2ikf\pi\Delta) \tag{3}$$

$$w_k = \frac{1}{2f_n} \int_{-f_n}^{f_n} R(f)\, exp(-2ikf\pi\Delta)df \tag{4}$$

Where k = -n, …, 0, …., n; Δ is the sampling interval and f_n the Nyquist frequency with value 0.5 cycle per data interval.

For band-pass filter, w_k is given by relationship (5), whereas the R(f) is the same as in (3):

$$w_k = \left(\frac{\sin 2\pi f_{c2} k}{\pi k} - \frac{\sin 2\pi f_{c1} k}{\pi} \right) \tag{5}$$

where f_{c1} and f_{c2} are the cutoff frequencies in the chosen band, which in this study are 10 and 90 days, besides 10 and 25 days and 20 and 90 days.

The minimum number of weights required for Lanczos band-pass filter is given by (6):

$$n \geq \frac{1.3}{f_{c2} - f_{c1}} \tag{6}$$

Selecting a time scale for filtering requires a good choice of number of weights (MACAMBACO, 2016). As in Macambaco (2016) we used in this study 211 weights.

The advantage of the Lanczos filter is its ability to be easily adjusted to the band of interest by adjusting the cutoff frequencies f_{c1} and f_{c2}.

3.2.2 Principal component analysis (PCA)

Large datasets are increasingly common and are often difficult to interpret (JOLLIFFE and CADIMA, 2016). This is particularly true for weather/climate datasets.

In order to reduce the dimensionality of such datasets, increasing interpretability but at the same time preserving as much 'variability' (i.e. statistical information) as possible, Empirical Orthogonal Function (EOF) analysis, also referred to as principal component analysis (PCA) which was firstly introduced by Pearson (1901) and, developed independently by Hotelling (1933) is among the most widely and extensively used methods in atmospheric science. This method became popular for analysis of atmospheric data following the paper by Lorenz (1956), who called the technique EOF analysis.

The central idea of PCA consists mainly in decomposing a larger possibly correlated set of datasets (the set of gridpoints in our case) into a smaller, linearly uncorrelated and orthogonal ones termed variability modes (which are the function of the spatial domain and the time period being used), while losing only a small amount of original information (JOLLIFFE and CADIMA, 2016; WILKS, 2011).

The computation of PCA can be specified in at least six basic operational modes (O, P, Q, R, S), depending on which parameters are chosen as variables, individuals and fixed entities (RICHMAN, 1986). These six modes will result in a unique clustering of variables when simple structure rotation (e.g., varimax, RICHMAN, 1986) is applied. In studies of meteorological fields which are given in space and time, there are three entities: a meteorological field (rainfall in our case), time and a location or space (grid points). In this perspective, a PCA of a meteorological field can therefore be performed by varying any two of these three entities and holding the third fixed. PCA calculated by fixing space (time) is said to be computed in S-mode (T-mode).

In S mode, which was used in this study, grid points are represented by columns and time by rows, the inverse is true for T mode. Furthermore, in S mode, rotation (e.g., varimax) which is needed to make the modes physically more interpretable tends to isolate subgroups of gridpoints which covary similarly, so that their results are used for identification of homogeneous regions with respect to time variability. Conversaly, in T mode, rotation isolates subsets of observations with similar spatial patterns and, thereby, simplify the time series (RICHMAN, 1986).

As PCA can be performed using either the covariance or the correlation matrices, here we use the latter one, which accounts for different standard deviations in the data, although the covariance matrix showed similar results in term of absolute values.

Based uppon the explanation above, we applied the S-mode PCA using correlation matrix (7) applied to each intraseasonal band data described in section 3.2.1 to identify the variability modes (EOFs) of precipitation in the respective intraseasonal time bands over Mozambique.

$$\boldsymbol{R} = \frac{1}{n-1}\, Z^T Z \tag{7}$$

Where $\mathbf{R}$ denotes correlation matrix (symmetric matrix), $\mathbf{Z}$ indicates the matrix of standardized anomalies, while $\boldsymbol{Z^T}$ denotes transposed matrix of $\mathbf{Z}$. All matrixes have n rows representing the number of time data samples and k columns representing the number of grid points.

From this matrix we get through an eigenanalysis the k eigenvalues (λ_k) and their corresponding eigenvectors ($\mathbf{e}_m$) (Equations (8) and (9), respectively):

$$\lambda_1 \geq \lambda_2 \geq, ..., \geq \lambda_k \tag{8}$$

$$e_m^T = [\, e_{1m}, e_{2m}, ..., e_{km}\,] \tag{9}$$

Where m = 1,2,3,…,k.

The eigenvalues and eigenvectors describe respectively the variance and direction of the variability modes. Recall that the set of eigenvectors, and associated eigenvalues, represent a coordinate transformation into a coordinate space where the matrix **R** becomes diagonal.

The principal components (PC, also termed factor scores) which is the new time series is obtained by projecting a single eigenvector onto the original data to get an amplitude of this eigenvector at each time. As the eigenvalues represent the variance explained by each variability mode, the PCs are thus ordered by the fraction of the variance they explain, i.e. the first principal component (PC1) accounts for the largest variance in the dataset, then, the second one (PC2) accounts for most of the remaining variability in the dataset, and so on, under the constraint that succeeding PC is uncorrelated and orthogonal to the preceding ones. For each variability mode in each frequency band, the spatial pattern (factor loadings or EOFs) associated with the PCs is obtained by correlating the PC with rainfall anomalies in the corresponding band over the domain grid points. Thus, in so doing, PCA yields information describing both spatial patterns (EOFs) and temporal variations (PCs) of variance experienced in the original dataset.

One of the most important decisions to be taken during the PCA implementation is the number of PCs to be retained (e.g., RICHMAN, 1986), since inadequate PC's extraction makes it impossible to interpret appropriately the results (e.g., EHRENDORFER, 1987; MANATSA et al., 2011). Note that, there is no theoretical grounds for or any general agreement on the cut-off hypothesis, but experience suggests that it is reasonable to consider a number that fix the amount of represented variance as much as possible (e.g. 80%; HANNACHI et al., 2007; HARRISON, 1984b). With this in mind in the present study, the first 5 PCs explaining over 60% of the original variance, were retained using the Kaiser criterion of cutting-off PCs with eigenvalue greater or equal to one (KAISER, 1958).

Since unrotated modes may be nonphysical or spurious ones, the varimax orthogonal rotation (Equation 10), the most well-known and used rotation algorithm was applied, which maximizes the local variance within the domain, and makes the modes physically more interpretable (RICHMAN, 1986).

$$V^* = \frac{n \sum_{i=1}^{n} (b_{ij}^2)^2 - (\sum_{i=1}^{n} b_{ij}^2)^2}{n}, \qquad j = 1, \dots, r \qquad (10)$$

Where n is the number of variables (gridpoints in our cases), r is the number of PCs retained for rotation, and the b_{ij} are the eigenvectors.

The EOFs obtained after rotation are termed REOFs (rotated EOFs). For a more detailed description on the PCA including its application to meteorological and climatological variables we refer the readers to Ehrendorfer (1987), Hannachi et al. (2007), Wilks (2011), among others.

3.2.3 Power sprectral density (PSD)

In climatic variability studies, besides knowing the leading patterns in the dataset, it is also important to check which cycles are present in the data. This information is of practical importance in water resources, since by detecting the approximate periodicity of a precipitation pattern, it is possible more precisely to plan and operate a hydroelectric system. If in a given region, it is known that there is a strong oscillation in precipitation with a period for example of 60 years or so, it is possible to prepare in advance for three drier decades and other wetter (SABOIA, 2010).

There are several methods used to detect the presence of cycles and their frequencies in a time series. One of this, and used in the present study, is power spectral density (PSD) whose computation follows the Blackman-Tukey approach that estimates the spectral power through the Fourier Transform of the autocorrelation function (e.g., MITCHELL et al., 1966).

To apply this method, it is desirable that the series be periodic. This condiction is satisfied by applying a cosine temporal window as shown in Equations (11) and (12).

$$x' = x_i 0.5[1 - \cos\frac{(i-1)\pi}{0.1N}], \quad (1 \geq i \leq 0.1n) \tag{11}$$

$$x' = x_i 0.5[1 - \cos\frac{(N-1)\pi}{0.1N}], \quad (0.9N \geq i \leq N) \tag{12}$$

where N is the number of terms in the series, i is an individual sample point index, x the original series and x' the series after the application of the window.

The autocorrelation function is the correlation coefficient of a time series with itself, shifted in time by a lag. In discrete variables, it is defined by Equation (13), as follows:

$$C_i = \frac{1}{n-i} \sum_{i=1}^{n-i} x_i x_{i+i} \tag{13}$$

where C_i is autocorrelation for lag l, n is the number of terms in the series, i is an individual sample points index and, x_i is a time series with null mean.

PSD or G_h is accordingly estimated by Equation (14) as follows:

$$G_h = 2\Delta t[C_0 + 2\sum_{i=1}^{m-i} cos\frac{\pi i h}{m} + C_0 cos\pi h] \tag{14}$$

where G_h is the PSD estimator (hereafter referred to as PSD) corresponding to the harmonic h, Δt is the timporal interval between one term and other in the time series and, m is the maximum lag.

The maximum lag in which the spectrum is essentially constant must be chosen. The maximum lag (m) is the maximum width of the time window to be evaluated, which corresponds to the lowest frequency at which the spectral density is estimated, and must not be greater than half of the time series function (MITCHELL et al., 1966).

The maximum lag defines the amount of harmonics (h) analyzed, which in turn are associated with periods (T) and frequencies (f) as shown in (15). The smaller the maximum lag, the smaller the width of the base of the temporal window (and the greater the width of the base of the corresponding spectral window). The narrowing of the base of the temporal window causes an ever greater distortion between the estimated value of the spectral density and the true value. Therefore, it is necessary to seek a balance between the variance of the estimator and the real spectrum and fidelity (or resolving power) (MITCHELL et al., 1966).

$$T = \frac{2m\Delta t}{h} \tag{15}$$

To determine the statistical significance of spectral estimates, a null hypothesis which is theoretical spectrum of a stochastic process is adjusted to the estimated spectrum as described in Mitchell et al. (1966). The white noise spectrum can be used for instance as a null hypothesis, if the first order autocorrelation is not significantly different from zero. Otherwise, the spectrum of red noise can be considered (WILKS, 2011).

In this thesis as in Silva (2018), the theoretical spectrum of a first-order autoregressive process, as described by (16), is considered:

$$S_h = \bar{s}[\frac{1 - \rho_1^2}{1 + \rho_1^2 - 2\rho_1 cos\frac{\pi h}{m}}] \tag{16}$$

where h = 0,…,m are the harmonics and m the maximum lag. ρ_1 is the first-order autocorrelation of the series, $\bar{s}$ is the average of the spectral estimates and corresponds to the ratio of the

magnitude of the spectral estimate (PSD) to the local magnitude of the theoretical spectrum of white noise.

It is important to note that if the first-order autocorrelation of the series is very small, the (16) tends to the theoretical spectrum of white noise (the straight line). The confidence limits of the results are the product of the value of the null hypothesis in any harmonic h by the test statistic, which corresponds to the ratio of the magnitude of the spectral estimate to the local magnitude of the continuum (MITCHELL et al., 1966). This ratio has been found to be distributed as chi-square devided by degrees of freedom (χ^2/ν), where $\nu = \frac{2N - m/2}{m}$.

Recall that PSD analysis in this study was applied to REOFs time series to determine the prevailing period in the modes of each time band (see text in sections 3.2.1 and 3.2.2). The total length N of the REOFs time series, composed of the sequence of DJF days over the 1979–2005 period (with leap days excluded), was extended by a 5*N padding applied to each end of the series and the maximum lag used was 1/5 of the resulting series, consistent with Silva (2018).

The 0.05 and 0.01 significance levels were computed to determine the significance of the most prevailing periods.

3.2.4 Pearson correlation and composites analyses

While a correlation analysis can help identifying relationships between two variables that can indicate areas where research should be taken to show further results, composite analysis can properly tell a powerful story about how that meteorological phenomenon (either wet or dry periods) is affected by the variables used in the composite stratification.

A brief explanation of the implamentation of both methods follows below:
The Pearson correlation coefficient (PCC or r; Equation 17) is the ratio of the sample covariance of the two variables (x and y) to the product of their standard deviations (WILKS, 2011):

$$r_{x,y} = \frac{\sum_{i=1}^{n}(x_i - \bar{x})(y_i - \bar{y})}{\sqrt{\sum_{i=1}^{n}(x_i - \bar{x})^2 \sum_{i=1}^{n}(y_i - \bar{y})^2}} = \frac{Cov(x,y)}{\sigma_x \sigma_y} \tag{17}$$

where x_i and y_i denote the individual sample points indexed with i; n indicates the sample size; $\bar{x}$ and $\bar{y}$ – the means of variable x and y, respectively; Cov – the covariance, whereas σ_x and σ_y – the standard deviation of variable x and y, respectively.

The correlation coefficient ranges from −1 to 1. A value of 1 implies that the equation (17) describes the relationship between x and y perfectly, with all data points lying on a line for which y increases as x increases. On the other hand, a value of −1 implies that all data points lie on a line for which y decreases as x increases, whereas a value of 0 implies that there is no linear relationshp between the x and y variables.

In essence, the PCC measures the linear relationship degree between x and y variables. The significance of computed PCC is assessed using the Student's t test, in which the underlying null hypothesis is that the PCC between x and y variables is null.

Composite analysis (CA), also referred to as conditional sampling analysis was originally developed by Chree (1913, 1914) in space science, and now it is widely-used in various fields of earth science including Meteorology. CA is a useful tool to help understand the relationships among different phenomena (XIE et al., 2017) occuring over time that are difficult to observe in totality. In studying climate, CA adequately helps exploring the large scale impacts for example of the well known teleconnection patterns (e.g., El Niño) on the weather/climate over a given geographical area.

The computation of composite is implemented as follows: supposing that we want to investigate the large scale circulation anomalies associated with intraseasonal rainfall variability represented by an area averaged standardized daily rainfall anomaly index I (Fig. 7), at first, we set to the index I timeserie a threshold say of +(−) 0.7 standard deviation (green line) above (below) which the events or days are regarded being in a positive (negative) phase, whereas those in between −0.7 and +0.7 standard deviation are considered being in neutral or climatological phase. Similar threshold has been applied for example in Grimm and Saboia (2015) and SG20, and that showed to be effective in revealing the extremes years in almost all known climate variability modes (e.g., ENSO years), apart from warranting the retention of a reasonable number of events for composite analysis.

Then, we compute the composites for days in each phase by averaging separately the anomalies of a selected meteorological field (e.g., either OLR or PSIZA200) at each grid cell. Finally, to determine the statistical significance of composited anomalies at each grid point, the Student's t test (Equation 18) applied to the data following normal distribution is considered as the DJF rainfall over SAF is assumed to show near-normal distribution (D'ABRETON, 1992).

$$t = \frac{\overline{x_1} - \overline{x_2}}{\sqrt{[(\frac{1}{n_1} + \frac{1}{n_2})\{\frac{(n_1-1)\sigma_1^2 + (n_2-1)\sigma_2^2}{n_1 + n_2 - 2}\}]}} \tag{18}$$

Where $\overline{x_1}$ and $\overline{x_2}$ denote the means of sample 1 (say positive phase days) and sample 2 (say negative phase days), respectively; n_1 and n_2 denote the size of sample 1 and sample 2, respectively; σ_1 and σ_2 represent the standard deviation of sample 1 and sample 2, respectively. The term $n_1 + n_2 - 2$ indicates the number of degrees of freedom (ν) defined broadly in statistics as the number of "observations or pieces of information" in the data that are free to vary when estimating statistical parameters (the mean and the standard deviation in our case).
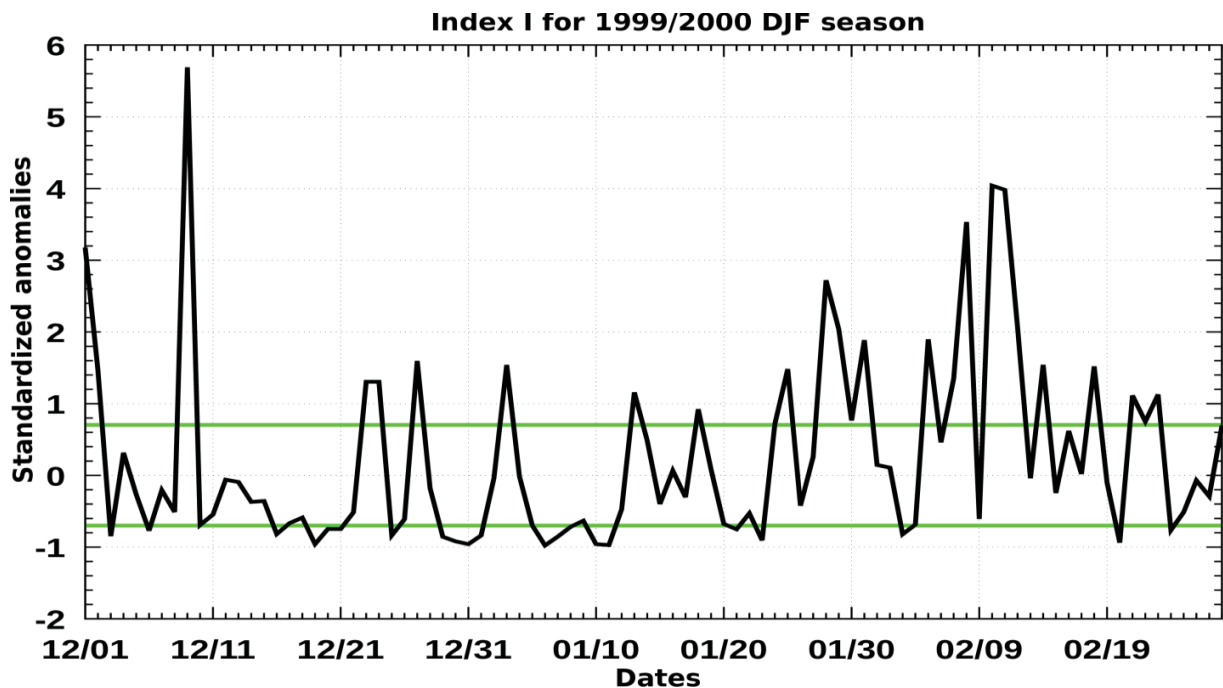
Figure 7 – Example of time series used for definition of positive and negative phases for index I. The positive (negative) phases include days with values above (bellow) the threshold of +(–)0.7 standard deviation represented in figure by solid horizontal green lines. In between the positive and negative phases are neutral (climatological) phases or situation.

The underlying null hypothesis of the test considered in the composite is that there is no difference either between composited anomalies for positive (negative) phases and neutral ones or between composited anomalies for positive phases and negative ones.

For above described Student's t test, a key assumption is that the individual observations composing each of the samples are independent, meaning that a first-order autocorrelation is null, it is to say that is assumed that all the x (or x_1) values are mutually independent and that the

y (or x_2) values are mutually independent, whether or not the data values are paired. However, the atmospheric data often do not satisfy this assumption (WILKS, 2011). To overcome this issue, the effective sample size (n'), equivalent to the number of independent samples has been considered in both correlation and composite analyses using the Equation 19 (WILKS, 2011):

$$n' = \mathbf{n} \frac{(1 - \rho_1)}{(1 + \rho_1)}$$
(19)

Where n and ρ_1 denote the original sample size and the lag-1 autocorrelation, respectively.

It is worthy mentioning here that in Equation 18, n'_1 and n'_2 has been separately calculated for x_1 and x_2 as described in Equation 19.

We also calculate normalized root mean square error (NRMSE) by dividing root mean square error (RMSE, Equation 20) by the standard deviation of observed data, where n in (20) denotes the sample size. NRMSE is calculated to see average magnitude of the forecast errors.

$$RMSE = \sqrt{\frac{\sum_{i=1}^{n}(y_{forecast,i} - y_{observation,i})^2}{n}}$$
(20)

All the methods used in the present thesis are summarized in table 2.

Table 2 A summary of methods used in the present thesis

Sequence	Methods	Source	Papers 01	02
1	Linear interpolation	Meijering (2002)	x	x
2	Descriptive statistic measures (e.g., average, variance and standard deviation)	Wilks (2011)	x	x
3	Lanczos band-pass filter	Duchon (1979)	x	
4	Empirical orthogonal functions (EOFs)	Wilks (2011)	x	
5	Pearson correlation coefficient (PCC)	Wilks (2011)	x	x
6	Normalized root mean square error (NRMSE)	Kim et al. (2016)		x
7	Power spectral density analysis (PSD)	Mitchell et al. (1966)	x	
8	Compositing analysis	Xie et al. (2017)	x	x

For fuller details on each method, the reader is refered to the text in this section (3.2), and in chapters 4 and 5. The letter "x" indicates that the method was used either in paper01 or paper02 or in both papers.

4. Intraseasonal variability of southern Africa summer monsoon rainfall

As was stated in the introduction section, the results of this thesis are presented in the form of two manuscripts, which together address the proposed research objectives. In the present chapter, is attached the first manuscript that focuses on: (1) determination of the leading modes of rainfall intraseasonal variability (ISV) from 1979–2005 Mozambique gauge gridded precipitation anomalies, filtered in three frequency bands (10–25, 10–90 and 20–90 days), which were shosen to give an idea on how these different bands contribute to rainfall ISV over Mozambique; (2) selection of the mode whose spatial pattern is stronger in the monsoon core region (20°S–13.75°S; 32°E–38°E) and whose associated anomalous circulation appears to be more related to variations in monsoon flows; (3) definition of monsoon precipitation index (MPI) calculated over the selected monsoon core region and several low-level monsoon circulation indices, associated whith the MPI, all to characterize the monsoon active (wet) and break (dry) episodes within the rain season. Both the MPI and monsoon circulation indices are calculated separately as area averaged standardized daily anomalies over a previously selected area. The monsoon circulation indices are useful for subseasonal prediction, since models tend to show better performance in predicting circulation than precipitation (MARSHALL and HENDON, 2015). In this part of the research the emphasis was given to large-scale forcing of regional rainfall at the subseasonal timescale, specifically, the teleconnection patterns between SA and SAF, in order to use it as a potential predictor for intraseasonal rainfall anomalies over the latter subcontinent. The results from this paper extend the SAF ISV existing knowledge that is of great importance for agricultural production, water resources management, and subseasonal prediction.

Southern African monsoon: intraseasonal variability and monsoon indices

Kénedy C. Silvério [1,2], and Alice M. Grimm [2,3*]

[1] Higher Polytechnic Institute of Songo (ISPS), Songo-Tete, Mozambique

[2] Postgraduate Program in Water Resources and Environmental Engineering, Federal University of Parana (UFPR), Curitiba, Brazil

[3] Department of Physics, Federal University of Parana (UFPR), Curitiba, Brazil

Kénedy C. Silvério ORCID ID: https://orcid.org/0000-0003-1140-517X

Alice M. Grimm ORCID ID: https://orcid.org/0000-0002-9056-4656

[*] *Corresponding author address*: Department of Physics, UFPR, Caixa Postal 19044, CEP 81531-980, Curitiba, Brazil. E-mail: grimm@fisica.ufpr.br

Southern African monsoon: intraseasonal variability and monsoon indices

Kénedy C. Silvério [1,2], and Alice M. Grimm [2,3*]

[1] Higher Polytechnic Institute of Songo (ISPS), Songo-Tete, Mozambique

[2] Postgraduate Program in Water Resources and Environmental Engineering,

Federal University of Parana (UFPR), Curitiba, Brazil

[3] Department of Physics, Federal University of Parana (UFPR), Curitiba, Brazil

Abstract

Southern African summer monsoon rainfall varies over a range of timescales. Here the emphasis is placed on its intraseasonal variability (ISV), which is of great importance for agricultural production, water resources management, and subseasonal prediction. Rotated modes of ISV are determined based on daily rainfall gauge data (1979–2005) in eastern southern Africa (SAF). One of the leading modes exhibits strongest factor loadings over the region with most intense monsoon precipitation over land and is associated with variations in the monsoon circulation. Its most significant oscillations in different ISV frequency bands exhibit periods around 12, 22-24 and 50 days, also found previously in ISV of monsoon rainfall over South America (SA). The 12-day oscillation is associated with the quasi-biweekly oscillation originated from Rossby waves in the extratropical westerly belt propagating into SAF. The lead-lag composite anomalies keyed to positive and negative phases of the mode in the 20-90 day band confirm a 24 day mode and the influence of the Madden Julian Oscillation. Besides, they indicate the influence of convective anomalies over SA through propagation of atmospheric waves from this continent to SAF. A monsoon precipitation index (MPI) is proposed to help characterizing, monitoring and predicting active and break monsoon spells. It is based on the average standardized precipitation anomaly over a selected area in northeast SAF, where the variability of the precipitation in the core monsoon region over land is strongest not only on intraseasonal but also on synoptic and interannual time scales. Therefore, the MPI reflects the monsoon precipitation variability where its prediction is more useful. Furthermore, monsoon circulation indices are defined based on circulation features most associated with the MPI, since models show better skill in predicting circulation than precipitation.

KEYWORDS: Intraseasonal oscillations, Summer monsoon, Southern Africa, teleconnections, Monsoon indices.

Corresponding author address: Department of Physics, UFPR, Caixa Postal 19044, CEP 81531-980, Curitiba, Brazil. E-mail: grimm@fisica.ufpr.br

1 Introduction

Most of southern Africa (SAF) experiences a seasonal peak of rainfall occurring between December and February (DJF), with the exception of the southwest and south coastal regions (Fig. 1). Although this seasonal peak in summer is a typical monsoon feature, most of SAF was for a long time not considered a monsoon region. According to Ramage (1971), a monsoon regime is characterized by a seasonal reversal of prevailing low-level winds. Although this definition has been accepted by the meteorological community for almost 3 decades, it was contested by Zhou and Lau (1998) and Webster et al. (1998), who qualified monsoon regions in the Americas in terms of rainfall. These works modified the Ramage's monsoon definition to a more general one, by considering seasonal changes in multiple meteorological variables such as rainfall and wind's components, among others. New monsoon definitions characterized recently most of SAF as monsoon region (Wang and Ding 2008; Yim et al. 2014).

Similar to other monsoon regions, the rainfall in southern African monsoon (SAFM) region exhibits significant variability on wide range of time scales (Pohl et al. 2018). This variability results sometimes in extreme events (either floods or droughts) with tremendous impacts on the economies and societies of the region. A good example of these impacts is Mozambique (801,537 km^2), a country in eastern SAF (Fig. 1a). In this country, as in most SAF, rainfall is the life-blood for agricultural and hydropower sectors, known as the backbone for most economies in the region. Mozambique has undergone devastating floods as well as droughts. For instance, the precipitation over 400 mm in 24 hours associated with a set of cyclones, especially the Eline, which occurred over Mozambique, South Africa and parts of Zimbabwe in February 2000 (Reason and Keibel 2004), caused approximately 700 deaths in Mozambique and hundreds of thousands of people displaced. The accumulated property damages resulting from this flood exceeded 600 million USD (Wiles et al. 2005). After these floods, a system of early warning was implemented in the country and several efforts were made at local and regional levels in order to improve the knowledge on climate variability and the forecast skill of such events (Wiles et al. 2005). However, several years later, challenges still remain in accurately predicting such events, as shown by the floods in Mozambique during January 2013 (Manhique et al. 2015), January-February 2015 (OCHA 2015), and March 2019 (INAM 2019; INGC 2019).

Thus, understanding the variations of the SAFM has a great socio-economic importance. In view of that, this study seeks to advance the knowledge on SAFM variability on intraseasonal time scales, in which many risk reduction and disaster preparedness actions for a range of sectors can be taken to minimize the impacts of extreme events. The study is more focused on Mozambique, although the variability disclosed extends to other SAF countries.

One of the sources of rainfall variability at this time-scale is the Madden-Julian Oscillation (MJO), known as the dominant mode of tropical intraseasonal variability (ISV; Madden and Julian 1971). It involves significant variations in tropical convective activity and tropospheric large-scale circulation, with coherent signals in many other variables, propagating eastward around the globe with characteristic period of 30–90 days. Many studies have demonstrated that the MJO influences weather/climate phenomena worldwide and it plays an important role in the coupled atmosphere-ocean system (Zhang 2005, 2013). It is also known that the MJO strongest activity coincides with austral summer season,

94   suggesting its potential influence, for instance, on SAFM rainfall variability (Zaitchik 2017). Therefore,

95   there is enhanced chance for skilful global subseasonal prediction, especially in the global tropics , when it

96   is active.

97   However, relatively few studies linking the MJO to SAFM rainfall variability have been performed to

98   date (e.g., Levey and Jury 1996; Pohl et al. 2007; Macambaco 2016; Macron et al. 2016). This is probably

99   associated with the fact that the most comprehensive study on the MJO across the region (Pohl et al.

100   2007) has reported its relatively weak influence on regional rainfall, explaining 35–40% of all intra-

101   seasonal variance in the outgoing long-wave radiation (OLR), used often as a proxy for convective

102   activity. The relatively weak MJO influence on SAFM rainfall was confirmed in the subsequent study by

103   Pohl et al. (2009). These authors also found that synoptic-scale tropical-temperate-troughs (TTTs;

104   Harrison 1984) have equally likely occurrence during any MJO phase, suggesting that the MJO is only

105   one of the many factors influencing rainfall variability in the region at subseasonal scales. Similar results

106   have been recently reported by Macron et al. (2016) for Madagascar including whole SAF. However,

107   these authors suggested that the relatively weak MJO's influence on SAFM may be related to modulation

108   of its signal by some local features (e.g., topography, surface properties, among others).

109   Although the present study has found relatively weaker peaks of power spectral density (PSD) at

110   MJO's timescales compared with those in the 10–30 day range, composite analysis associated with an

111   important mode of ISV showed that the structure of rainfall and circulation anomalies over SAF is

112   reminiscent of the structure of the MJO in certain phases. This indicates that the existing teleconnection

113   between South America (SA) and SAF, caused by eastward propagating wave trains, is likely modulated

114   by MJO related convective activity over tropical SA, consistent with findings in Grimm and Reason

115   (2015) and Macambaco (2016). Grimm (2019) indicated that the MJO-related anomalies over SA in

116   austral summer can contribute to the initiation of the MJO in the Indian Ocean through equatorial

117   teleconnection and extratropical wave trains in both hemispheres linking SA and the Indian Ocean. The

118   wave train in the Southern Hemisphere passing over SAF is able to impact the rainfall in this region.

119   Therefore, we assume that the MJO influences the regional rainfall. The reason by which the MJO-related

120   influence on SAFM was found weak in a number of previous studies may be the fact that it does not

121   influence the SAFM rainfall directly, but via the teleconnection mechanisms just described. This implies

122   that understanding the processes governing the variability of the SA monsoon system is not only

123   important for SA, but also for SAF. This issue, although interesting, is not the scope of the present study,

124   and those interested are referred to Grimm (2019).

125   The first goal of this study is to analyse the space-time structures of intraseasonal summer

126   monsoon rainfall leading modes (Empirical Orthogonal Functions, EOFs) over SAF, based on rainfall

127   gauge data from eastern SAF, as well as the circulation anomalies behind this variability, and compare

128   them to modes of outgoing longwave radiation (OLR) over a larger domain in SAF found in previous

129   work. To the best of our knowledge, this is the first study to take such approach to the ISV in the region,

130   since previous studies used satellite products. The second goal is to propose precipitation and circulation

131   indices to represent the variability of SAF monsoon, on the basis of climatological information and the

132   ISV. These indices are intended to help characterizing, monitoring and predicting active and break

133 monsoon spells in subseasonal time scale, using models participating in the Subseasonal to Seasonal
134 (S2S) Project (Vitart et al. 2017; Vitart and Robertson 2018).

135   The data and methods used in this study are described in section 2, whereas the seasonal rainfall
136 climatology and its associated circulation are described in section 3. The rainfall intrasesonal leading
137 modes over eastern SAF, their prevailing periods and physical mechanisms associated with each mode are
138 presented in section 4. Section 5 discusses the proposed monsoon indices, based on anomalous
139 precipitation and associated circulation. Summary and concluding remarks are given in section 6.
140
141 **2 Data and methods**
142
143 *2.1 Data*
144
145   The gauge daily rainfall data for the period 1979–2005 (blue triangles in Fig. 1a), provided by
146 Mozambique National Institute of Meteorology (INAM), are used as basic data for determining
147 variability modes. Additionally, the Climate Prediction Center (CPC) unified gauge-based daily
148 precipitation dataset with 0.5° grid resolution (Chen et al. 2008), and daily OLR at 2.5° grid resolution
149 (Liebmann and Smith 1996) are used in a composite analysis to give a larger scale picture of the
150 precipitation (convection) anomalies associated with the temporal evolution of a selected ISV mode and
151 the monsoon precipitation index, since the INAM data do not cover all SAF. The CPC dataset is the only
152 gauge-based daily dataset available from 1979. CPC data are also used in the analysis of the relationship
153 between monsoon indices and summer rainfall over SAF. Seasonal mean climatological rainfall pattern
154 over the SAF is obtained with monthly data from Global Precipitation Climatology Center (GPCC)
155 version v2018 with 2.5° horizontal resolution (Schneider et al. 2016). The use of GPCC instead of CPC
156 precipitation in SAF climatology description is due the fact that the former exhibits a more realistic
157 maximum over the Mozambican monsoon core region, consistent with that shown in McHugh and Rogers
158 (2001) and with the pattern of annual mean rainfall, displayed in Nicholson (2000).

159   For circulation analysis we use 2.5° gridded daily zonal and meridional wind's components at lower
160 (850–hPa) and upper (200–hPa) levels, both derived from the National Centers for Environmental
161 Prediction (NCEP)/National Center for Atmospheric Research (NCAR) Reanalysis products (Kalnay et
162 al. 1996). This reanalysis has been used for calculating the MJO phases (Wheeler and Hendon 2004) and
163 the MJO impacts on Australia and SA with coherent results (e.g., Wheeler et al. 2009; Grimm 2019).

164   This study concentrates on the DJF season, which is the peak monsoon season over the region with
165 highest monsoon rainfall over SAF (cf. Figs. 1b, 2a), and during which the influence of global variability
166 modes such as the El–Niño Southern Oscillation (ENSO) and MJO, among others, is stronger (Mason and
167 Jury 1997; Zaitchik 2017). The period 1979–2005 was chosen for providing good data coverage over
168 eastern SAF, and because CPC and reliable OLR data are available only after 1978.
169
170 *2.2 Methods*
171
172   The gauge data over SAF (Fig. 1a) are verified for spurious values, following the procedures

173   described in Grimm and Saboia (2015) for SA data. These data are interpolated to a 1° grid, using the
174   stations with at least 70% of the daily data in the period 1979–2005. In this way the rainfall data are
175   distributed more evenly over the study area. After that, daily anomalies at each grid point are calculated
176   following similar procedures used in Grimm (2019). For each grid point, the average daily values for
177   January 1st through December 31st are calculated and then smoothed with a 31-day moving average to
178   produce the climatological annual cycle, since there is much spurious variance in the annual cycle of
179   average daily values due to the relatively short sample. The climatological annual cycle at each grid point
180   is then subtracted from the daily values in the corresponding grid box, to obtain the anomalies. The same
181   procedure for calculating anomalies is applied to CPC, OLR and NCEP/NCAR data. These anomaly time
182   series at each grid point are submitted to a Lanczos band-pass filter with 211 weights (Duchon 1979), to
183   retain intraseasonal fluctuations in three selected frequency bands (10–25 day, 10–90 day and 20–90 day),
184   and to analyse their contribution to ISV over the study domain. Only the DJF season is separated from the
185   filtered data and used in the analyses.

186   In order to identify the variability modes of precipitation in each time band, principal component
187   analysis (PCA, e.g., Jolliffe 2002; Wilks 2011) is performed in S-mode using correlation matrix, which
188   accounts for different standard deviations in the data, although the covariance matrix showed similar
189   results. For each variability mode in each frequency band, the spatial pattern (factor loadings) associated
190   with the principal component (PC, also termed factor scores) is obtained by correlating the PC with
191   rainfall anomalies in the corresponding band over the domain grid points. Since unrotated modes may be
192   nonphysical or spurious modes, the varimax orthogonal rotation is applied, which maximizes the local
193   variance within the domain, and makes the modes physically more interpretable (Richman 1986). The
194   first 5 PCs, explaining over 60% of the original variance, were retained for rotation, using the Kaiser
195   criterion of retaining PCs with eigenvalue greater or equal to one (Kaiser 1958).

196   To determine the prevailing period in the modes of each time band, PSD analysis is applied. The
197   computation of PSD follows the Blackman-Tukey approach, as described in Mitchell et al. (1966). The
198   total length N of the REOFs time series, composed of the sequence of DJF days over the 1979–2005
199   period (with leap days excluded), is extended by a 5*N padding applied to each end of the series and the
200   maximum lag used is 1/5 of the resulting series. A chi square test variant, as described in Mitchell et al.
201   (1966), is used to determine whether a PSD is significantly different from the null hypothesis of red noise.
202   The 0.05 and 0.01 significance levels were computed to determine the significance of the most prevailing
203   periods.

204   In order to understand the time-evolution of rainfall and circulation anomalies associated with the
205   modes, anomaly composites of rainfall, OLR, and circulation fields at lower (850 hPa) and upper (200
206   hPa) levels are prepared for the positive and negative phases of the modes (and their difference) as well as
207   for the days preceding and following these phases. The positive (negative) phase comprises days in which
208   the factor scores are equal or above (below) +0.7 (–0.7) standard deviation. The significance of the
209   anomalies (and their difference) is assessed using Student's t test, in which the effective sample size at
210   each grid cell is reduced by considering the autocorrelation introduced in the series by the filter (Wilks
211   2011).

212   To facilitate the prediction and monitoring of active and break monsoon episodes, a monsoon

213 precipitation index (MPI) and associated large-scale circulation indices are proposed. The MPI is defined
214 as the averaged standardized rainfall anomaly over the region shown in Fig. 1b, selected for its high
215 monsoon precipitation and variability associated with variations in the main features of the SAF monsoon
216 circulation. The computation of the daily values of these indices follows the same procedure as described
217 above, added by the calculation of the annual cycle of the daily standard deviations for each of the 365
218 days in the same way as the annual cycle of daily precipitation, in order to standardize the daily
219 anomalies. Active (break) monsoon episodes are defined whenever the MPI values are equal or above
220 (below) to +(–) 0.7 standard deviation. The circulation indices are defined according to the correlation of
221 MPI with meridional and zonal components of the low level wind.

3 Climatology analysis

225 The SAFM rainfall structure and its circulation system is discussed in several studies (e.g.,
226 Taljaard 1986; Mason and Jury 1997; Nicholson 2000; Reason et al. 2006; Silverio and Kulikova 2011,
227 among others). Therefore, only background information needed for this study is reviewed. Figure 2a
228 shows the DJF seasonal mean rainfall. For the same period are displayed circulation fields, illustrated by
229 streamlines at lower (Fig. 2a) and upper (Fig. 2b) levels, derived from NCEP-NCAR daily reanalysis
230 products. It is evident that seasonal mean distribution of rainfall over SAF is extremely uneven,
231 increasing from south to north and from the western to the eastern coast. An elongated area of maximum
232 rainfall along the northwest–southeast (NW–SE) direction is evident in central-east SAF, extending over
233 Madagascar (Fig. 2a), and seems to be associated with the interaction of three low-level air flows: (1) the
234 northeasterly monsoon (NEM), originating in the Indian subcontinent, (2) westerly or northwesterly
235 monsoon (NWM), formed by recurved air flows from the eastern flank of the South Atlantic High (SAH)
236 and from the eastern equatorial Atlantic, and (3) the southeast trade winds (SETW), originating from the
237 South Indian Ocean High (SIH). The NWM is conducted by the Angola Low (AL) into the interior, where
238 it meets the NEM, forming the Congo Air Boundary (CAB). Besides the AL, another important
239 circulation feature is the Mozambique Channel Trough (MCT), off the east coast of central Mozambique,
240 which is probably associated with warm sea surface temperatures in the Mozambique Channel. It
241 conducts most of the NEM from the eastern coast of SAF towards Madagascar and the Mozambique
242 Channel. The monsoonal flows NEM and NWM meet the SETW in the south, forming the SAF
243 Intertropical Convergence zone (ITCZ). The commonly accepted definition of ITCZ, which is the
244 location where the trades meet the northerly monsoonal flow, is used here. In SAF, the ITCZ influences
245 rainfall patterns particularly over the eastern portion of the subcontinent, comprising central Mozambique
246 (around 20°S), and Madagascar (Fig. 2a). Apart from northern Madagascar, where the strong rainfall
247 maximum may be influenced also by orography, the maximum summer rainfall is not coincident with the
248 ITCZ. This agrees with the view that the ITCZ may not explain the rainfall distribution over continental
249 Africa and its seasonal variations, although it can have important contribution. Other factors, such as the
250 role of topography in the development of rain-bearing systems, as well as thermodynamic and dynamic
251 conditions for ascent and rainfall, favoured by the climatological summer conditions, may be more
252 important than the low level convergence associated with the ITCZ (e.g., Nicholson 2018).

253   The convergence along the northern CAB may influence the precipitation maximum over central
254   SAF, although in this region the role of orography may also be determinant, since the regions of
255   interaction between the monsoonal flows with the mountains in southern Democratic Republic of Congo
256   (DRC) and in northeastern Zambia are co-located with rainfall maxima. The southern CAB does not
257   coincide with a maximum rainfall band.

258   The three airflows converging on SAF can be affected by the progression of pressure systems at
259   higher latitudes, and by tropical cyclones. Therefore, climate variability that affects these factors can
260   affect monsoon rainfall in SAF

261   The regional upper-level climatological circulation seems to be dominated by the Botswana High
262   (BH), a prominent mid-tropospheric regional circulation system (Driver and Reason 2017) (Fig. 2b),
263   consistent with a response to the enhanced monsoon convection (Fig. 2a).

264   Although the maximum rainfall band encompasses several countries in SAF, the variability
265   analysis will be centered on eastern SAF, in the region over Mozambique (where daily gauge data are
266   available), which is consistent with the region of maximum summer rainfall over central-east SAF shown
267   in McHugh and Rogers (2001, their Fig. 2a). Comparison with variability modes of OLR obtained on a
268   larger domain shows consistency with the variability at this region, which also shows connection with
269   variations in the monsoon circulation.

270

271   **4 Intraseasonal rainfall leading modes and their associated circulation anomalies**

272

273   *4.1 The leading modes and their prevailing periods*

274

275   The factor loadings of four rotated empirical orthogonal functions (REOF) of daily precipitation,
276   present in the three considered intraseasonal bands, are shown in Fig. 3, besides the factor scores of the
277   20–90 day band REOF3. The last of these modes (REOF5 in the 10–25 day band and REOF4 in the other
278   two bands) is slightly different in the 20–90 day band, while REOF1, REOF2 and REOF3 are very
279   similar in all intraseasonal frequency bands, even in non-filtered data (not shown), indicating that these
280   modes are present in all these time scales. Although in this analysis we use filtered daily data, it is
281   noticeable that the factor scores of the 20–90 day band REOF3 displayed in the last row of Fig. 3 capture
282   well the floods that occurred over central Mozambique during the 2000/2001 summer monsoon season,
283   demonstrating their robustness in adequately describing this important event present in the original data.
284   The variance explained by the rotated modes (shown on top of each REOF, Fig. 3) is calculated with
285   respect to the variability explained by the non-rotated modes retained.

286   The prevailing low-level anomalous circulation associated with each mode is shown in Fig. 4 through
287   maps of correlation coefficients between the factor scores of each 20–90 day band REOF and the
288   components of 850 hPa wind at each grid point over the SAF. Similar analysis giving similar results (not
289   shown) was performed for the other two bands (10–25 days and 10–90 days). This figure shows that
290   enhanced precipitation in all modes is associated with an anomalous cyclonic circulation centered around
291   different positions. It is evident that the anomalous precipitation and circulation related with REOF3 and
292   REOF4 appear to be more associated with variations in monsoon precipitation and circulation (enhanced

293 NWM, NEM, and even the SETW, besides the MCT), favourable for enhanced monsoon rainfall in the
294 core monsoon region. It is also worth mentioning that for the 30-60 day band (not shown, only focused on
295 MJO), the REOF3 mode changes to REOF1. Visual inspection of Figs. 1b, 2a, 3, shows that the monsoon
296 core region over SAF (particularly Mozambique) encompasses regions with strong factor loadings of
297 REOF3 and also REOF4, although REOF3 alone represents most of the variability in the box of the MPI.
298 The strong connection between REOF3 and MPI is also shown in section 5. Moreover, the region with
299 highest factor loadings of this mode at each intraseasonal frequency band seems also consistent with that
300 of the first summer mode on interannual time scales for Yim et al. (2014, their Fig. 3d), suggesting that
301 besides undergoing monsoon precipitation ISV, it also experiences significant variability at longer
302 timescales.

303 The PSD of REOF3 in the 10–90-day band (all the ISV), shown in Fig. 5, indicates that the strongest
304 signals in the intervals 10-20, 20-30, and 30-90 days have periods respectively around 12, 24, and 50
305 days. The first one is associated with the quasi-biweekly oscillation (QBW, Kikuchi and Wang 2009),
306 with wavelike features propagating into the SAF region from the extratropical westerly belt of the
307 Southern Hemisphere. The origin of the second one is still unclear, but it also appears in the South
308 American monsoon precipitation and seems to be linked to the Tropics (Nogués-Paegle et al. 2000). This
309 peak is also present in REOF1 and REOF2 (not shown). It is probably the variability mentioned by Levey
310 and Jury (1996) and Jury (1999), who reported that summer convection over southern Africa is "pulsed"
311 at cycles of 20–35 days, associated with the passage of wave trains in the subtropical westerly flow whose
312 influence spreads into the tropical belt over Africa. The third one is associated with MJO. All these three
313 time scales are also present in the South American ISV, especially in the South Atlantic Convergence
314 Zone (SACZ) (Nogués-Paegle et al. 2000; Kikuchi and Wang 2009; Grimm 2019). The MJO-related peak
315 is weaker in Fig. 5 compared with those in the interval of 20–30 days or 10–20 days, suggesting that the
316 latter ones likely contribute more significantly to rainfall ISV over SAF. The MJO contribution (temporal
317 band 30–60 day) is a little stronger for REOF4 (not shown) than for REOF3, which is expected, since the
318 former has stronger factor loadings nearer to the equator than the latter. It is weaker for REOF2 and
319 REOF3, whose strongest factor loadings are more to the south.

320 Although these ISV modes of observed precipitation in southeast SAF are not exactly comparable
321 with those obtained with different variables (e.g., OLR), domains (e.g., including the Indian Ocean), or
322 methods (e.g., using daily PCA for each summer separately, as in Jury (1999), PCA of daily OLR, as in
323 Pohl et al. (2009), or Canonical Correlation Analysis, as in Puaud et al. (2017), the last two for a domain
324 including the Indian Ocean), it is interesting to verify if those modes describe approximately the same
325 ISV of the monsoon precipitation in the SAF core monsoon region represented by our REOF3 and
326 REOF4.

327 Jury (1999) calculated ISV modes of pentad OLR over SAF for each summer in the period 1976–
328 1994. The results indicate that the cumulative % variance explained is largest for the tropical NE mode,
329 with largest loadings in the same region as REOF3, over northern Mozambique and Malawi (e.g., their
330 Fig. 3a), which is influenced by the line of confluence established by the cross-hemispheric NEM.

331 Puaud et al. (2017) reported covariability between SA and SAF with about 10–day lag in the ISV
332 band 25-75 days. As most of the highest frequency ISV is filtered out in this band (periods around 12 and

333 22-24 days), the frequencies at which the co-variability was analysed is strongly reminiscent of MJO.
334 Their canonical correlation analysis first co-variability mode in summer over SAF has largest components
335 in the NE part of SAF (their Fig. 5a), similar to the mode REOF3 (and REOF4) of the present study (Fig.
336 3). Since Puaud et al. (2017) filtered in the band 25–75, while here the band is 20-90 and the band 10–25
337 is the one with highest PSD in ISV (Fig. 5), their analysis retained mainly the MJO-related variability.
338 Therefore, a straight comparison is not possible, but it is worth pointing out that their intraseasonal mode
339 with co-variability with SA has spatial distribution similar to REOF3 (and REOF4), concentrating on NE
340 SAF.

341   Pohl et al. (2009) calculated modes of daily summer OLR variability. The factor loadings and the
342 associated vertical wind anomalies show that all the five first modes contribute to the rainfall variability
343 of the MPI region in northeast (NE) SAF, especially the first one. The two first modes are those that
344 represent most the synoptic variability associated with tropical–temperate troughs (TTT) that propagate
345 north-eastward, but they also contain ISV. In this time scale, they interact significantly at the period
346 around 12 days. The next three ones display more power in the intraseasonal time scales, both in the
347 higher frequency band (10–30 day) and the MJO band (30–70 day). They represent the propagation of the
348 large-scale convective clusters over SAF in intraseasonal time scales, and have common variance with the
349 first two modes and between themselves. Therefore, even if the first two modes do not seem strongly
350 modulated by MJO, they undergo its influence through association with the other modes in the
351 intraseasonal time scales. Therefore, the ISV with periods around 12, 24 days and the MJO band seem to
352 explain complementary parts of the subseasonal atmospheric and rainfall variability over SAF, which is
353 of importance for the subseasonal forecasting.

354

355 *4.2 The space-time evolution of rainfall and circulation anomalies related to 10–25 day mode 3*

356

357   Although most of the subseasonal predictability comes probably from ISV modes with longer periods,
358 it is interesting to see how the highest frequency ISV influences precipitation in NE SAF, and therefore,
359 MPI. As mentioned before, this frequency band, which displays a peak with period around 12 days (Fig.
360 5), is associated with the QBW oscillation (Kikuchi and Wang 2009).

361   Fig. 6 displays the difference between lead-lag composite anomalies keyed to positive and negative
362 phases of the 10–25 day band REOF3 for 200 hPa eddy streamfunction and OLR. Before calculating the
363 composites, anomalies are filtered to retain the 10–25 day band. Streamfunction is used because the
364 response of the rotational component of atmospheric circulation to the anomalous heat sources at lower
365 latitudes is more evident in this field rather than in geopotential height. The lower right panel of Fig. 6
366 shows an approximate scheme for the temporal evolution of the oscillation revealed in this composite.
367 The days are keyed to the first days of the positive phases (factor scores equal or above 0.7 standard
368 deviation), named − 0, and to the last days of the positive phases, named +0. The entire sequence of Fig. 6
369 represents 1.5 cycles of a 12-day oscillation. Between days − 6 and − 4 there is negative phase, with
370 below normal precipitation over NE SAF (and negative MPI over the small green rectangle). In day − 4
371 begins the transition from a negative phase to neutral conditions. At this time, OLR (rainfall) anomalies
372 are still positive (negative) over the MPI region. A wave train extends over the southern extratropical

373   Atlantic, with weak cyclonic anomalies east of the southern coast of SA. As negative OLR anomalies
374   develop over southeast SA, this cyclonic center strengthens, as well as the streamfunction centers
375   downstream. Over SAF, northwest-southeast bands of enhanced convection and subsidence extend to the
376   east of respectively the cyclonic and anticyclonic centers over the region and move northeastward. These
377   features represent tropical–temperate interactions and occurrences of synoptic scale TTT systems. They
378   are represented by the first two modes of daily OLR in Pohl et al. (2009), which concentrate most of the
379   variability in the 5-20 day band (synoptic and higher frequency ISV), and have strong interaction or
380   common variance for periods around 12 days. As the wave train moves eastward, at day − 0 the
381   anomalous convection is centered over the MPI region, from where it moves eastward at day +0, and
382   vanishes at day +2, when opposite anomalies start. An entire cycle takes place, for example, between days
383   -4 and +6, with opposite phases of precipitation over NE SAF (or of MPI) on days − 0 to +0 and +4 to +6.

384   Convective activity associated with the QBW is significant in the subtropical regions along 10°–30°
385   latitudinal bands in both hemispheres, and are connected with upstream extratropical Rossby wave trains
386   propagating primarily eastward and equatorward. The positive (negative) convective anomalies caused by
387   those circulation anomalies are associated with low-level northerly (southerly) wind anomalies in the
388   Southern Hemisphere. Barotropic Rossby wave trains (with slight westward tilt with height below 700
389   hPa when entering subtropics) are essential in controlling initiation, development, and propagation of the
390   eastward QBW mode in the subtropics, as well as in maintaining QBW convection in some regions
391   (Kikuchi and Wang 2009). Besides being triggered by extratropical Rossby wave trains, the QBW
392   subtropical convective activity can also produce or influence the extratropical Rossby wave that is
393   responsible for eastward propagating the convective anomaly. In the Southern Hemisphere during the
394   austral summer it can happen, for example, with anomalous convection in the central-eastern subtropical
395   South Pacific and over SA, where anomalous convection can influence the extratropical Rossby wave that
396   will produce convection respectively in SA (SACZ and subtropical plains to the southwest) and in SAF.
397   Indications about this influence are visible in Fig. 6 (see, for instance, days − 0 and +4), as well as in
398   maps of QBW teleconnectivity and austral summer QBW life cycle over SA and SAF (Kikuchi and Wang
399   2009).

400

401   *4.3 The space-time evolution of rainfall and circulation anomalies related to 20–90 day mode 3*

402

403   The PSD analysis of REOF3 in the 20-90 day band shows the highest significant peaks with periods
404   around 22-24 days and 50 days (Fig. 5). Figures 7 and 8 display the difference between lead-lag
405   composite anomalies keyed to positive and negative phases of this mode for 850 and 200 hPa eddy
406   streamfunction, CPC rainfall and OLR. Before calculating the composites, anomalies are filtered to retain
407   the 20–90 day band, and this can account for weaker anomalies than displayed by other studies.

408   Since the PSD peak for period around 24 days is much higher than that for 50 days (MJO time scale),
409   that shorter period will be more reflected in the composite, contrary to Puaud et al. (2017), in which the
410   period around 24 days was filtered out before the analysis, this emphasizing the MJO-related period
411   around 50 days (they used the 25-75 day intraseasonal band). In the present composite this MJO period is
412   superimposed on the approximate 24-day period, modulating it, but is less clearly visible than the 24-day

413 period. The lower right panel of Figs. 7 and 8 shows an approximate scheme for the temporal evolution of
414 the anomaly composite oscillation, with the days keyed to the first days of the positive phases (− 0), and
415 to the last days of the positive phases (+0). Although the figures were produced from day − 16 through
416 +16 in order to construct this scheme, the composite is displayed only from day − 8 (8 days before -0) to
417 day +8 (8 days after +0), covering an interval of around 20 days. This corresponds to a little more than
418 three MJO phases of around 6 days each (Wheeler and Hendon 2004). When the effects of the two
419 variabilities are in phase the anomalies have highest intensity.

420　　While Fig. 7 shows anomalies of 850 hPa circulation and continental CPC precipitation, Fig. 8
421 displays anomalies for 200 hPa and OLR. Day − 8 represents the beginning of the transition from a
422 negative phase to neutral conditions (see scheme). At this time, rainfall (OLR) anomalies are still negative
423 (positive) over the PMI region in NE SAF, and positive (negative) over central-east Brazil, especially the
424 southern part of it, over the SACZ (Figs. 7a, 8a). These anomalies are probably connected with a wave-
425 train from the enhanced convection on the subtropical South Pacific, east of the Date Line, towards SA,
426 which can influence rainfall over SA (Grimm 2019) through a Pacific-SA (PSA)-like pattern comprising
427 an upper-level anticyclone in the extratropics and a cyclone in the subtropics of SA (Mo and Nogués-
428 Paegle 2001) (Fig. 8a). Over the southeastern Pacific Ocean and SA there are signals of this Rossby
429 wavetrain connecting the anomalous convection over the subtropical South Pacific (visible in Fig. 8a) to
430 the enhanced SACZ convection, as described in Grimm (2019) in connection with the MJO impacts, and
431 visible in the composites of day − 8 (Figs. 7 and 8). Since convective anomalies in the Pacific Ocean and
432 its associated anomalies over SA can exist in both time scales, around 22-24 days and in the MJO time
433 frame (Nogués-Paegle et al. 2000), the connection between the Pacific Ocean and SA may happen in both
434 time scales of the ISV, as well as the connection from SA to SAF described in Grimm and Reason (2015).

435　　The extratropical circulation anomalies some days before day − 0 are favourable to the formation of
436 TTTs over SAF (Grimm and Reason 2015). This is confirmed by the OLR anomalies from day − 8 to day
437 − 0, which show the familiar southwest-northeast oriented dipole pattern of significantly enhanced and
438 suppressed rainfall (convection) over SAF (Washington and Todd 1999) moving northeastward before
439 day -0 (Figs. 7a-e, 8a-e). During this period, convection increases over Central-East SA and western
440 tropical South Atlantic and decreases over the subtropics. The anomalous convection over SA is able to
441 influence the tropical and extratropical circulation over the Atlantic, producing an anticyclone over the
442 extratropical South Atlantic and a cyclone south of Africa by day − 0, both of barotropic structure (Figs.
443 7d,e, 8d,e). The circulation anomalies averaged just before and over days of positive phase (between days
444 − 4 and 0) show clearly an extratropical Rossby wave train from SA towards SAF, favouring rainfall in
445 the target region by the subtropical combination cyclone-anticyclone at upper-level (and cyclone at low-
446 level) over SAF and by also producing low-level convergence and upper-level divergence via the tropical
447 circulation in the tropical teleconnection between SA and SAF (Figs. 7f, 8f). At low levels (Fig. 7), the
448 circulation anomalies at days − 0 and 0 enhance the monsoon-related circulation, such as the NWM, the
449 NEM, as well as the SIH (Fig. 2a). When the 10-20, 20-30 and 30-90 day variability bands are in phase at
450 day 0 (between − 0 and +0), the lower frequency anomalies favour the enhancement and persistency of
451 the higher frequency anomalies associated with enhanced rainfall in NE SAF (cf. Figs. 6 and 8).

452　　It is worth mentioning that the composite corresponding to day -0 presents the same circulation

anomalies as the corresponding composite in Puaud et al. (2017) for similar OLR anomalies over SAF (their Fig. 7, Day D+15). A wave train similar to that in our Fig. 8d-e also emerges from SA, with an anticyclone over the extratropical South Atlantic and a cyclonic anomaly southwest of the enhanced convection over NE SAF. The other days are not very comparable, since their composites do not contain the 24-day oscillation, although their composite for D+20 reminds our Fig 8f (days 0 All). Our composite for day − 2 is also comparable with the corresponding composite in Nogués-Paegle et al. (2000, their Fig. 2c), for the maximum convection over Central-East SA.

The tropical convection during the neutral conditions between a negative and a positive phase (days − 8 through − 0, Figs. 8a-e) is enhanced in Central-East SA (negative OLR anomalies) and with less intensity extends from Northeast Brazil towards tropical Africa over the equatorial Atlantic, as is typical for MJO phase 1 (Grimm 2019). During the days of positive phase (day − 0 through 0+) the convection over SA withdraws to Northeast Brazil and weakens, while over Africa it shifts to the subtropics of NE SAF, which is typical of MJO phase 2 and 3 (Grimm 2019).

In the last day of REOF3 positive phase (day 0+, Fig. 8g) the pattern of enhanced precipitation moves a little north-eastward and a band of suppressed convection appears southwest of it. In the next two and four days (+2, +4) these two bands forming a southwest-northeast oriented dipole pattern of significantly suppressed and enhanced rainfall (convection) over SAF continue to move north-eastward and the REOF3 pattern will enter its negative phase in day +8 (Fig. 8k). The changes associated with the beginning of opposite phases can be seen by comparing composites for day − 0 (beginning of a positive phase) and day +8 (beginning of a negative phase), which are separated by 12 days or approximately half period of the oscillation (see scheme). Therefore, it is expected that the anomalies are approximately of opposite signs. In fact, comparing Fig. 8e with 8k it is possible to see that the OLR anomalies changed from negative to positive over Northeast Brazil and the MPI region, while over the Maritime Continent they changed from positive to negative, and the same change happened to the predominant OLR anomaly in the subtropical South Pacific, east of the Date Line. The streamfunction patterns also change sign.

The changes associated with the end of opposite phases can be seen by comparing composites for day − 8 (end of a negative phase) and day +0 (end of a positive phase), which are also separated by 12 days or half period, and also display patterns of opposite signs (Figs. 8a and 8g). As this same interval separates day − 0 (beginning of a positive phase) and day +8 (beginning of a negative phase), with composites from day − 16 though day +16, it was possible to determine the dominant period of 24 days for REOF3 in the band 20-90 day.

It is worth mentioning that the enhanced convection associated with this mode comprises the entire core monsoon region with maximum summer rainfall in SAF (cf. Figs. 8f and 2a). Therefore, a rainfall index based on a region with highest factor loadings of this mode would represent well the ISV of the SAF monsoon.

Although the analysis in Figs. 7 and 8 indicates that convection anomalies prevalent in these composites are in the 20–30 band variability, the anomalies observed during few days before the first day of the positive phase of REOF3 resemble the MJO phase 1, consistent with Fig. 3 in Grimm (2019). This suggests that the existing teleconnection between SA and SAF may happen via tropics–tropics and tropics-extratropics, in the 20–30 day band and in the MJO time frame (Grimm and Reason 2015; Grimm

2019), with the related convection anomalies over tropical SA / Atlantic Ocean playing an important role in modulating eastward propagating anomalies. These anomalies over SA exist in both time scales (Nogués-Paegle et al. 2000), as they also exist in the subtropical South Pacific, east of the Date Line, where they seem to be connected with production of convective anomalies over SA (Grimm 2019). An anomaly composite similar to that in Fig. 8, but using anomalies filtered in the 30–90 day band (not shown), confirms that there is also variability within the 30–60 day band, and that precursor anomalies are consistent with the MJO phase 1.

The composite anomalies for REOF4 (not shown) also indicate the role of convective anomalies associate with MJO phase 1, but emphasizes a tropics-tropics teleconnection between SA and SAF, while for REOF3 teleconnection between SA and SAF may happen via tropics–tropics and tropics-extratropics in the SH.

Convection variability on intraseasonal time scales in the 20–90 day band over NE SAF (the region under focus) results from a complex interaction of time as well as spatial scales. In addition to the MJO, there is a sub monthly mode with highest peaks around 22–24 days, as in SA (Nogués-Paegle et al. 2000). According to Nogués-Paegle et al. (2000) both modes are linked to the tropics. In their study of the SACZ variability, they found that the two modes reinforce each other over SA to enhance or suppress the SACZ. Over SA, these two modes are in phase with each other, but they tend to cancel out over certain regions of the Pacific Ocean. Therefore, the MJO signal does not appear clearly in the composites, as it also does not appear in the composites of Nogués-Paegle et al. (2000) when considering both modes included in the data.

Figures 7 and 8 indicate that teleconnections exist between the South Pacific and SA and this continent and SAF, through the tropics and via extratropical Rossby wave trains, generated by anomalous convection over SA and the neighbouring Atlantic (Grimm and Reason 2015). Indeed, an area of enhanced convection, for instance, over central-east Brazil is evident before the positive phase which likely modulates a tropics-tropics teleconnection towards SAF. The propagating extratropical teleconnection, which influences the extratropical wave trains with its migratory cyclones circling the globe, is probably originated from anomalous convection over SACZ. The wave train excited from SA interacts with SAF regional circulation, creating favourable conditions to enhance the monsoon circulation. For instance, in Fig. 7e, at the beginning of the REOF3 positive phase, the low-level westerly and northerly flows are strengthened over NR SAF. This circulation structure is responsible for enhanced convective activity over the monsoon region of SAF. At higher levels, the enhanced convection over SAF produces anticyclonic anomalies which reinforce the climatological Botswana High (Figs 8f and 2b).

5 Monsoon indices for southern Africa

5.1 Monsoon precipitation index (MPI)

The proposed MPI is intended to help characterizing, predicting and monitoring active and break monsoon spells, in the SAF monsoon domain predominantly over land, where this knowledge is of great importance for the regional economies and livelihood of millions of people. It is constructed based on the

understanding gained from the climatology (section 3) and the ISV leading modes (section 4). It is the average standardized precipitation anomaly (obtained from gauge data) in a region that satisfies two criteria: i) its rainfall variability represents fairly well the variability over the region of strongest monsoon rainfall over land (the northwest-southeast band over SAF and Madagascar in Fig. 2a), and ii) exhibits strong ISV. This region (20°S–13.75°S; 32°E–38°E) is approximately at the geographical centre of the highest monsoon rainfall band, which also comprises the South Indian Convergence Zone (SICZ).

Figure 9a, which represents the correlation of MPI with daily rainfall over land, shows that this index satisfies the first criterion, representing the variability of the northwest-southeast band of maximum monsoon rainfall extending from SAF to Madagascar (Fig. 2a), since the region of maximum correlation reproduces this rainfall band (cf. Figs. 2a and 9a). Another correlation map using the CPC Merged Analysis of pentad Precipitation (CMAP; Xie and Arkin 1997) data interpolated to daily resolution (not shown) extends the highest correlation band also over the ocean, between Mozambique and Madagascar. This result implies that the proposed index is suitable to measure the monsoon rainfall variability over SAF, including Mozambique and neighbouring regions most affected by the monsoon. Figure 9a also shows that there is correspondence between gauge and CPC precipitation, confirmed by the correlation coefficient between the MPI calculated with each of these data sets, which is 0.57 and statistically significant at 99 % confidence level. This suggests that CPC rainfall can be used as a proxy to observed gauge data, albeit with caution.

To ensure that the second criterion is met, meaning that MPI variability reflects the ISV leading modes more associated with the SAF monsoon over land, correlation between the MPI and the REOFs factor scores was calculated and informed in Fig. 3, in the lower right corner of the panels. Since the modes are obtained from filtered data, the index was also submitted to Duchon's filter to retain ISV in the corresponding bands of the modes, although for predicting and monitoring purposes it is advisable using unfiltered indices (Marshall and Hendon 2015). It is evident that the MPI has strongest correlations with mode 3, although it also significantly correlates with mode 4. As the circulation anomalies associated with these modes (Figs. 4c,d) reflect the variability of the monsoon circulation (NWM, NEM, SETW), it is expected that this index adequately depicts the variations of the core monsoon precipitation over continental SAF (and Madagascar) and reflects the rainfall ISV most directly associated with the variability of the monsoon circulation that affects this region (Fig. 2).

As already mentioned in section 4.1, besides representing well the ISV of the monsoon precipitation, which is important for subseasonal prediction, MPI also represents well the synoptic and interannual variability since, within the region of largest monsoon-related precipitation, the MPI area in NE SAF contains the highest factor loadings of the first modes in each of these time scales, as has been shown by other authors as well (e.g., Jury 1999; Pohl et al. 2009; Yim et al. 2014; Puaud et al. 2017) and the strongest negative OLR anomalies associated with the synoptic convective regime that most affects the monsoon region in SAF (Pohl et al. 2018).

5.2 Monsoon circulation indices

Since circulation is better simulated than precipitation by models, it is also convenient to define one or

573 more circulation indices related with the precipitation index. To this end, the MPI is correlated with 850

574 hPa zonal (Fig. 9b) and meridional (Fig. 9c) wind over SAF. Figure 9b indicates two zonally elongated

575 regions for definition of area-averaged monsoon circulation indices: one to the north of the MPI region

576 (gray box) and another to its south (pink box), henceforth referred to as zonal westerly and zonal easterly

577 wind indices (ZWWI and ZEWI, respectively). Visual inspection suggests that these indices are part of

578 the cyclonic circulation displayed in Figs. 4c, d. On the other hand, Figure 9c indicates regions for

579 definition of meridional wind indices: the meridional northerly wind index to the northeast of the MPI

580 region (MNWI, in the pink box), and the meridional southerly wind indexes 1 and 2, to the

581 west/southwest of this region (MSWI1 and MSWI2, in the dark blue and light blue boxes, respectively).

582 All these indices are consistent with variations in the monsoon circulation of Fig. 2a and with the

583 anomalies in Figs. 4c, d.

584   This analysis of the correlation between MPI and the zonal and meridional wind indices confirms that

585 the enhanced precipitation in the MPI region is indeed associated with a low-level cyclonic circulation

586 anomaly near this region (as can be seen in Figs. 4c, d). Therefore, it is possible to combine indices based

587 on just one element (zonal or meridional wind averaged over selected region) into indices containing

588 more than one element, which represent better this cyclonic anomaly and therefore follow more closely

589 MPI. Many possible combinations have been carried out with 2 to 4 elements (Table 1). One of the

590 simplest combination (with just two elements) is the zonal wind vorticity index (ZWVI), defined as the

591 difference between ZWWI and ZEWI, following a procedure used in Yim et al. (2014).

592   The combined indices usually present higher correlation with the MPI than those indices of which

593 they are formed, but there are interesting exceptions, generally involving the use of the ZWWI or ZEWI,

594 which alone present respectively the lowest and the highest correlation of one-element index with MPMI

595 (0.153 and -0.297, Table 1). For instance, the zonal and meridional wind vorticity indexes (ZWVI and

596 MWVI1 or 2), each composed by two elements, present similar correlation with MPI (0.315 and 0.317,

597 Table 1). Combining these indices gives a vorticity index with four elements (ZMVort1 or 2) whose

598 correlation with MPI is higher (0.372 or 0.376, Table 1). However, when combining MWVI1 or 2 with

599 just the ZEWI, creating a three-element index (MV1ZE or MV2ZE), the correlation increases to 0.392,

600 while the combination with just the ZWWI (creating MV1ZW or MV2ZW) decreases the correlation to

601 0.291 or 0.298. Another example of strong difference when using the ZWWI to the north or the ZEWI to

602 the south appears when combining two elements in one index. The combined index with two elements

603 that shows highest correlation with MPI joins ZEWI with MNWI, forming ZEMN, which presents a

604 correlation coefficient of -0.381 with MPI, while joining ZWWI with MNWI, forming ZWMN, gives a

605 correlation of only 0.205 (Table 1). The highest correlation is obtained with an index of averaged

606 vorticity over a region in eastern SAF.

607   Looking at Figs. 4c, d, it seems that the zonal westerly wind index to the north would have more

608 connection with MPI (which is related to REOF3 and REOF4) than the zonal easterly wind index to the

609 south. However, it is important to remember that Fig. 4 shows correlation between modes of precipitation

610 variability and 850 hPa wind in the 20-90 day band. In this time scale, the westerly zonal wind near the

611 equator is more important for the rainfall variability in REOF3 (and MPI). On the other hand, the

612 circulation indices and MPI were not filtered to calculate the correlations in Table 1, and thus they

613 contain all the synoptic variability produced by the passage of the extratropical patterns of atmospheric
614 circulation that travel around the globe and penetrate southern Africa, influencing much more the
615 subtropical rather than the equatorial circulation. Therefore, this synoptic component, which is stronger in
616 ZEWI than in ZWWI tends to strengthen the correlation of MPI with indices containing ZEWI rather than
617 ZWWI, when MPI and the circulation indices are not filtered. For weather prediction this synoptic
618 component is important and this is why in Table 1 it is not removed. However, in subseasonal prediction,
619 when using weekly averages, the subseasonal component of the variability becomes more important.
620
5.3 Relationship between the monsoon circulation indices and monsoon rainfall variability
622
623   While Figure 9a shows how the MPI represents the variability of the monsoon rainfall over land in
624 SAF and Madagascar, Fig. 10 shows the results of the correlation between some of the monsoon
625 circulation indices and CPC daily precipitation, to show how they represent the monsoon rainfall
626 variability over SAF. Similar analysis was performed using gauge data, and gave qualitatively similar
627 results over where gauge data available. The correlation maps are shown for indices: i) based on one
628 element, in order to show the relationship with isolated components of the circulation (Figs. 10a-d)
629 (except for MSWI2, for which the correlation patterns are similar to MSWI1, but a little more limited to
630 the eastern part of SAF); ii) based on two elements, which represent vorticity based on zonal wind and on
631 meridional wind (ZWVI and MWVI1, Figs. 10e-f), besides the combination of two elements which
632 presents the higher correlation with MPI (ZEMN, Fig. 10g); iii) based on three elements with ZWVI
633 combined with each meridional wind index (ZVMN and ZVMS1, Figs. 10h-i), besides the combination
634 of three elements which presents the highest correlation with MPI (MV1ZE, Fig. 10j); iv) based on four
635 elements (ZMVORT1, Fig. 10k), and v) of averaged vorticity over a selected region (VORT, Fig. 10l).
636   The correlation maps in Fig. 10 are compared with that one in Fig. 9a. Figures 10a-b show that
637 enhanced monsoon rainfall over SAF (and not just MPI) is associated with westerly and easterly wind
638 anomalies averaged over the boxes of Fig. 9b, which is consistent with enhancement of the climatological
639 monsoon circulation of Fig. 2a. Both correlation maps indicate significant values over the MPI region and
640 neighbouring regions with monsoon rainfall, as in Fig. 9a. However, the ZWWI shows also influence on
641 the rainfall in the equatorial part of SAF (Fig. 10a), while the ZEWI is also correlated with rainfall over
642 the region in western SAF (Fig. 10b). The meridional northerly wind index MNWI also displays a pattern
643 of significant correlation similar to Fig. 9a, with the exception of minor features in southeastern and
644 western SAF (Fig. 10c). The correlation of southerly wind index MSWI1 with rainfall (Figs. 10d),
645 although showing high values in the region of MPI, also presents significant values over extensive region
646 in southern SAF and a little to northeast of the main monsoon rainfall band (correlation with MSWI2, not
647 shown, is similar, but significant positive correlation in the northern SAF is a little more limited to the
648 eastern part of SAF). These results show that indices that represent circulation features more to the
649 subtropics and that are more affected by extratropical variability, such as ZEWI and MSWI1 and 2,
650 although influencing the monsoon rainfall variability, also influence rainfall in non-monsoonal regions,
651 such as southern and western SAF.
652   The adequate combination of these one-element indices into two-element indices, in order to more

653 accurately represent the vorticity anomaly associated with the precipitation anomaly, generally improves
654 their correlation with MPI, and their correlation patterns with rainfall become more similar to the
655 distribution of higher monsoon rainfall (and to Fig. 9a). This happens, for instance, with ZWVI and
656 MWVI1 (Figs. 10e-f) and ZEMN (Fig. 10g). It is convenient to point out that, although the correlation of
657 MPI with ZEWI is higher than with ZWWI, the correlation with the vorticity index combining them
658 (ZWVI) is even stronger than for each one of them (Table 1). This emphasizes the importance of the
659 cyclonic circulation to the west of the precipitation index region for the enhancement of the monsoon
660 rainfall (Fig. 4c). As mentioned in the previous section, the variability of the zonal westerly wind
661 (ZWWI) is important in intraseasonal time scales (clear in Fig. 4c), although it is lower than the synoptic
662 variability of the zonal easterly wind index to the south (ZEWI), but the combination of the two gives a
663 much better representation of the vorticity anomaly that produces enhanced rainfall.

664 Combination to produce three elements indices further improves their representation of the vorticity
665 anomaly and their correlation with MPI and the relationship with variability of the highest monsoon
666 precipitation, as exemplified by two indices based on the zonal wind vorticity combined with a
667 meridional wind index, ZVMN (Fig. 10h) and ZVMS1 (Fig. 10i), and by one meridional vorticity index
668 combined with ZEWI, (MV1ZE, Fig. 10j). When adding to a three-element index the ZWWI as fourth
669 element (creating ZMVort1 or 2) the correlation with MPI does not improve (Table 1), but the
670 relationship with monsoon rainfall is improved (Fig. 10k). The index VORT, the average of vorticity in a
671 region covering MPI, but with its center a little displaced to southwest of MPI's center (Fig. 9c), displays
672 the best correlation with MPI.

673 The results in Table 1 and Fig. 10 demonstrate that the enhanced (supressed) rainfall over the
674 monsoon core region (represented by positive (negative) MPI) is accompanied by westerly (easterly)
675 wind anomalies in the region marked ZWWI (ZEWI) in Fig. 9b, as well as northerly (southerly) wind
676 anomalies in the region marked MNWI (MSWI1 or MSWI2) in Fig. 9c, suggesting the potential of these
677 indices for prediction of active monsoon spells over the region (opposite anomalies would indicate break
678 monsoon spells). These wind components are climatologically associated with the monsoon circulation
679 (Fig. 2a) and their strengthening (weakening) would be expected to strengthen (weaken) monsoon
680 precipitation. The combination of these indices to more completely reproduce the cyclonic anomaly
681 associated with enhanced rainfall in the MPI region and surroundings improves the relationship of the
682 resulting circulation index with the rainfall index or with the highest monsoon precipitation variability.

683 The more subtropical indices, such as ZEWI and MSWI1 and 2 are more affected by the synoptic
684 variability, whereas the ISV is more present in the more tropical indices, such as ZWWI and MNWI, as
685 can be seen in the correlation of filtered anomalies with the ISV modes in Figs 4c, d.

686 The monsoon circulation indices and their correlation with the precipitation (Fig. 9) give an idea of
687 how the variation of the different monsoon-related flows in Fig. 2a contributes to the variation of the
688 monsoon precipitation. Their intensification increases the monsoon precipitation, including the
689 intensification of NEM (represented by the index MNWI) and SETW (represented by the index MSWI1
690 or MSWI2), although Nicholson (1996) stated that the NEM and the SETW are thermal stable flows and,
691 hence, associated with subsiding air or dry conditions. However, according to Torrance (1972), the NEM
692 flow is dry when it originates over the eastern Sahara, and does not traverse the northwestern Indian

693 Ocean. This could be expanded to say that the SETW are dry, when they do not traverse the warm and
694 moist southern Mozambique Channel.

695   Figure 11 shows further comparison between rainfall as defined by MPI calculated with gauge data
696 (solid black line) and CPC data (dotted black line) for two summers with strong rainfall anomalies in SAF
697 (1996-1997 and 1999-2000), besides two circulation indices: MV1ZE and VORT, which display the best
698 correlation with MPI (Table 1). The figure shows that gauge MPI and CPC MPI exhibit frequent
699 discrepancies, although the main variations are coherent. However, the highest gauge MPI values (around
700 4 standard deviations) were underrepresented by the CPC MPI, while some modest gauge MPI values
701 were very exaggerated by the CPC MPI (as in December 1996). The circulation index MV1ZE based on
702 three elements, two of them more subtropical (MSWI1 and ZEWI), and one more tropical (MNWI),
703 presents a much higher variability than MPI, perhaps due to its higher synoptic variability, while the
704 variability of VORT is comparable to that of MPI. The ZVMN, based on three elements predominantly
705 tropical (not shown), exhibits less variability than MV1ZE.

706   Some of the monsoon circulation indices are compared with the vorticity circulation index of Yim et
707 al. (2014), calculated considering a SAF monsoon domain very extended over the Indian Ocean, east of
708 Madagascar, with more than half its area over the ocean. The correlation of their index with ZWWI,
709 ZEWI, ZWVI, and ZVMN is, respectively, 0.66, -0.44, 0.75, and 0.57, significant at 99% confidence
710 level. It is not significantly correlated with MNWI, which is somehow expected, since the Yim et al's
711 index is based solely on U850 index, over two regions much more longitudinally elongated than the ones
712 used here, extending up to 50°E over the Indian Ocean. On the other hand, its strong correlation with
713 ZWVI demonstrates that the latter may adequately be used for a domain more extended over the ocean. It
714 is not possible to compare the monsoon precipitation index used here with that of Yim et al's, since the
715 INAM (and CPC) data do not cover oceanic regions, included in their rainfall index. Notwithstanding,
716 there is probably a correspondence, although their index does not represent variability of the monsoon
717 rainfall in the central-eastern tropical continental SAF, since their index reference region is displaced
718 eastward, extending much over the ocean.
719

720 **6 Summary and Conclusions**
721

722   Regional climate in SAF varies over a range of timescale. In this study the emphasis is placed on ISV
723 affecting the monsoon region, which is of great importance for agricultural production, water resources
724 management, and subseasonal prediction. Notwithstanding the contribution of synoptic variability is also
725 taken into account. The space-time structures of intraseasonal summer rainfall leading modes of
726 variability over SAF are determined based on rainfall gauge data in eastern SAF. The study reveals four
727 dominant patterns of ISV. Among these modes, the third one (REOF3) displays strongest factor loadings
728 over the region with most intense monsoon precipitation and is associated with variations in the monsoon
729 circulation. Furthermore, the spatial pattern of this mode resembles that obtained by Yim et al. (2014) as
730 the leading interannual variability mode of summer precipitation over a SAF monsoon domain that
731 extends over the Indian Ocean. A similar mode in this region appears in previous studies on OLR ISV
732 over a larger domain in SAF including part of the Indian Ocean. Since there is not a perfect

733 correspondence between OLR and gauge data, it is important to make such comparison.

734   In the intraseasonal 10–90 day band this mode displays the strongest oscillations at periods around 12,

735 22-24 and 50 days. The 12-day oscillation is associated with the QBW oscillation (Kikuchi and Wang

736 2009) produced by Rossby wave trains propagating into the SAF region from the extratropical westerly

737 belt of the Southern Hemisphere. The 22-24 day oscillation is consistent with the one found by Nogués-

738 Paegle et al. (2000) for the ISV in central-east SA and SACZ, probably linked to tropical convection

739 variability. The 50 day oscillation is associated with the MJO. The lead-lag composite difference between

740 positive and negative phases of this mode in the 20-90 day band, for convection and circulation

741 anomalies, confirms that a 24 day variability mode and the MJO influence are associated with these

742 oscillations. Besides, the temporal lags indicate the influence of convective anomalies over SA and

743 propagation of atmospheric waves (tropical and extratropical) from SA to SAF. This lower frequency ISV

744 displays larger spatial scale (lower wave number) than the 12-day oscillation. These teleconnections

745 create favourable conditions for enhanced convective activity for few days over SAF, and consequently

746 more rainfall in the monsoon region. Indeed, the convection anomalies observed over SA and SAF few

747 days before the beginning of the REOF3 positive phases are reminiscent of the composites by Nogués-

748 Paegle et al. (2000) and of MJO related OLR anomalies in the phase 8 and 1, as shown in Grimm (2019).

749 They are also coherent with the intraseasonal summer teleconnection between SA and SAF shown in

750 Grimm and Reason (2015).

751   A monsoon MPI is proposed, on the basis of the monsoon climatology and variability, to represent the

752 variability of SAF monsoon and facilitate the evaluation of climate models' performance in reproducing

753 this variability. This index is intended to help characterizing, monitoring and predicting active and break

754 monsoon spells in the SAF monsoon domain predominantly over land using models participating in the

755 S2S Project. It is based on the average standardized precipitation anomaly over a selected area in NE

756 SAF, where the variability of the precipitation in the core monsoon region over land is strongest not only

757 on intraseasonal but also on synoptic and interannual time scales. Accordingly, the MPI reflects

758 adequately the variability of the monsoon precipitation over the region where this precipitation is

759 strongest over SAF, since the map of strongest correlations of the unfiltered MPI based on daily gauge

760 data with the unfiltered daily CPC rainfall data over the entire SAF reproduces well the SAF core

761 monsoon region.

762   Besides the precipitation index (MPI), also monsoon circulation indices are defined based on

763 circulation features most associated with the precipitation index. These indices may be useful for

764 subseasonal prediction, since they can be associated with rainfall and the models show better skill in

765 predicting circulation than precipitation. They represent components of the monsoonal circulation and

766 their variation is connected to the variation of the monsoon precipitation. They are based on one

767 circulation element (zonal or meridional wind averaged over selected region) or a combination of 2 to 4

768 elements. The highest correlation with MPI is obtained for an index of averaged vorticity over a region in

769 eastern SAF.

770   While the synoptic and higher frequency ISV is best represented by the subtropical circulation indices,

771 the tropical indices are important in the 20–90 day band. Combinations of both types produce indices with

772 higher correlation with MPI. Indices that represent circulation features more to the subtropics and that are

more affected by extratropical variability, such as ZEWI and MSWI1 and MSWI2, although influencing the monsoon rainfall variability, also influence rainfall in non-monsoonal regions, such as southern and western SAF. Therefore, indices that adequately combine other tropical and subtropical indices, in order to more accurately represent the vorticity anomaly associated with the precipitation anomaly, generally exhibit higher correlation with MPI, and their correlation patterns with rainfall are more similar to the distribution of the highest monsoon rainfall.

Acknowledgements

References

Chen M, Shi W, Xie P, et al (2008) Assessing objective techniques for gauge-based analyses of global daily precipitation. J Geophys Res 113:D04110. doi: 10.1029/2007JD009132

Driver P, Reason CJC (2017) Variability in the Botswana High and its relationships with rainfall and temperature characteristics over southern Africa. Int J Climatol 37:570–581. doi: 10.1002/joc.5022

Duchon CE (1979) Lanczos Filtering in One and Two Dimensions. J Appl Meteorol 18:1016–1022. doi: 10.1175/1520-0450(1979)018<1016:LFIOAT>2.0.CO;2

Dyson LL, van Heerden J (2001) The heavy rainfall and floods over the northeastern interior of South Africa during February 2000. S Afr J Sci 97:80–86

Grimm AM (2019) Madden–Julian Oscillation impacts on South American summer monsoon season: precipitation anomalies, extreme events, teleconnections, and role in the MJO cycle. Clim Dyn 1–26. doi: 10.1007/s00382-019-04622-6

Grimm AM, Reason CJC (2015) Intraseasonal Teleconnections between South America and South Africa. J Clim 28:9489–9497. doi: 10.1175/JCLI-D-15-0116.1

Grimm AM, Saboia JPJ (2015) Interdecadal Variability of the South American Precipitation in the Monsoon Season. J Clim 28:755–775. doi: 10.1175/JCLI-D-14-00046.1

Harrison MSJ (1984) A generalized classification of South African summer rain-bearing synoptic systems. J Climatol 4:547–560. doi: 10.1002/joc.3370040510

INAM (2019) Informação Sobre a Situação Meteorológica Nacional. In: Inst. Nac. Meteorol. https://www.facebook.com/meteo.maputo/. Accessed 26 Apr 2019

INGC (2019) Ponto de Situação: Ciclone IDAI (Dados preliminares até 12 de Abril de 2019). In: Inst. Nac. Gestão Calamidades. https://www.facebook.com/INGC.Mocambique/photos/a.30457988687 0732/328819124446808/?type=3&theater. Accessed 20 Apr 2019

Jolliffe IT (2002) Principal Component Analysis, Second Edition. Springer-Verlag, New York

Jury MR (1999) Intra-Seasonal Convective Variability over Southern Africa: Principal Component Analysis of Pentad Outgoing-longwave Radiation Departures 1976-1994. Theor Appl Climatol 62:133–146. doi: 10.1007/s007040050079

Kaiser HF (1958) The varimax criterion for analytic rotation in factor analysis. Psychometrika 23:187–200. doi: 10.1007/BF02289233

Kalnay E, Kanamitsu M, Kistler R, et al (1996) The NCEP/NCAR 40-Year Reanalysis Project. Bull Am Meteorol Soc 77:437–471. doi: 10.1175/1520-0477(1996)077<0437:TNYRP>2.0.CO;2

Kikuchi K, Wang B (2009) Global Perspective of the Quasi-Biweekly Oscillation. J Clim 22:1340–1359. doi: 10.1175/2008JCLI2368.1

824 Levey KM, Jury MR (1996) Composite Intraseasonal Oscillations of Convection over Southern Africa. J
825   Clim 9:1910–1920. doi: 10.1175/1520-0442(1996)009<1910:CIOOCO>2.0.CO;2
826 Liebmann B, Smith CA (1996) Description of a Complete (Interpolated) Outgoing Longwave Radiation
827   Dataset. Bull. Am. Meteorol. Soc. 77:1275–1277
828 Macambaco MP (2016) Climate variations in southeastern Africa (SEA) and their possible
829   teleconnections with South America (SA). Master Thesis at Federal University of Parana
830 Macron C, Richard Y, Garot T, et al (2016) Intraseasonal Rainfall Variability over Madagascar. Mon
831   Weather Rev 144:1877–1885. doi: 10.1175/MWR-D-15-0077.1
832 Madden RA, Julian PR (1971) Detection of a 40–50 Day Oscillation in the Zonal Wind in the Tropical
833   Pacific. J Atmos Sci 28:702–708. doi: 10.1175/1520-0469(1971)028<0702:DOADOI>2.0.CO;2
834 Manhique AJ, Reason CJC, Silinto B, et al (2015) Extreme rainfall and floods in southern Africa in
835   January 2013 and associated circulation patterns. Nat Hazards 77:679–691. doi: 10.1007/s11069-
836   015-1616-y
837 Marshall AG, Hendon HH (2015) Subseasonal prediction of Australian summer monsoon anomalies.
838   Geophys Res Lett 42:10,913-10,919. doi: 10.1002/2015GL067086
839 Mason SJ, Jury MR (1997) Climatic variability and change over southern Africa: a reflection on
840   underlying processes. Prog Phys Geogr 21:23–50. doi: 10.1177/030913339702100103
841 Mchugh MJ, Rogers JC (2001) North Atlantic Oscillation Influence on Precipitation Variability around
842   the Southeast African Convergence Zone. J Clim 14:3631–3642. doi: 10.1175/1520-
843   0442(2001)014<3631:NAOIOP>2.0.CO;2
844 Mitchell JJM, and Dzerdzeevskii B, and Flohn H, et al (1966) Climatic change: report of a working group
845   of the Commission for Climatology. WMO technical note No. 79. WMO, Geneva, Switzerland
846 Mo KC, Nogués-Paegle J (2001) The Pacific-South American modes and their downstream effects. Int J
847   Climatol 21:1211–1229. doi: 10.1002/joc.685
848 Nicholson SE (2000) The nature of rainfall variability over Africa on time scales of decades to millenia.
849   Glob Planet Change 26:137–158. doi: 10.1016/S0921-8181(00)00040-0
850 Nicholson SE (2018) The ITCZ and the Seasonal Cycle over Equatorial Africa. Bull Am Meteorol Soc
851   99:337–348. doi: 10.1175/BAMS-D-16-0287.1
852 Nicholson SE (1996) A review of climate dynamics and climate variability in eastern Africa. In: Johnson,
853   T.C., Odada EZ (ed) The Limnology, Climatology and Paleoclimatology of the East African Lakes.
854   In: Johnson, T.C., Odada, E. Gordon and Breach, Amsterdam, Netherlands, pp 25–56
855 Nogués-Paegle J, Byerle LA, Mo KC (2000) Intraseasonal Modulation of South American Summer
856   Precipitation. Mon Weather Rev 128:837–850. doi: 10.1175/1520-
857   0493(2000)128<0837:IMOSAS>2.0.CO;2
858 OCHA (2015) The 2014/2015 Southern Africa Flood Season. Issue 18. May 2015. South Africa
859 Pohl B, Dieppois B, Crétat J, et al (2018) From Synoptic to Interdecadal Variability in Southern African
860   Rainfall: Toward a Unified View across Time Scales. J Clim 31:5845–5872. doi: 10.1175/JCLI-D-
861   17-0405.1
862 Pohl B, Fauchereau N, Richard Y, et al (2009) Interactions between synoptic, intraseasonal and
863   interannual convective variability over Southern Africa. Clim Dyn 33:1033–1050. doi:
864   10.1007/s00382-008-0485-4
865 Pohl B, Richard Y, Fauchereau N, et al (2007) Influence of the Madden–Julian Oscillation on Southern
866   African Summer Rainfall. J Clim 20:4227–4242. doi: 10.1175/JCLI4231.1
867 Puaud Y, Pohl B, Fauchereau N, et al (2017) Climate co-variability between South America and Southern
868   Africa at interannual, intraseasonal and synoptic scales. Clim Dyn 48:4029–4050. doi:
869   10.1007/s00382-016-3318-x
870 Ramage CS (1971) Monsoon meteorology. Academic Press, New York
871 Reason CJ., Landman W, Tennant W (2006) Seasonal to Decadal Prediction of Southern African Climate
872   and Its Links with Variability of the Atlantic Ocean. Bull Am Meteorol Soc 87:941–956. doi:
873   10.1175/BAMS-87-7-941
874 Reason CJC and, Keibel A (2004) Tropical Cyclone Eline and Its Unusual Penetration and Impacts over
875   the Southern African Mainland. Weather Forecast 19:789–805
876 Richman MB (1986) Rotation of principal components. J Climatol 6:293–335. doi:
877   10.1002/joc.3370060305
878 Schneider U, Ziese M, Meyer-Christoffer A, et al (2016) The new portfolio of global precipitation data
879   products of the Global Precipitation Climatology Centre suitable to assess and quantify the global
880   water cycle and resources. Proc Int Assoc Hydrol Sci 374:29–34. doi: 10.5194/piahs-374-29-2016
881 Silvério K, Kulikova LA (2011) EVALUATION OF POTENTIAL PREDICTORS FOR LONG-TERM
882   FORECAST OF PRECIPITATION IN THE AREA OF MOZAMBIQUE. Russ State
883   Hydrometeorol Univ Proceeding Theor Res journal 21:107–112. doi:

884 http://www.rshu.ru/university/notes/rggmu_uchenye_zapiski_21.pdf

885 Taljaard JJ (1986) Change of rainfall distribution and circulation patterns over Southern Africa in
886 summer. J Climatol 6:579–592. doi: 10.1002/joc.3370060602

887 Torrance JD (1972) Malawi, Rhodesia and Zambia. In: Griffiths JF (ed) Climates of Africa. World
888 Survey of Climatology, Vol. 10. Elsevier, Amsterdam, Netherlands, pp 409–460

889 Vitart F, Ardilouze C, Bonet A, et al (2017) The Subseasonal to Seasonal (S2S) Prediction Project
890 Database. Bull Am Meteorol Soc 98:163–173. doi: 10.1175/BAMS-D-16-0017.1

891 Vitart F, Robertson AW (2018) The sub-seasonal to seasonal prediction project (S2S) and the prediction
892 of extreme events. npj Clim Atmos Sci 1:3. doi: 10.1038/s41612-018-0013-0

893 Wang B, Ding Q (2008) Global monsoon: Dominant mode of annual variation in the tropics. Dyn Atmos
894 Ocean 44:165–183. doi: 10.1016/j.dynatmoce.2007.05.002

895 Wang B, Liu J, Kim H-J, et al (2012) Recent change of the global monsoon precipitation (1979–2008).
896 Clim Dyn 39:1123–1135. doi: 10.1007/s00382-011-1266-z

897 Washington R, Todd M (1999) Tropical-temperate links in southern African and Southwest Indian Ocean
898 satellite-derived daily rainfall. Int J Climatol 19:1601–1616. doi: 10.1002/(SICI)1097-
899 0088(19991130)19:14<1601::AID-JOC407>3.0.CO;2-0

900 Webster PJ, Magaña VO, Palmer TN, et al (1998) Monsoons: Processes, predictability, and the prospects
901 for prediction. J Geophys Res Ocean 103:14451–14510. doi: 10.1029/97JC02719

902 Wheeler MC, Hendon HH (2004) An All-Season Real-Time Multivariate MJO Index: Development of an
903 Index for Monitoring and Prediction. Mon Weather Rev 132:1917–1932. doi: 10.1175/1520-
904 0493(2004)132<1917:AARMMI>2.0.CO;2

905 Wheeler MC, Hendon HH, Cleland S, et al (2009) Impacts of the Madden–Julian Oscillation on
906 Australian Rainfall and Circulation. J Clim 22:1482–1498. doi: 10.1175/2008JCLI2595.1

907 Wiles P, Selvester K, Fidalgo L (2005) Learning Lessons from Disaster Recovery: The Case of
908 Mozambique. Washington DC, USA

909 Wilks DS (2011) Statistical methods in the atmospheric sciences, 3rd edn. Academic Press

910 Xie P, Arkin PA (1997) Global Precipitation: A 17-Year Monthly Analysis Based on Gauge
911 Observations, Satellite Estimates, and Numerical Model Outputs. Bull Am Meteorol Soc 78:2539–
912 2558. doi: 10.1175/1520-0477(1997)078<2539:GPAYMA>2.0.CO;2

913 Yim S-Y, Wang B, Liu J, Wu Z (2014) A comparison of regional monsoon variability using monsoon
914 indices. Clim Dyn 43:1423–1437. doi: 10.1007/s00382-013-1956-9

915 Zaitchik BF (2017) Madden-Julian Oscillation impacts on tropical African precipitation. Atmos Res
916 184:88–102. doi: 10.1016/j.atmosres.2016.10.002

917 Zhang C (2013) Madden–Julian Oscillation: Bridging Weather and Climate. Bull Am Meteorol Soc
918 94:1849–1870. doi: 10.1175/BAMS-D-12-00026.1

919 Zhou J, Lau K-M (1998) Does a Monsoon Climate Exist over South America? J Clim 11:1020–1040. doi:
920 10.1175/1520-0442(1998)011<1020:DAMCEO>2.0.CO;2

921

922

Figure captions

Fig. 1 (a) Southern Africa (SAF) topography (in meters) at 0.5° grid resolution, obtained from the International Centre for Theoretical Physics (ICTP; http://clima-dods.ictp.it/regcm 4/). Meteostations in Mozambique are represented by triangles. (b) Annual rainfall cycles over SAF obtained from the Global Precipitation Climatology Centre (GPCC) data for the period 1979–2005. The red box indicates the region selected for definition of the monsoon precipitation index (MPI), described in the text (section 5)

Fig. 2 Summer (DJF) seasonal mean streamlines at (a) 850 hPa and (b) 200 hPa. In (a) AL and MCT denote Angola Low and Mozambique Channel Trough, while SAH and SIH indicate subtropical South Atlantic High and South Indian High. Blue lines indicate northeasterly (NEM) and westerly or northwesterly (NWM) monsoon flows, as well as southeast trade winds (SETW). Green solid line denotes Congo Air Boundary (CAB) and green dashed line the Intertropical Convergence Zone (ITCZ). In (b) BH indicates Botswana High and the rectangle indicates the region selected for the monsoon precipitation index. The colour bar denotes the values of seasonal mean monthly rainfall, according to GPCC data averaged over 1979–2005

Fig. 3 Rotated empirical orthogonal functions (REOFs) of the summer daily precipitation over eastern SAF in the 10–25 day (top row), 10–90 day (2nd row), and 20–90 day (3rd row) bands. From left to right are REOF1, REOF2, REOF3, and REOF4 (or REOF5, for 10–25 day band). The purple box indicates the region of the monsoon precipitation index (MPI, defined in section 5). The number in the lower-right corner of each panel is the correlation coefficient between the factor scores and MPI, with bold (italic) values statistically significant at the 99 (95) % confidence level. The bottom panel shows the factor scores series of the 20–90 day band REOF3

Fig. 4 Simultaneous correlation coefficient maps between the components of the 850 hPa wind anomalies and the factor scores of the 20–90 day band (a) REOF1, (b) REOF2, (c) REOF3, (d) REOF4. Only vectors with at least one component with confidence level better than 95% are shown
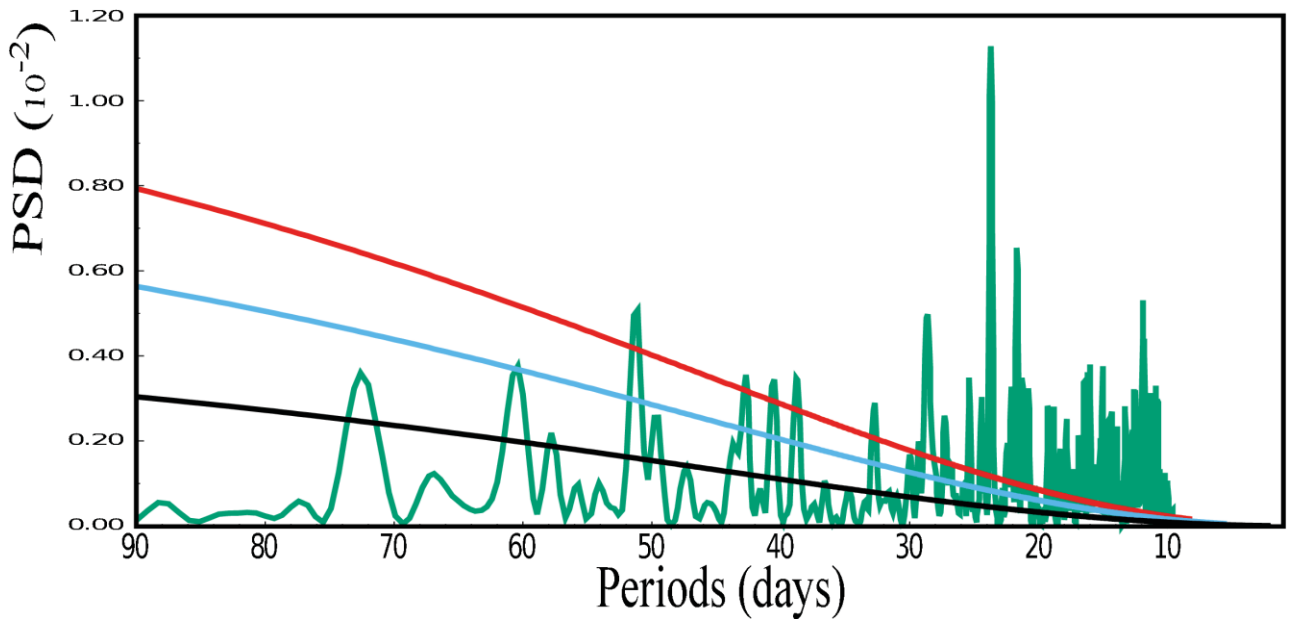
Fig. 5 Power spectral density of REOF3 time series in the 10–90 day band. Solid lines indicate calculated spectrum (green), red noise (black) and curves of 95% and 99 % confidence limits (blue and red)

Fig. 6 Difference between anomaly composites in the 10–25 day band for REOF3 positive and negative phases, showing 200 hPa eddy streamfunction (contours) and OLR (shades). Negative numbers in the top right corner are days before the first day of positive phase (– 0), while the positive numbers are days after the last day of positive phase (+0), and (0 All) is the average over all days of positive phase. Contour interval is 0.5 x 10^{-6} m^2 s^{-1}, and zero contour is omitted. Dark yellow (purple) contours represent positive (negative) values, and stippled areas have confidence level above 95%. OLR anomalies are indicated in the bottom color bar, and only those with confidence level above 95% are shown. The bottom right panel is an approximate scheme for the temporal evolution of the anomaly composite oscillation

Fig. 7 Difference between anomaly composites in the 20–90 day band for REOF3 positive and negative phases, showing 850 hPa eddy streamfunction (contours) and CPC rainfall (shades). Negative numbers in the top right corner are days before the first day of positive phase (– 0), while the positive numbers are days after the last day of positive phase (+0), and (0 All) is the average over all days of positive phase. Contour interval is 0.5 x 10^{-6} m^2 s^{-1}, and zero contour is omitted. Dark yellow (purple) contours represent positive (negative) values, and stippled areas have confidence level above 95%. OLR anomalies are indicated in the bottom color bar, and only those with confidence level above 95% are shown. The bottom right panel is an approximate scheme for the temporal evolution of the anomaly composite oscillation

Fig. 8 Same as Fig. 7, but for 200 hPa eddy streamfunction and OLR anomalies. Contour interval is 1.0 x 10^{-6} m^2 s^{-1} and zero contour is omitted

Fig. 9 Simultaneous correlation maps between the gauge daily summer monsoon MPI and (a) daily rainfall from CPC data, (b) zonal and (c) meridional winds at 850 hPa. The color bar indicates levels of significance for positive and negative correlations. The rectangles indicate the regions over which the circulation variables are averaged to define the monsoon circulation indices. See Table 1 for definition of the indices
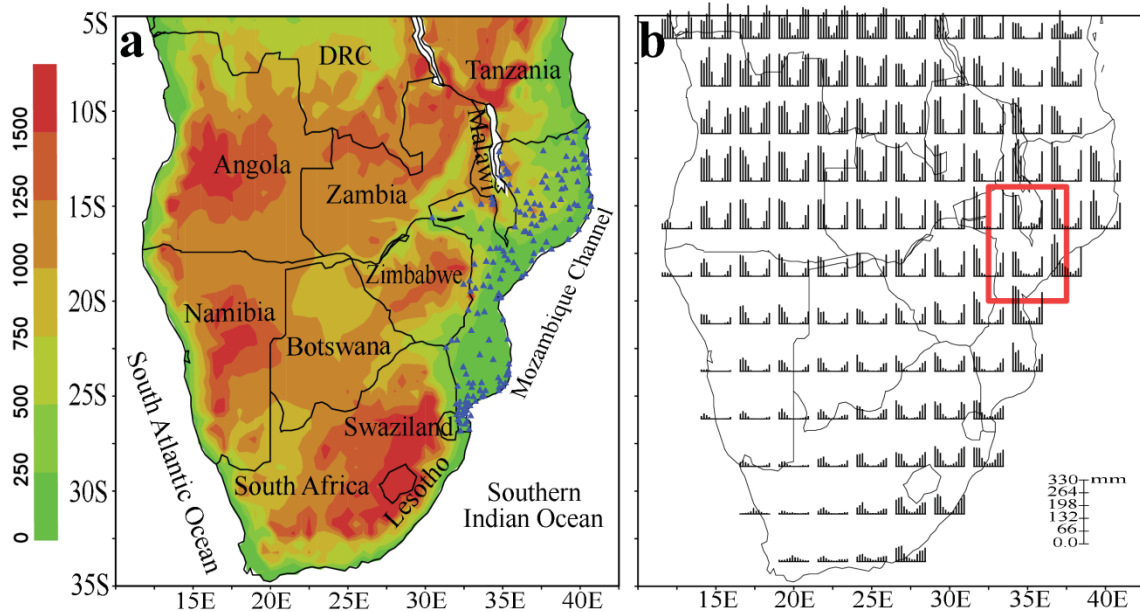
982 **Fig. 10** Simultaneous correlation maps between the CPC summer monsoon rainfall and each of the
983 monsoon indices named at the lower right corner of each panel. The number indicates the correlation
984 coefficient between the MPI gauge data and each of the indices. The color bar indicates levels of
985 significance for positive and negative correlations. See Table 1 for definition of the indices
986
987 **Fig. 11** Standardized anomalies of daily monsoon indices for DJF seasons in (a) 1996–1997 and (b)
988 1999–2000. MPMI calculated with gauge and CPC data is indicated respectively by the black solid and
989 black dotted lines, whereas MVlZE and VORT are represented by the solid blue and red lines,
990 respectively. The positive ZWVI or CI values indicate westerly (cyclonic) wind anomalies accompanied
991 with enhanced rainfall as described by positive MPMI. The inverse is true for suppressed rainfall. Green
992 lines indicate the $\pm$ 0.7 standardized anomalies, above or below which the monsoon is in an active or
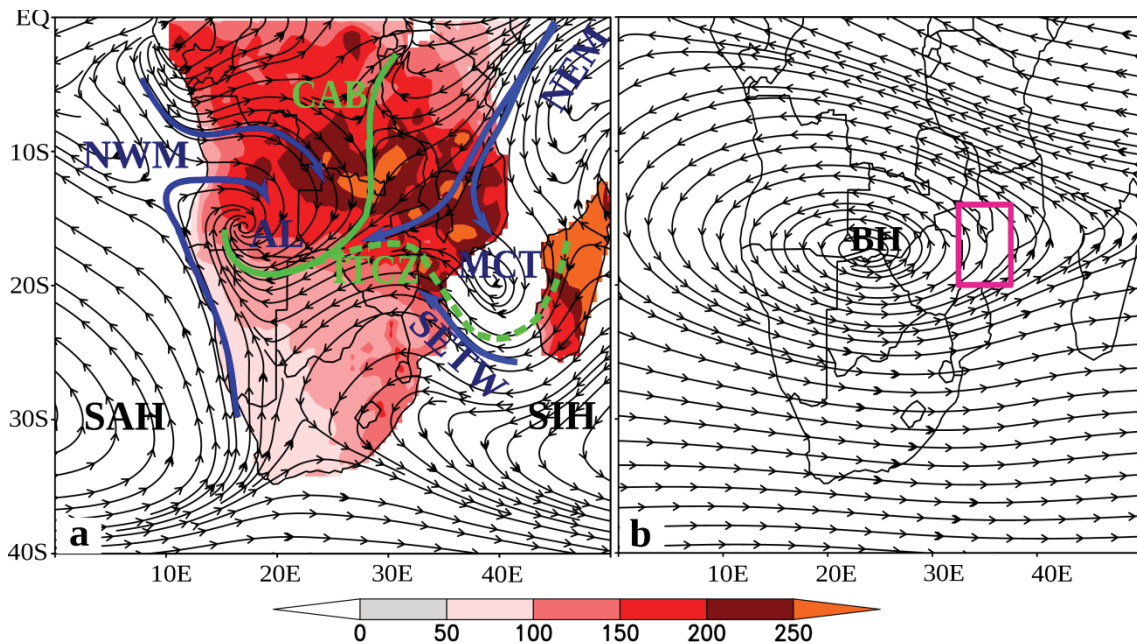993 break phase

Table 1 Correlation coefficients between daily non-filtered MPI and monsoon circulation indices. All are statistical significant at 99 % confidence level. The correlation coefficient between MPI calculated with gauge and CPC data is 0.57. In bold are the highest correlation coefficients between MPI and indices composed of one, two, three and four elements (see text), besides the highest value, obtained with an index of averaged vorticity.

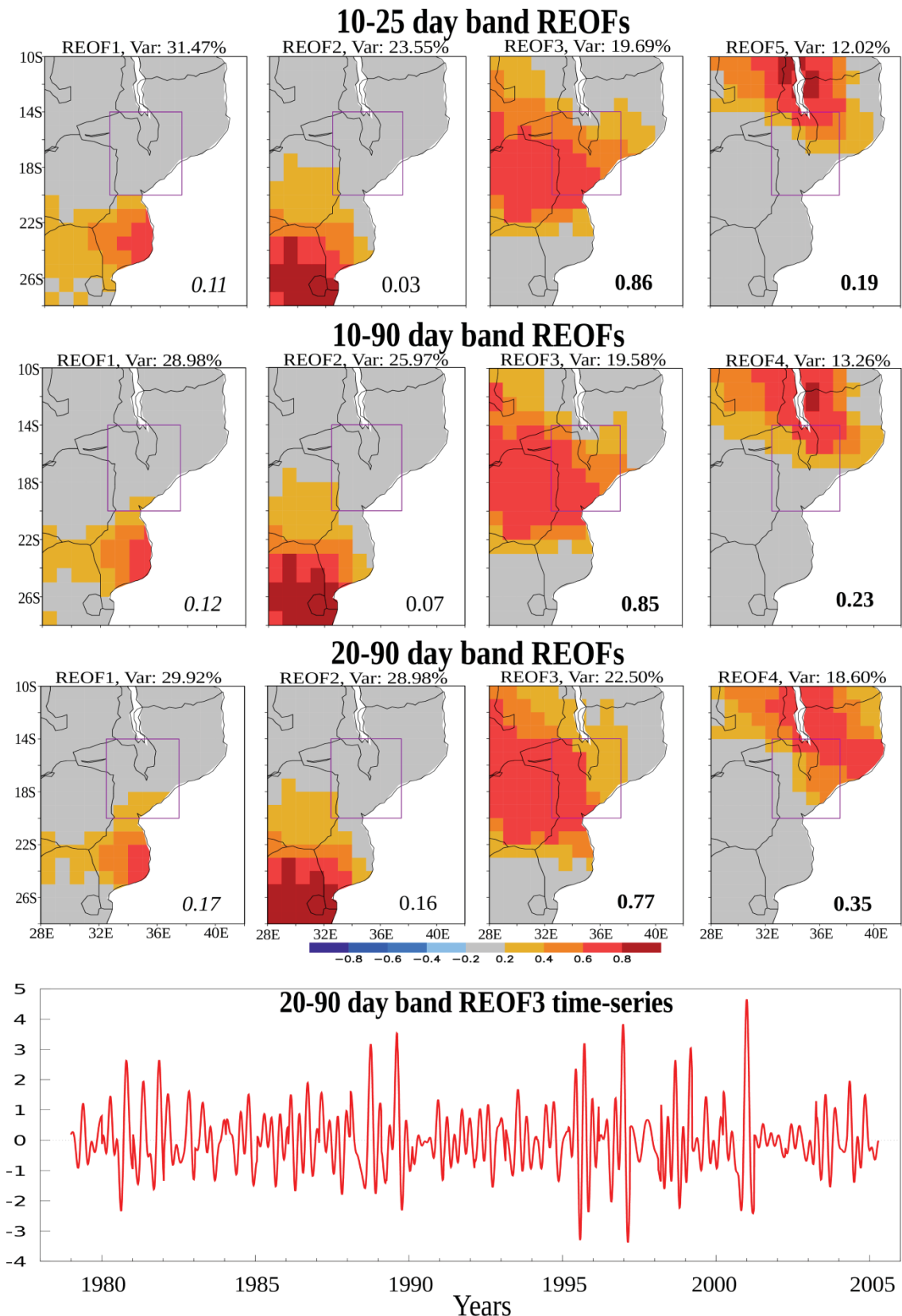| Indices	Acronyms	Domains (or formulae)	Correl. with MPI gauge data	Correl. with MPI CPC data
Zonal westerly wind index	ZWWI	7.5°S–14°S, 19.5°E–36.5°E	0.153	0.195
Zonal easterly wind index	ZEWI	19.5°S–25°S, 25°E–41°E	**-0.297**	-0.272
Meridional northerly wind index, over area northeast of MPMI area	MNWI	7.5°S–18.5°S, 36.5°E–44.5°E	-0.199	-0.211
Meridional southerly wind index 1, over elongated area west of MPMI area	MSWI1	15°S–20°S, 15.5°E–33.5°E	0.244	0.256
Meridional southerly wind index 2, over area west of MPMI area	MSWI2	15°S–25°S, 26.75°E–33.5°E	0.237	0.252
Zonal wind vorticity index	ZWVI	ZWWI–ZEWI	0.315	0.327
Meridional wind vorticity index 1	MWVI1	MSWI1–MNWI	0.309	0.327
Meridional wind vorticity index 2	MWVI2	MSWI2–MNWI	0.317	0.337
Zonal westerly wind index minus Meridional northerly wind index	ZWMN	ZWWI-MNWI	0.205	0.237
Zonal westerly wind index plus Meridional southerly wind index 1	ZWMS1	ZWWI+MSWI1	0.266	0.303
Zonal westerly wind index plus Meridional southerly wind index 2	ZWMS2	ZWWI+MSWI2	0.269	0.309
Zonal easterly wind index plus Meridional northerly wind index	ZEMN	ZEWI+MNWI	**-0.381**	-0.371
Zonal easterly wind index minus Meridional southerly wind index 1	ZEMS1	ZEWI-MSWI1	-0.322	-0.315
Zonal easterly wind index minus Meridional southerly wind index 2	ZEMS2	ZEWI-MSWI2	-0.313	-0.307
Zonal wind vorticity index minus Meridional northerly wind index	ZVMN	ZWVI–MNWI	0.339	0.355
Zonal wind vorticity index plus Meridional southerly wind index 1	ZVMS1	ZWVI+MSWI1	0.343	0.358
Zonal wind vorticity index plus Meridional southerly wind index 2	ZVMS2	ZWVI+MSWI2	0.341	0.356
Meridional wind vorticity index 1 plus zonal westerly wind index	MV1ZW	MWVI1+ZWWI	0.291	0.324
Meridional wind vorticity index 2 plus zonal westerly wind index	MV2ZW	MWVI2+ZWWI	0.298	0.333
Meridional wind vorticity index 1 minus zonal easterly wind index	MV1ZE	MWVI1–ZEWI	**0.392**	0.392
Meridional wind vorticity index 2 minus zonal easterly wind index	MV2ZE	MWVI2–ZEWI	**0.392**	0.393
Zonal wind vorticity index plus Meridional wind vorticity index 1	ZMVort1	ZWVI+MWVI1	0.372	0.389
Zonal wind vorticity index plus Meridional wind vorticity index 2	ZMVort2	ZWVI+MWVI2	**0.376**	0.395
Vorticity index (averaged vorticity)	VORT	11.75°S–22°S, 30°E–39°E	**-0.395**	-0.393

Fig. 1 (a) Southern Africa (SAF) topography (in meters) at 0.5° grid resolution, obtained from the International Centre for Theoretical Physics (ICTP; http://clima-dods.ictp.it/regcm 4/). Meteostations in Mozambique are represented by triangles. (b) Annual rainfall cycles over SAF obtained from the Global Precipitation Climatology Centre (GPCC) data for the period 1979–2005. The red box indicates the region selected for definition of the monsoon precipitation index (MPI), described in the text (section 5)
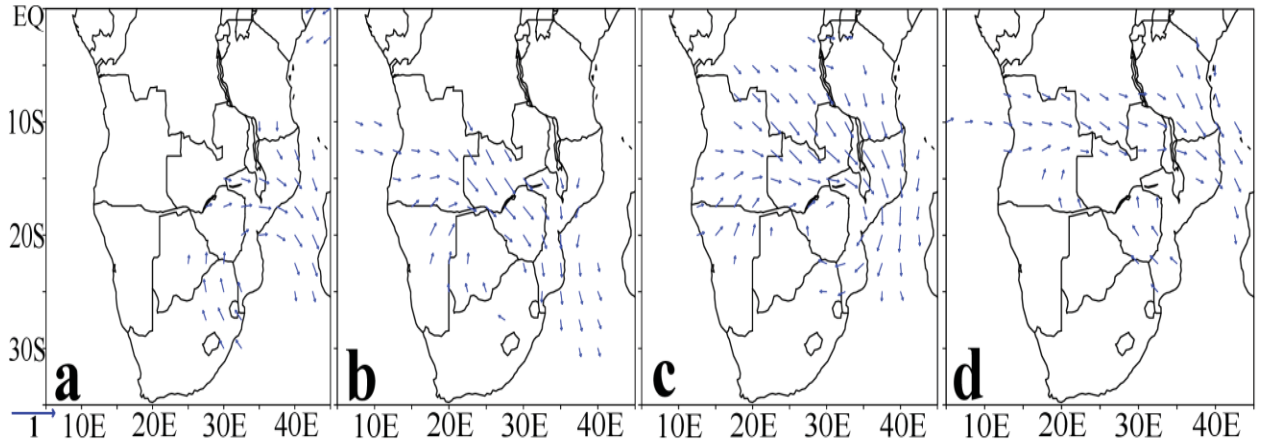

Fig. 2 Summer (DJF) seasonal mean streamlines at (a) 850 hPa and (b) 200 hPa. In (a) AL and MCT denote Angola Low and Mozambique Channel Trough, while SAH and SIH indicate subtropical South Atlantic High and South Indian High. Blue lines indicate northeasterly (NEM) and westerly or northwesterly (NWM) monsoon flows, as well as southeast trade winds (SETW). Green solid line denotes Congo Air Boundary (CAB) and green dashed line the Intertropical Convergence Zone (ITCZ). In (b) BH indicates Botswana High and the rectangle indicates the region selected for the monsoon precipitation index. The colour bar denotes the values of seasonal mean monthly rainfall, according to GPCC data averaged over 1979–2005

Fig. 3 Rotated empirical orthogonal functions (REOFs) of the summer daily precipitation over eastern SAF in the 10–25 day (top row), 10–90 day (2nd row), and 20–90 day (3rd row) bands. From left to right are REOF1, REOF2, REOF3, and REOF4 (or REOF5, for 10–25 day band). The purple box indicates the region of the monsoon precipitation index (MPI, defined in section 5). The number in the lower-right corner of each panel is the correlation coefficient between the factor scores and MPI, with bold (italic) values statistically significant at the 99 (95) % confidence level. The bottom panel shows the factor scores series of the 20–90 day band REOF3
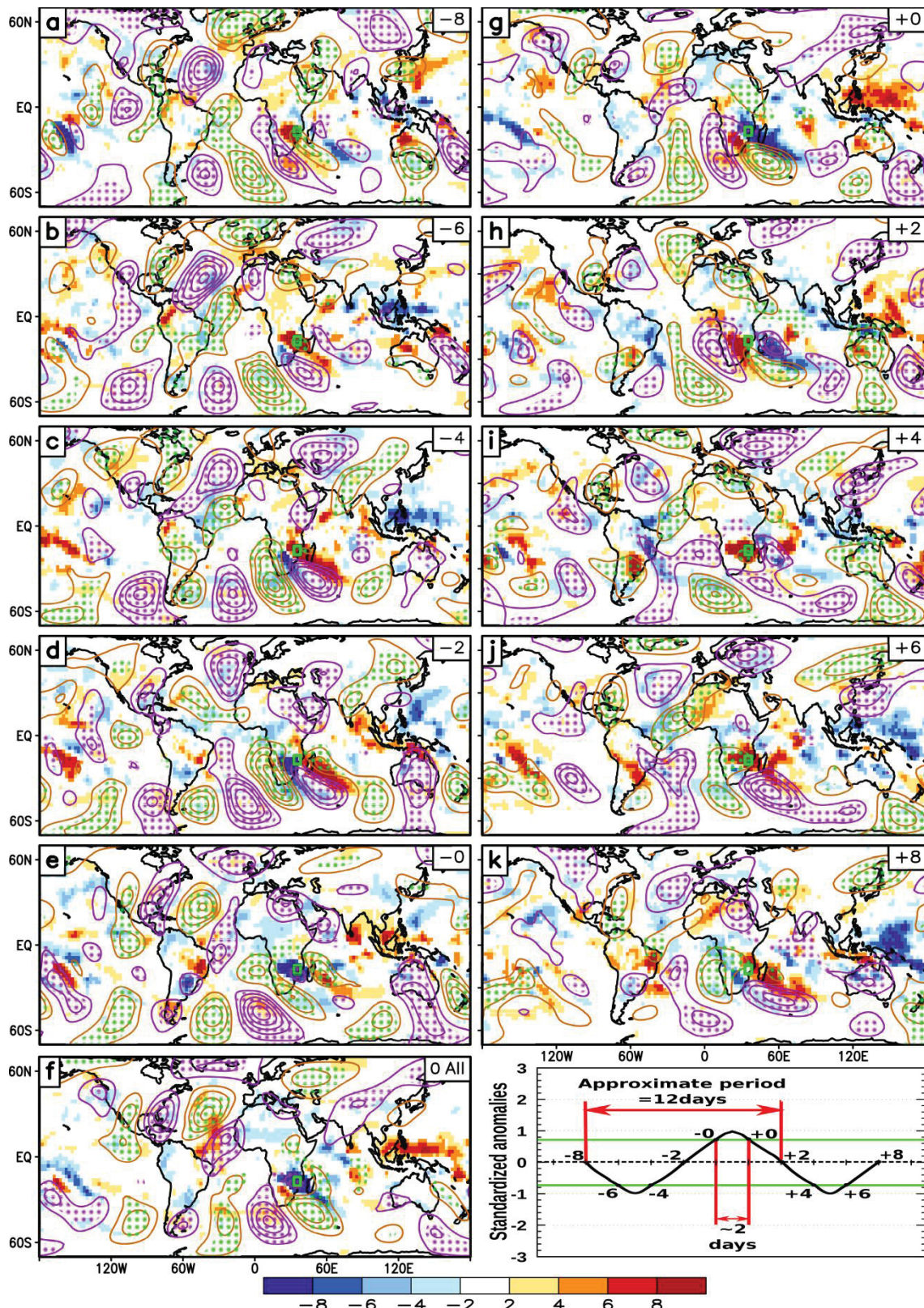
1029 .
1030
1031

1032
1033
1034 **Fig. 4** Simultaneous correlation coefficient maps between the components of the 850 hPa wind anomalies
1035 and the factor scores of the 20–90 day band (a) REOF1, (b) REOF2, (c) REOF3, (d) REOF4. Only
1036 vectors with at least one component with confidence level better than 95% are shown
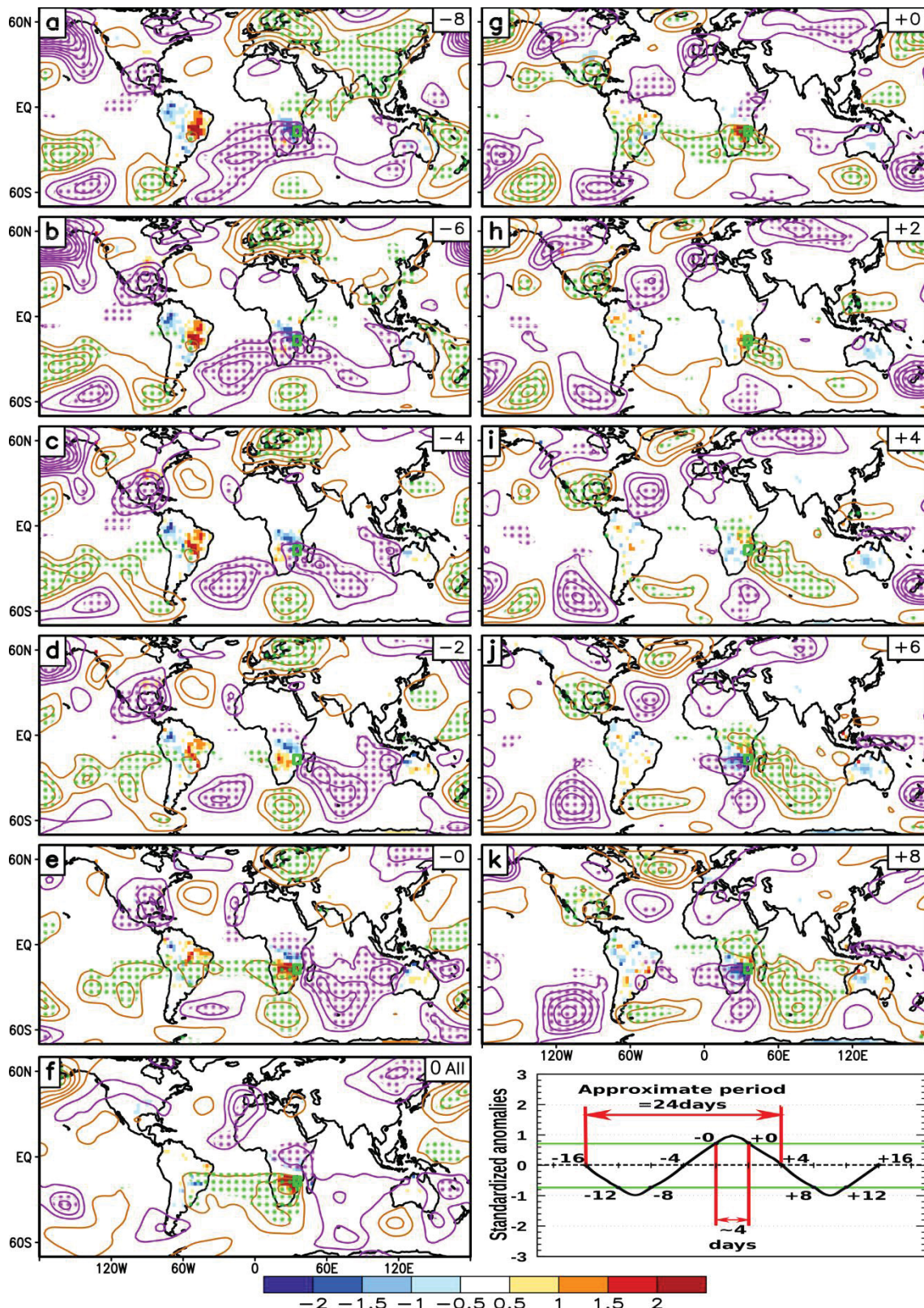1037
1038
1039
1040
1041

1042
1043
1044 **Fig. 5** Power spectral density of REOF3 time series in the 10–90 day band. Solid lines indicate calculated
1045 spectrum (green), red noise (black) and curves of 95% and 99 % confidence limits (blue and red)
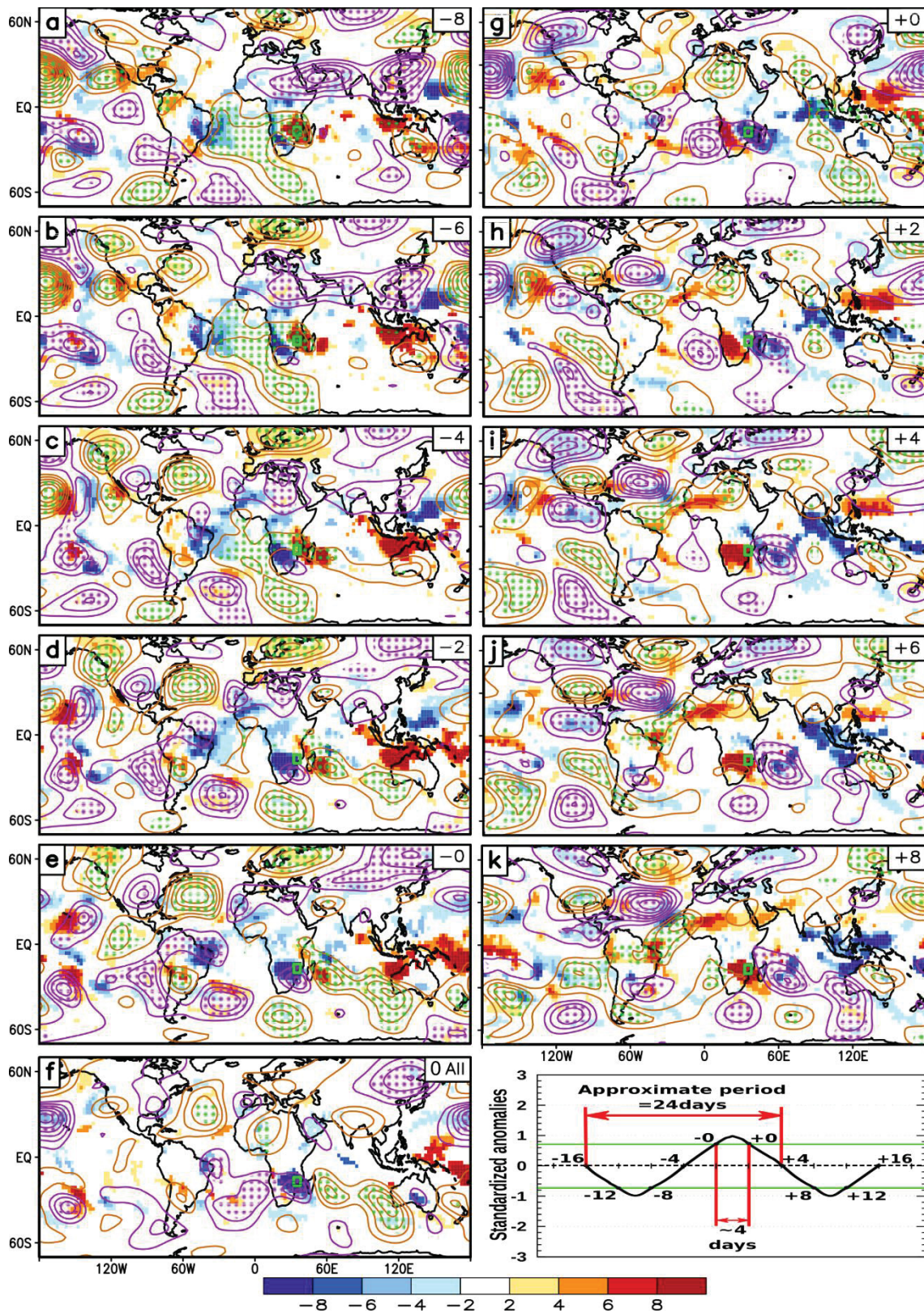1046
1047
1048
1049

Fig. 6 Difference between anomaly composites in the 10–25 day band for REOF3 positive and negative phases, showing 200 hPa eddy streamfunction (contours) and OLR (shades). Negative numbers in the top right corner are days before the first day of positive phase (– 0), while the positive numbers are days after the last day of positive phase (+0), and (0 All) is the average over all days of positive phase. Contour interval is 0.5×10^{-6} m^2 s^{-1}, and zero contour is omitted. Dark yellow (purple) contours represent positive (negative) values, and stippled areas have confidence level above 95%. OLR anomalies are indicated in the bottom color bar, and only those with confidence level above 95% are shown. The bottom right panel is an approximate scheme for the temporal evolution of the anomaly composite oscillation

Fig. 7 Difference between anomaly composites in the 20–90 day band for REOF3 positive and negative phases, showing 850 hPa eddy streamfunction (contours) and CPC rainfall (shades). Negative numbers in the top right corner are days before the first day of positive phase (− 0), while the positive numbers are days after the last day of positive phase (+0), and (0 All) is the average over all days of positive phase. Contour interval is 0.5×10^{-6} m^2 s^{-1}, and zero contour is omitted. Dark yellow (purple) contours represent positive (negative) values, and stippled areas have confidence level above 95%. OLR anomalies are indicated in the bottom color bar, and only those with confidence level above 95% are shown. The bottom right panel is an approximate scheme for the temporal evolution of the anomaly composite oscillation
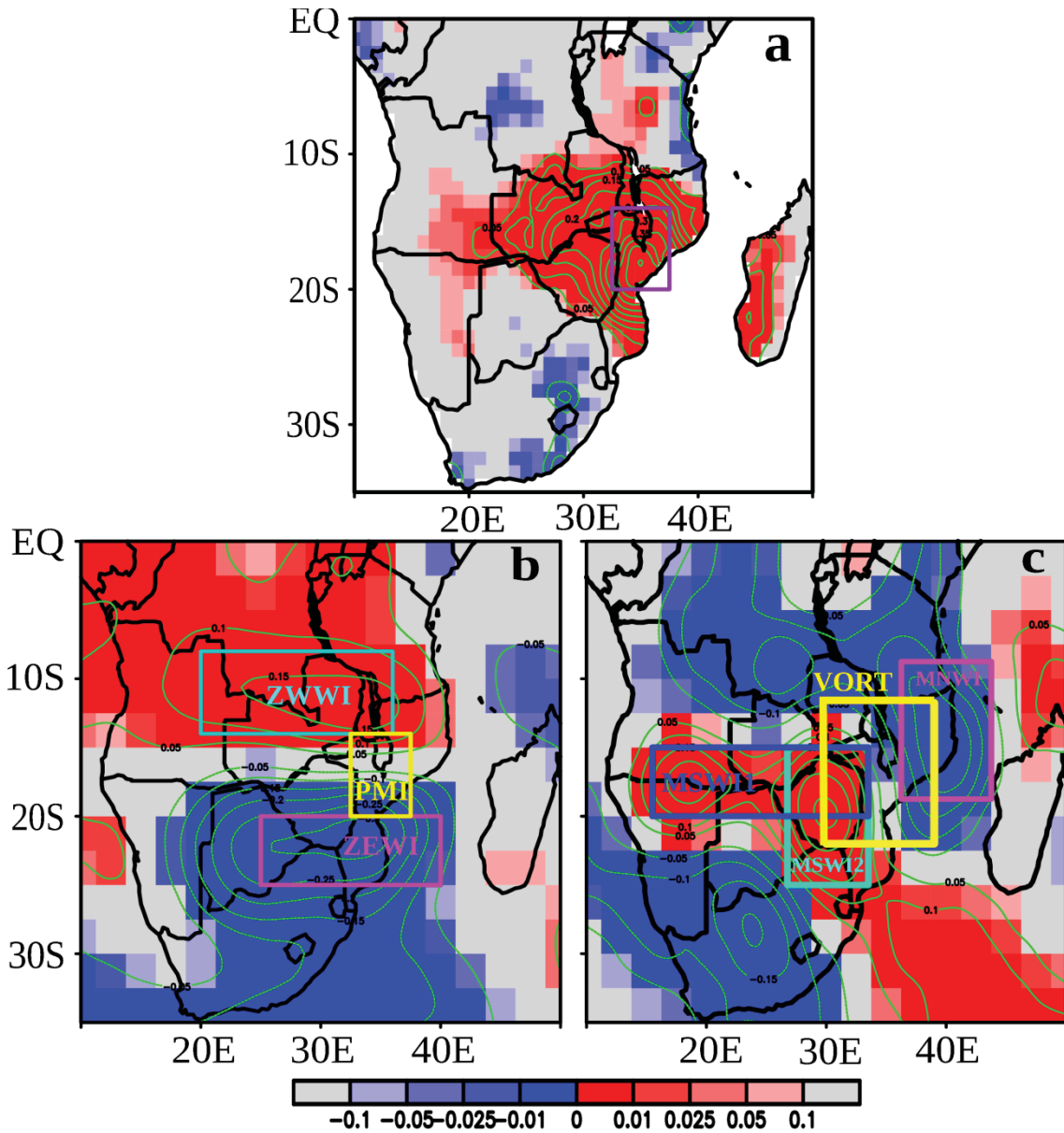
Fig. 8 Same as Fig. 7, but for 200 hPa eddy streamfunction and OLR anomalies. Contour interval is $1.0 \times 10^{-6} \, \mathrm{m^2 \, s^{-1}}$ and zero contour is omitted

Fig. 9 Simultaneous correlation maps between the gauge daily summer monsoon MPI and (a) daily rainfall from CPC data, (b) zonal and (c) meridional winds at 850 hPa. The color bar indicates levels of significance for positive and negative correlations. The rectangles indicate the regions over which the circulation variables are averaged to define the monsoon circulation indices. See Table 1 for definition of the indices

Fig. 10 Simultaneous correlation maps between the CPC summer monsoon rainfall and each of the monsoon indices named at the lower right corner of each panel. The number indicates the correlation coefficient between the MPI gauge data and each of the indices. The color bar indicates levels of significance for positive and negative correlations. See Table 1 for definition of the indices
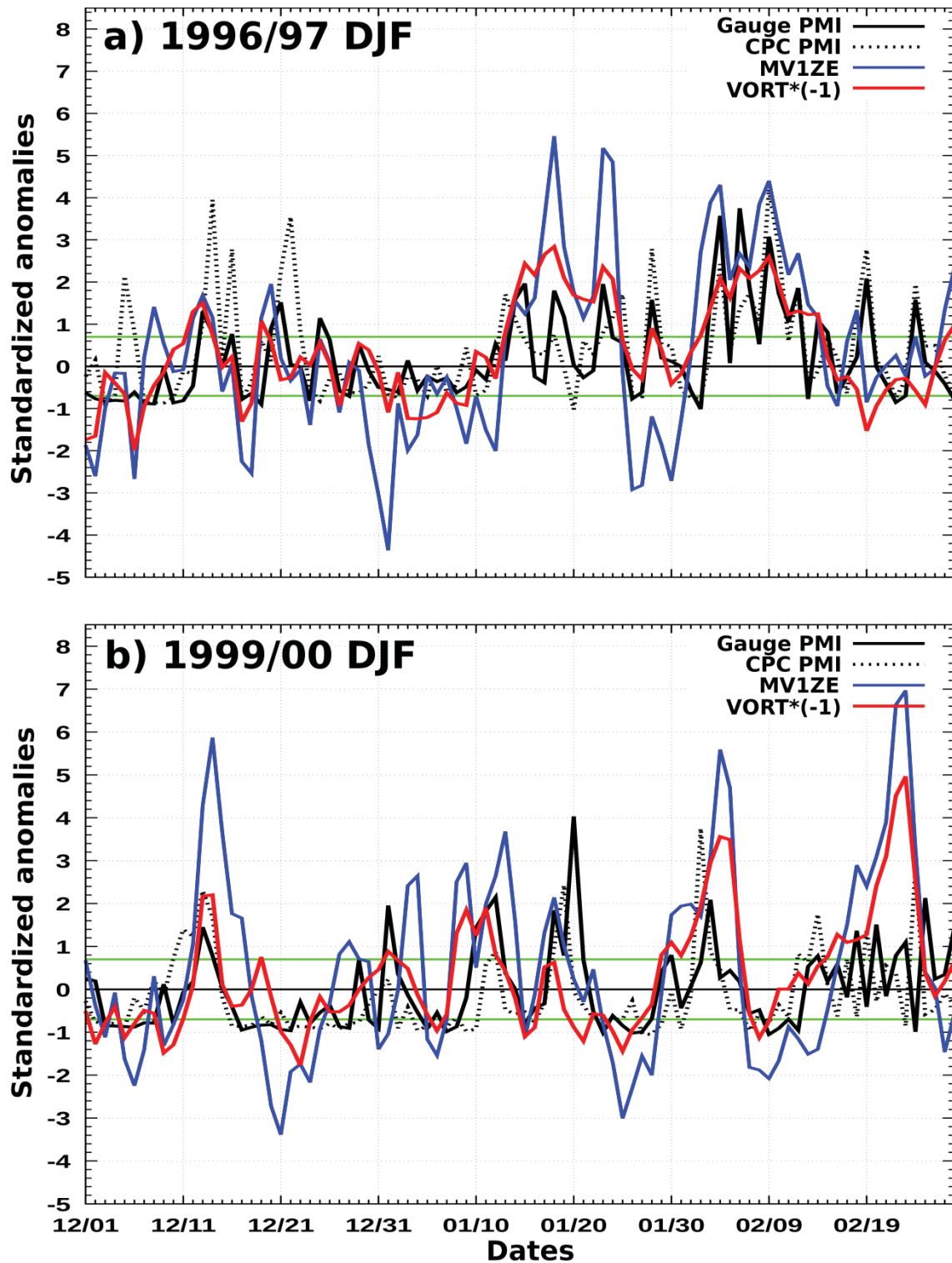
Fig. 11 Standardized anomalies of daily monsoon indices for DJF seasons in (a) 1996–1997 and (b) 1999–2000. MPMI calculated with gauge and CPC data is indicated respectively by the black solid and black dotted lines, whereas MV1ZE and VORT are represented by the solid blue and red lines, respectively. The positive ZWVI or CI values indicate westerly (cyclonic) wind anomalies accompanied with enhanced rainfall as described by positive MPMI. The inverse is true for suppressed rainfall. Green lines indicate the ± 0.7 standardized anomalies, above or below which the monsoon is in an active or break phase

5. Subseasonal prediction skill of southern Africa monsoon anomalies

Situated in eastern SAF, the southern Africa monsoon region is an area with approximately 100 million inhabitants, most of whom living in rural areas and whose subsistence heavily relies on agriculture. Besides that, most of the energy consumed in this region comes from hydropower generation. The success of both agricultural production and hydropower generation, the key sectors to the development of the countries in the region, strongly depends on availability of water resources, supplied in the region mainly by the monsoon rainfall, which usually occurs during DJF months. However, the monsoon rainfall, besides undergoing year-to-year variation in its distribution, also shows significant ISV, characterized by active and break periods. Thus, besides the prediction of the overall strength of monsoon rainfall in a particular year, it is also important predicting its monsoon active and break episodes, as their knowledge is of great societal and economical value in the highly populated Mozambique provinces, especially during the monsoon season, when frequent extreme rainfall occur, associated sometimes with tropical cyclones incursions. In this line, this study assesses the ability of all 11 S2S project models in reproducing the SAFM subseasonal anomalies through the monsoon indices derived in Chapter 4. This assessment is made at multiweek lead times out to 4 weeks using retrospective forecast (hindcasts) data over the S2S models commom period (1999–2010). For countries like Mozambique historically vulnerable to extreme events (droughts, floods, and tropical cyclones), this type of forecast will improve preventive action when and where it is needed, as it does have neither adequate telecommunication infractructure nor financial and technological capacity.

Multiweek prediction performance of southern Africa monsoon anomalies in the subseasonal to seasonal (S2S) project database

Kénedy Cipriano Silvério [1,2,*], and Alice Marlene Grimm [2,3]

[1] Higher Polytechnic Institute of Songo (ISPS), Songo-Tete, Mozambique

[2] Postgraduate Program in Water Resources and Environmental Engineering (PPGERHA), Federal University of Paraná (UFPR)

[3] Department of Physics, Federal University of Parana (UFPR), Curitiba, Brazil

Abstract

Previous work on intraseasonal variability of southern Africa monsoon, proposed a monsoon precipitation index (MPI) as well as some monsoon circulation indices, in order to help characterizing, monitoring, and predicting the monsoon intraseasonal variability (active and break periods). Here, using this MPI and one of the suggested monsoon circulation indices, we assess the predictive ability of all 11 subseasonal to seasonal (S2S) project models in simulating monsoon active and break periods over southern Africa for the period 1999–2010. Although the models can predict the local large-scale zonal wind anomalies for lead times beyond 3 weeks, predictive ability of monsoon precipitation anomalies is limited to a week. The model's rank showed ECMWF, JMA, UKMO, CNRM, KMA and NCEP as the top scoring ones. The observed monsoon active periods are associated with an eastward propagating wave train that seems to be produced by convection over South America and the Atlantic Ocean. All selected models tend to reproduce the convective anomalies associated with observed monsoon active periods, although not all reproduce their associated circulation anomalies. This is likely due to the errors associated with model deficiencies in representing teleconnections.

KEY WORD: Southern Africa Monsoon Rainfall, Intraseasonal Variability, MJO, S2S Models, Teleconnections between South America and southern Africa.

_____

[*] _Corresponding author address_: PPGERHA–UFPR, CP 19011, CEP 81531-990, Curitiba, Brazil. E-mail: kenedysilverio@mail.ru

1 Introduction

Prediction of the impending meteorological conditions at lead-times of short (1–5 days) to medium-range (7–15 days) and long or climate scale (>30 days) are routinely issued by national weather services around the globe.

The longest lead time at which currently a weather forecast is skillful is, on average, about one week, which is a good lead time compared to that of six decades ago when it was approximately a day (Lin et al. 2008; Bauer et al. 2015). Beyond a week, due to the chaotic nature of the atmosphere, growth of initial errors and imperfections of the models, weather forecast errors become so large that a prediction contains little useful information (Lin et al. 2008). On the other hand, seasonal (climate) prediction that is based on the premise that there is long-range forecasting memory residing in underlying boundary conditions (e.g., surface temperature, soil moisture, sea ice, etc.) has also significantly improved during the last 3–4 decades or so thanks to the coordinated efforts under the World Climate Research Program (WCRP), being now possible predicting for example sea surface temperature (SST) anomalies associated with the El Niño Southern Oscillation (ENSO) at least 6 months ahead (Mariotti et al. 2018). This improvement of climate forecasts, as of weather predictions, has resulted in an increased preparedness with significant economic savings and societal benefits in many countries across the globe.

Nonetheless, there remain some fundamental problems that limit the use of these forecasts. Firstly, the short-to-medium-range weather scales appear too short for meaningful mitigating action to be taken (Olaniyan et al. 2018). Secondly, in between the short-to-medium and climate ranges (seasonal outlooks), there is effectively a predictive temporal gap, referred to as the subseasonal to seasonal (S2S) or extended time range (from 15- to 30-day).

Although forecasts at S2S timescale have the potential to bridge the gap between the more mature medium-range and seasonal predictions by providing the weekly updated forecast information of intermediate specificity about the risks of extreme events up to several weeks ahead, they have so far received much less attention than the predictions on other scales (Vitart et al. 2012; White et al. 2017; Robertson et al. 2018). This is why the S2S time-range has been seen until recently as a "predictability desert". It is remarkably influenced by both (1) the initial conditions of the atmosphere, which are the primary predictability source for the short-to-medium-range weather forecast (Lorenz 1963, 1969) and (2) the more slowly evolving boundary conditions (forcings) such as soil moisture, snow cover, sea-ice components, and SSTs, all upon which depends the predictability of long-range forecasts (Palmer and Anderson 1994; Shukla 1998). These different aspects and time scales associated make the S2S forecasting an especially challenging task (Doblas-Reyes et al. 2013). However, recent research on sources of predictability at subseasonal timescale, such as the Madden–Julian oscillation (MJO; Madden and Julian 1971), stratosphere–troposphere interactions, tropical–extratropical teleconnections, along with their interaction with the boundary forcings, which evolve more slowly over timescales of weeks to years have changed that picture (Vitart et al. 2012; Robertson et al. 2018). Via interactions with the atmosphere, the slowly evolving Earth system components provide boundary conditions to guide with increased degree of reliability the atmospheric predictability beyond two weeks (Mariotti et al. 2018). Obviously, the skill of a particular forecast will strongly depend on how active some phenomena (e.g., MJO, ENSO) are during the forecast period, and how strongly they impact the study domain (Vigaud et al. 2017b). For a comprehensive review on a full assessment of these and other S2S predictability sources together with the recent advances, the readers are referred to, among others, National Research Council (2010) and Vitart et al. (2015) and references therein.

To sustain the current successful efforts and foster the scientific researches on continuing the evolution toward seamless approach to the weather–climate prediction continuum, the World Weather Research Program (WWRP) jointly with the WCRP launched in 2013 a 5-year international research collaborative initiative called the S2S project (Vitart and Robertson 2018), which was extended in 2019 for an additional 5 years (http://www.s2sprediction.net/). The

main goal of this project is to improve forecast skill and understanding the predictability sources at subseasonal time range, and to promote its uptake by operational centers and exploitation by the applications communities (http://www.s2sprediction.net/). An important outcome of this initiative has been the establishment of an extensive database containing near-real-time (3 weeks behind) and retrospective forecasts with lead-times up to approximately 30–60 days (Vitart et al. 2017). This database which is sourced by 11 operational and research meteorological centers represents an unprecedented resource for researchers, and other interested parties to better exploit, understand, and ultimately improve the S2S predictions (Robertson et al. 2018).

The predictive skill of the global operational state-of-the-art S2S project models in simulating the different meteorological variables has been assessed at different spatial scales, including global (Liu et al. 2015; Bombardi et al. 2017; de Andrade et al. 2019), regional (e.g., Liu et al. 2015, 2017; Ardilouze et al. 2017; Lee et al. 2017, 2018; Jie et al. 2017; Vigaud et al. 2017a,b; Osman and Alvarez 2018; Lin 2018), and local (e.g., Marshall and Hendon 2015; Baggett et al. 2017; Wang et al. 2017; Vitart and Robertson 2018; Olaniyan et al. 2018; Hirata and Grimm 2018; Wang and Robertson 2018; Vuillaume et al. 2018; Lin et al. 2018). The results derived from these studies appear overall encouraging, as the prediction, for example, of the onset, evolution and decay of some large-scale extreme events occurred in the past have been shown that might be predicted several weeks ahead, possibly associated with MJO teleconnections (Vitart and Robertson 2018; Robertson et al. 2018).

Notwithstanding these encouraging results, none of those studies to our knowledge have attempted to address specifically on southern Africa monsoon (SAFM) characteristics (e.g., rainfall), despite the potential benefits of these forecasts for this region, given its high vulnerability to extreme events (Reason et al. 2006; White et al. 2017). Furthermore, studies performed for greater domain, such as those by Liu et al. (2015) and de Andrade et al. (2019) may fail capturing the response of the regional/local features to the impact of large-scale circulation, associated, for example, with rainfall variability in the region. This issue provides the impetus for this study, in which the performance of all 11 S2S models in predicting the active and break monsoon episodes and its associated circulation patterns at multiweek lead times (up to 4 weeks) over southern Africa ("SAF", Africa subcontinent south of 10°S) is assessed following a similar methodology applied by Marshall and Hendon (2015; hereafter referred to as MH15). As the MJO is considered to be the primary source for subseasonal predictability (Neena et al. 2014), an additional assessment of the capability of these models in simulating the MJO impacts on predictability of active and break monsoon episodes over the study domain is carried out. To define active and break monsoon episodes, the same monsoon indices defined in Silvério and Grimm (2020; hereafter referred to as SG20) are used as will be shown in subsection 2.3.

This study concentrates on SAF monsoon region (see section 3.1 and SG20 for its definition), a region with approximately 100 million inhabitants, most of whom living in rural areas and whose subsistence heavily relies on agriculture. Besides that, most of the energy consumed in this region comes from hydropower generation. The success of both agriculture and hydropower generation, the key sectors for the development of the countries in the region, strongly depends on availability of water resources, supplied mainly by the monsoon rainfall, which usually occurs during December-January-February (DJF). This suggests that skillful forecasts can have a great societal and economical value for countries in this region, especially during the monsoon season, when the extreme events, such as persistent heavy rainfalls, sometimes associated with tropical cyclones incursion over eastern SAF, may produce major economic and human life losses.

The present study considers the 1999–2010 period in which are available data from all 11 S2S project models, and it concentrates on DJF season, during which the monsoon highest rainfall occurs in most SAF, and during which the influence of global variability modes such as the MJO, ENSO, among others, are stronger (Mason and Jury 1997; Zaitchik 2017). Such an assessment provides an opportunity for identifying the strengths and weaknesses of each S2S

project model, which can be improved in their future versions. In Section 2, the models outputs and verification data, along with the methodology used to assess the quality of the forecasts are outlined. The results are presented and discussed in Section 3. Finally, the summary and concluding remarks are provided in Section 4.

2 Data and methods

2.1 Subseasonal to seasonal (S2S) project database

This study is based on the retrospective forecasts (also called reforecasts/hindcasts) retrieved from one of the S2S project database web-mirrors (https://apps.ecmwf.int/datasets/data/s2s/levtype=sfc/type=cf/). The host centers of these models include the Australian Bureau of Meteorology (BoM), the China Meteorological Administration (CMA), the Institute of Atmospheric Sciences and Climate of the National Research Council of Italy (CNR–ISAC), the Centre National de Recherches Météorologiques (CNRM) of Météo-France, the Environment and Climate Change Canada (ECCC), the European Centre for Medium-Range Weather Forecasts (ECMWF), the Hydrometeorological Centre of Russia (HMCR), the Japan Meteorological Agency (JMA), the Korea Meteorological Administration (KMA), the National Centers for Environmental Prediction (NCEP), and the United Kingdom's Met Office (UKMO).

Since the S2S database is a data of "opportunity," which means that the forecasts have not been produced specifically for the S2S project following an agreed-upon protocol as in Coupled Model Intercomparison Project (CMIP), the models of these centers have different prediction time range, spatial resolution, ensemble size, hindcast frequency and period (Vitart et al. 2017). Some models have the atmospheric component coupled to an ocean and active sea-ice model, while others use persisted SSTs and sea ice. The reforecasts of these models consist of one control run (using a single non-perturbed initial condition) and a number of perturbed members produced for sampling uncertainty in the initial conditions. Some hindcasts have been or are produced with a fixed model version (e.g., NCEP), whilst others with an on the fly model version (e.g., ECMWF) produce reforecasts with the most up to date model version at the time of forecast issuance. Due to the different reforecast frequencies, the hindcasts start dates are not identical in most models (Jie et al. 2017). For instance, the ECMWF is initialized twice weekly from January 3; NCEP and CMA daily from January 1; BoM and CNR-ISAC every five days from January 1; HMCR and ECCC weekly from January 3; CNRM weekly from January 1; KMA and UKMO every eight daily from January 1; JMA three times a month from January 10. Despite these differences, there are enough commonalities between these models to make intercomparisons or multimodel combinations possible. For instance, almost all of the S2S models produce real-time ensemble forecasts every Thursday and have reforecasts covering the common period (1999–2010). Thus, it is possible to create a multimodel combination of these models every Thursday, calibrated using their common period (Vitart et al. 2017). It is worth mentioning here that for those models with on the fly production cycles (version), the present study considers those hindcasts produced by the models version used only from June 2018 to June 2019, except the UKMO, for which were considered the hindcasts produced by the models version used up to April 1, 2019, the date after which the UKMO model migrated to newer version. For fuller details on each S2S project model characteristics, the readers are referred to either table 1 or S2S official webpage (https://confluence.ecmwf.int/display/S2S/Description or Vitart et al. (2017).

The variables analyzed in this study include daily values of precipitation ($\mathrm{mm\,day^{-1}}$), outgoing long-wave radiation (OLR, $\mathrm{W\,m^{-1}}$) used often as a proxy for atmospheric tropical heating (convection), zonal (U, $\mathrm{m\,s^{-1}}$) and meridional (V, $\mathrm{m\,s^{-1}}$) wind components at both 850- and 200-hPa levels. The KMA is the one of S2S model which at the moment of describing the results for this paper did not provide OLR data, therefore, for this model we did not perform MJO impacts assessment. Furthermore, in composite analysis (sections 2.5 and 3.1), we used for this model

rainfall data instead of OLR. The stream function (PSI, $m^2 s^{-1}$), which is computed from both U and V is also considered here for assessment of the global rotational circulation response to anomalous heat sources in the atmosphere. Here we display only the zonally asymmetric part of PSI (PSIZA, $m^2 s^{-1}$), which is obtained by removing the zonal mean (latitudinally averaged). PSIZA better reveals the wave-like structures in propagating Rossby waves (Hsu and Lin 1992; Held et al. 2002). The PSIZA considered here is that at 200 hPa (PSIZA200), the level in which the wave-like patterns are more clear and intense.

The analysis for each variable is performed with the ensemble mean, calculated from all hindcast perturbed members including the control run. It is worth mentioning here that the terms ensemble mean and forecast are interchangeable in this study.

Since the subseasonal time range is beyond deterministic weather prediction, here the weekly time frame that adequately removes part of the weather noise (Li and Robertson 2015) is considered. To this end, the forecasts issued on day d with lead times d+1–d+7, d+8–d+14, d+15–d+21, and d+22–d+28 are averaged in weekly means named respectively week 1, week 2, week 3, and week 4 leads, respectively. Each of these means is placed in the central day of the target week, forming series of week 1, week 2, week 3, and week 4 of forecasts with different lead times. As a result, for each lead time, the value of each day in each year over the study period is obtained from weekly means as described. Similar weekly means have been used in studies by Li and Robertson (2015), Marshall and Hendon (2015), Liang and Lin (2018), and de Andrade et al. (2019).

At a given lead, the weekly anomalies relative to their respective model climatology (calculated over the period 1999–2010) have been computed, and then included in the analysis if the dates pertaining to a given lead occur within DJF season. The running weekly model climatology has been smoothed with a 31-day moving average, to avoid spurious variance due to short period (1999–2010).

2.2 Verification data

To validate the models' rainfall, the 0.5° grid resolution Climate Prediction Center (CPC) unified gauge-based precipitation dataset (Chen et al. 2008) is used due to the unavailability of Mozambique gauge data after 2005 to the authors. This dataset is a blended product, composed of daily summary files from the Global Telecommunication System, and the CPC unified daily station data across the globe. The use of CPC among all other alternative gridded datasets is due to the fact that it shows a relatively good correspondence with Mozambique gauge precipitation (SG20). Furthermore, there was a need to make the S2S analysis for a large sample (1999–2010), rather than a small one (1999–2005), and hence, increase the reliability of the study.

For verification of atmospheric circulation of each model, wind components (U and V at both 850- and 200-hPa levels) derived from the NCEP/NCAR (National Center for Atmospheric Research) reanalysis version R1 (Kalnay et al. 1996) are used as in MH15. Sensitivity test for choosing a specific reanalysis has been performed here and the results have shown that it may only influence the magnitude of the performance metrics without changing the pattern of considered metrics, consistent with de Andrade et al. (2019). The OLR of each model is verified with 2.5° gridded daily averaged OLR from the National Oceanic and Atmospheric Administration (NOAA) polar-orbiting series of satellites (Liebmann and Smith 1996). For comparison purposes, all the observed including reanalysis data were regridded into a 1.5° S2S models common grid resolution through a bilinear interpolation method before using them in calculation of weekly (7-day) means. For comparison purposes, observed and reanalysis data series are computed as 7-day running means, so that these data can be compared to the reforecast data, in which, as already explained, each day represents an average over 7 consecutive days within a selected lead time interval (series of week 1, week 2, week 3, week 4

reforecasts). For these weekly means, we also created weekly anomalies relative to their climatology calculated for the 1999–2010 period and smoothed with a 31-day moving average, so as to be compatible with the models anomalies.

2.3 Definition of monsoon indices

As mentioned in Section 1, the analysis in this paper follows similar methodology used by MH15, who applied monsoon indices to evaluate the models prediction performance. These indices are generally calculated over the monsoon core region to help characterizing, monitoring, and predicting in an easier way the broad-scale monsoon rainfall variability and its associated circulation. To this end, SG20 have defined over SAF one index for rainfall (hereafter referred to as monsoon precipitation index, MPI) within the box (20°S–13.5°S, 32.5°E–38°E), and several monsoon circulation indices to complement the description captured by MPI or even to replace it, since the models show more skill in predicting circulation than precipitation (MH15). Among the circulation indices defined in SG20, we decided here to assess the performance of the models in simulating the one that is more associated with variations in monsoon circulation over the study region. This is the low-level zonal westerly wind index (ZWWI) defined over the box (7.5°S–14°S, 19.5°E–36.5°E). In SG20, both the MPI and ZWWI are calculated separately as area averaged standardized daily anomalies over the boxes just mentioned. Here the same indices are computed for both observations and model data. Since here the raw data are weekly means instead of daily means used in SG20, the indices are computed as area averaged standardized weekly anomalies. Although we use the weekly means, the same threshold of +(–) 0.7 standard deviation used in SG20 is considered in this study to define monsoon active (break) episodes. The mean standard deviation of observed daily MPI and ZWWI for DJF season over the period 1999–2010 is, respectively, 6.11 $\mathrm{mm\,d^{-1}}$ and 2.23 $\mathrm{m\,s^{-1}}$.

2.4 MJO index definition

To describe the MJO signal in terms of the strength (amplitude) and location (phase) of the convective center of action, the Real-time Multivariate MJO (RMM) index of Wheeler and Hendon (2004; hereafter referred to as WH04) is used. This index is defined using the first (RMM1) and second (RMM2) leading modes of the combined empirical orthogonal functions (EOFs) of weekly latitudinally-averaged (15°N–15°S) OLR, U850 and U200 anomalies after the removal of seasonal cycle and long-term variability of each field and normalization by its own individual zonal averaged standard deviation. The MJO is identified in its active state whenever the RMM index amplitude ($A = \sqrt{\mathrm{RMM1}^2 + \mathrm{RMM2}^2}$) is larger than 1. The eight phases of the MJO cycle are defined, as in WH04, according to the phase angle ($\theta = \tan^{-1}[\frac{\mathrm{RMM2}}{\mathrm{RMM1}}]$). This is performed for both observed data and models reforecasts. The RMM indices for the hindcast ensemble mean data series for each lead time (Wweek 1, week 2, week 3, week 4 data series), are computed by projecting the predicted weekly near-equatorially averaged anomalies of combined fields onto the observed EOF pair. The above procedures are almost the same as in Lin et al. (2008), except that here the OLR as in WH04 is used instead of rainfall to represent the tropical convection. The other difference is that here we use weekly anomalies instead of daily, as the analysis in the present study is in the weekly time frame.

2.5 Forecast assessment metrics

A variety of statistical verification metrics exists to evaluate the quality of a forecast. Two are used in this paper. One is the Pearson correlation coefficient (PCC) which measures the strength of the linear relationship between observed and predicted anomalies. Its significance is assessed using the Student's t test, in which the underlying null hypothesis is that the PCC between the observed and predicted anomalies is null.

Although this index assesses the synchrony between the variation of observed and predicted values, it gives no indication about the difference between observed and predicted values. Therefore, a second metric, the root-mean-squared error (RMSE) has been also used. Since the accuracy of models is verified for variables with different units (e.g., rainfall and wind), the normalized RMSE (NRMSE) that is scale-free is used. It is expressed in terms of the observed standard deviation.

The above hindcast quality measures were computed for all lead times analyzed, and applied separately to each grid point or selected area (in case of monsoon indices), considering weekly means whose midweek target date occurs during DJF season over the study period (1999–2010).

To understand the circulation anomalies associated with active (break) phases, defined as days in which the MPI weekly mean values are greater (less) than +(–) 0.7 standard deviation, an anomaly composite has been computed. To assess the significance of composited anomalies, the Student's t test is used with null hypothesis that there is no difference either between composited anomalies for positive (negative) phases and neutral ones or between composited anomalies for positive phases and negative ones.

In all analyses, the effective sample size has been estimated by considering the autocorrelation properties of time series (Wilks 2011).

3 Results

3.1 Selection of the best models for SAF monsoon prediction

A first idea about the performance of the S2S models in predicting summer precipitation over SAF is available in Figs. 1 and 2. Figure 1 shows the PCC between observed and predicted weekly rainfall anomalies (calculated without leaving any year out from the sample) over each SAF grid point for four different weekly lead times, while Fig. 2 shows results for NRMSE.

Relatively high PCC values result for week 1 and, as expected, they decrease as lead time increases. The region that exhibits more consistently a significant positive signal across the models from week 3 on is the equatorial eastern region. This signal is more evident after week 2, when the weather prediction limit is reached, and is possibly associated with either MJO or SST over tropical Indian Ocean. NRMSE in Fig. 2 shows generally higher values in northwest SAF, where the PCC displays the lowest values. In this region the two used metrics generally show consistent results for the performance. However, this is not always true, since sometimes high NRMSE follow high PCC pattern, as, for instance in HCMR and UKMO models over southwest SAF (Fig. 2), making it difficult to choose the best models in SAF.

In order to limit the number of models used in the SAF monsoon prediction, the evaluation is restricted to the performance in simulating the monsoon precipitation in the region of SAF most affected by the monsoon. This precipitation is represented by a Monsoon Precipitation Index (MPI) defined in SG20 as the standardized precipitation anomaly in the region delimited in purple over Fig. 3a. The SAF monsoon region is therefore defined here as the grid points in Fig. 3a whose precipitation is correlated with MPI with confidence level ≥ 90%. The result of this definition agrees with the region where the SAF monsoon precipitation is highest, as shown in SG20. Therefore, the selected models should meet the following criteria: (1) highest (lowest) average value of PCC (NRMSE) over the SAF monsoon

region, between observed and predicted precipitation (Figs. 3b, 3c); (2) highest (lowest) values of PCC (NRMSE) between observed and predicted MPI and ZWWI (Figs. 3f, 3g); (3) good reproduction of the correlation pattern between the observed MPI and precipitation over all SAF grid points (cf. Fig. 4 and Fig.3a).

All these criteria are evaluated for each lead time. Some of these criteria have objective evaluation, others more qualitative assessment. Each model was assigned order numbers regarding its classification in meeting each criterion. The sum of all these numbers for each model classifies the models: the lower the sum, the better the model in reproducing the monsoon precipitation in SAF. The first 6 models selected by criterion (1) are, regarding PCC, ECMWF, UKMO, JMA, KMA, NCEP, and ECCC (Fig. 3b), whereas with respect to NRMSE, are ECMWF, HMCR, CNRM, BoM, UKMO, JMA (Fig. 3c).

The analysis according to criterion (2) regarding PCC between observed and predicted MPI, indicates as first 6 models ECMWF, UKMO, JMA, KMA, CNRM, NCEP (Fig. 3d), while regarding NRMSE between observed and predicted MPI they are ECMWF, UKMO, JMA, KMA, ISAC, and CNRM (Fig. 3e). Still according to criterion (2), but now regarding PCC between observed and predicted ZWWI, the 6 first models are ECMWF, CNRM, JMA, NCEP, UKMO, and KMA (Fig. 3f), while regarding NRMSE between observed and predicted ZWWI they are ECMWF, CNRM, JMA, NCEP, UKMO, and ECCC (Fig. 3g)

Finally, the analysis according to criterion (3) requires the models to reproduce fairly well the observed pattern of relationship between MPI and rainfall over all SAF grid points (Fig. 3a). Results of PCC between observed MPI and predicted rainfall anomalies over all SAF grid points as a function of lead time are shown in Fig. 4. Comparison between Fig. 4 and Fig. 3a indicates ECMWF, CNRM, JMA, KMA, NCEP, and UKMO as the first six best models. It is worth mentioning here that in all three criteria adopted here, the selected models are listed according to the degree of their performance (e.g., best, god, normal, below normal, etc), ranked in descending order.

Analysis of Fig. 3 shows that for most of the models the PCC between observed and predicted MPI is larger than 0.5 in week 1, falling below 0.5 after this lead time (Fig. 3d). On the other hand, the PCC between observed and predicted ZWWI (Fig. 3f) appears larger than 0.5 up to week 2 for most models (and near 0.5 up to week 3 for ECMWF model). The NRMSE between observed and predicted MPI is below 1 in week 1 for most of the models, but exceeds this value after this lead time for all models except ECMWF, which stays below this value even in week 2 (Fig. 3e). On the other hand, the NRMSE between observed and predicted ZWWI (Fig. 3g) for almost all the models stays below 1 till week 2 (and near 1 up to week 3 for ECMWF model). Higher performance in predicting ZWWI is expected since rainfall is inherently noisier and more difficult to predict than large-scale circulation (MH15).

Summarizing the results of all three criteria for models selection, the first six best models are ECMWF, JMA, UKMO, CNRM, KMA, and NCEP, and these are retained for further analysis in the following sections. Interestingly, the ECMWF is the one that consistently appears as the top scoring model in all criteria consistent with previous studies (e.g., de Andrade et al. 2019). This is probably associated with its atmospheric component high horizontal resolution (15–32 km) that is the highest among all the S2S models.

3.2 Monsoon prediction and its modulation by MJO

The correlation assessment for predicting the weekly mean monsoon precipitation index (MPI) and U850 index (ZWWI) (described in section 2.3 and shown in Figs. 3d,f) is displayed in Fig. 5 for lead times out to 4 weeks, using the ensemble mean from all forecasts (green bars, the same shown in Figs. 3d,f), and also for forecasts initialized only on monsoon active days (red bars) and forecasts initialized only on monsoon break days (blue bars).

For stratification of forecasts into groups of ones initialized only on active days and others initialized only on break days, we have additionally computed the MPI using observed daily rainfall means instead of weekly ones as described in section 2.3. Then, for each weekly lead we separate lists of forecasts initialized only on monsoon break (active) days all weekly MPI values whose forecasts have been initialized on days in which the computed daily MPI is smaller (larger) than – (+) 0.7 daily standard deviation. The same stratification has been applied for ZWWI based also on daily MPI. Since the correlation using the ensemble mean from all forecasts for both MPI and ZWWI has been discussed in section 3.1 (Figs. 3d,f), here we discuss only the correlation for stratified forecasts.

Analysis of Fig. 5 suggests that there is an apparent consistent prediction skill improvement for both indices (MPI and ZWWI) in week 2 when the forecasts are initialized on monsoon active days and in week 3 when the forecasts are initialized on monsoon break days. This better performance of forecasts initialized during break periods in week 3 could be associated to the fact that this week could coincide with an active monsoon phase produced after half MJO cycle since the initialization on a break monsoon phase.

As the MJO is considered the primary source for subseasonal predictability (Neena et al. 2014), we analyze further the modulation of monsoon active and break episodes by this important intraseasonal mode.

To analyze this modulation, we firstly compute the proportion of days in each phase of MJO and in its neutral one with respect to the total days in the sample to get an idea of the most frequent (rare) MJO phases as the frequency and extension of specific MJO phase may strongly impact the number of monsoon active (break) days in a given phase. The results for observed data over the S2S common period (1999–2010) (Fig. 6a) show that during the 1999–2010 period the MJO phase 2 followed by phases 3, 4 and 6 appeared to occur more frequently, while phases 1 and 8, seemed to occur more rarely. It is worth mentioning that the MJO is thought to impact regional rainfall by increasing (decreasing) it when it is in its phases 8-1-2 (5-6-7) (Pohl et al. 2007, 2009; Macambaco 2016). However, this impact is not spatially homogeneous over SAF (Pohl et al. 2009). This is particularly true for the MPI region, over which the rainfall anomalies seem to be modulated mostly by MJO phase 1 convective activity possibly associated with teleconnections between South America (SA) and SAF subcontinent (Grimm and Reason 2015; Macambaco 2016; Grimm 2019; Silvério and Grimm 2020).

Following the MH15 methodology we assess the MJO influence on observed monsoon rainfall by calculating the proportion of monsoon active (break) days in each MJO phase and in neutral one with respect to the total monsoon active (break) days in the sample. The results for the monsoon active days are shown in Fig. 6b, which indicates the occurrence of higher number of monsoon active days in phase 2 followed by phase 4 of MJO. While the reason of occurrence of great number of monsoon active days in MJO phase 4 is likely associated with tropical-temperate troughs (TTT), the SAF main synoptic summer rain-producing system (Harrison 1984; Vigaud et al. 2012), which equally likely occur during any MJO phase (Pohl et al. 2009), the reason for higher proportion of monsoon active days in MJO phase 2 is likely associated with the fact that this phase occurs most frequently, as shown in Fig. 6a. This demonstrates that the number of monsoon active (break) days in each phase of MJO may depend on the number of days in which a specific MJO phase occurs, and not necessarily on the preference of monsoon active (break) days for a given MJO phase (Grimm et al. 2020; manuscript under compillation). To overcome this issue, we additionally applied a methodology proposed by Grimm et al. (2020) who assess the MJO influence on observed monsoon rainfall by calculating the proportion of active (break) monsoon days in a given MJO phase with respect to the number of days in that phase. The results for observed monsoon active days are shown in Fig. 6c, which shows that the Grimm's method adequately captures the expected MJO phase 1 influence on rainfall over the MPI region as reported before. It is worth pointing out that 30% of the monsoon active days occurs during neutral MJO period (letter "N", Fig. 6b), suggesting that non-MJO forcing also strongly impacts on rainfall over MPI region.

Figure 7 show the proportion of days in each phase of MJO and in its neutral one with respect to the total days in the sample for 5 retained models (see section 3.1) except KMA, which at the moment of obtaining the results for this paper did not provide the OLR data, one of variables used for extraction of MJO signal. Comparison of Fig. 7 with Fig. 6a suggests that most models fairly well depict the pattern shown in Fig. 6a out to week 3 although sometimes the highest proportion of days in the MJO phase 2 is moved to another phase. NCEP is one model that fairly well depicts the observed proportion of days in MJO phase 2 out to week 4 lead.

Figure 8 displays the proportion of monsoon active days in each MJO phase and in neutral one with respect to the total monsoon active days in the sample for the 5 models shown in Fig. 7. Consistent with Fig. 6b, most models, with exception of JMA, fairly well depict the observed higher proportion in MJO phase 2 out to week 2 lead. Again, NCEP outscores other models as it fairly well depicts the observed higher proportion in MJO phase 2 out to week 4 lead. It fails, however, in showing the second highest proportion in phase 4.

Finally, in Fig. 9, as in Fig. 6c, we show the proportion of active monsoon days in each MJO phase with respect to the number of days in each phase. For this type of analysis, all models fail reproducing the observed proportion presented in Fig. 6c. This can be attributed to the models' deficiencies in representing teleconnections, the most important mechanism by which the MJO impact modulates SA influences on SAF precipitation.

3.3 The space-time evolution of rainfall and circulation anomalies associated with MPI

Figure 10 shows the differences between anomaly composites for the monsoon active (positive) and break (negative) episodes using observed data and model reforecasts for week 1. Only the first (-0) and last (+0) days of active and break episodes are used, in order to show the evolution of these episodes (Fig. 10a and Fig. 10b) with OLR (shading) and PSIZA200 (contours) anomalies, from their beginning to their demise over the SAF monsoon region.

Analysis of Fig. 10a with observed data (first row) suggests that the rainfall anomalies development over SAF monsoon area is associated with a cloud band, consistent with the formation of TTT. This band of enhanced convection is followed by enhanced subsidence to the southwest, forming a familiar southwest–northeast oriented dipole pattern of suppressed and enhanced convection (Washington and Todd 1999; Silvério and Grimm, 2020), which seems to move north-eastward (Fig. 10b). The associated circulation anomalies, as represented by PSIZA200, are coherent with a TTT, being part of a wave train originating in subtropical South Pacific Ocean and which by moving into SAF seems to be modulated by convective anomalies over South America and the Atlantic Ocean, consistent with Grimm and Reason (2015) and Silvério and Grimm (2020). As the anomalous OLR southwest-northeast oriented dipole pattern moves northeastward, the precipitation starts decreasing in the MPI region. In the subsequent days (not shown), the dissipation of convection along with its associated circulation is observed.

Models that are able to simulate the described observed teleconnection patterns will have preference for operational forecast in the region, as they can adequately help SAF National Meteorological Services in predicting the occurrence of extreme weather events associated for example with anomalous convection likely associated with MJO convective activity over SA (Grimm and Reason 2015; Silvério and Grimm 2020). The next rows of Fig. 10 show the corresponding results obtained using the ensemble means of reforecasts for week 1 of each selected models (see section 3.1). We present the results for week 1 lead since for longer lead times the results get worse. Figure 10 shows the results for five of the six selected models (CNRM, ECMWF, JMA, KMA, and UKMO), while the NCEP model will undergo a more detailed analysis regarding the evolution of the active (break) monsoon periods. All the models tend to reproduce the observed OLR southwest-northeast oriented dipole pattern, while some of them also reproduce reasonably the

observed circulation anomalies associated with active monsoon periods (e.g., ECMWF, UKMO). In most models the anomalies of both convection and circulation tend to be stronger than those of observed results.

Figures 11 and 12 present differences between lead-lag composites for active and break monsoon days from day -4 with respect to the first day of the active period (-0) to day +4 after the last day of the active period. The results in Fig. 11 are for observations, while in Fig. 12 are for the week 1 reforecasts of NCEP model. The reason for creating composites from day -4 to day +4 for this model is due the fact that it fairly well reproduces the MJO influence (see section 3.2), and provides forecasts daily.

Analysis of Fig. 11 confirms the structure of eastward propagating wave trains. This wave train passing over South Atlantic seems to be modulated by convective activity extending from South Atlantic Convergence Zone (SACZ) to neighbouring Atlantic Ocean along northwest-southeast direction. Over SAF, the excited wave train interacts with SAF regional circulation, creating favourable conditions to enhance the monsoon circulation there (SG20). In the subsequent days (from day +0 to day +4, Fig. 11f-j), the convection moves and dissipates, and the circulation anomalies weaken changing to conditions favorable for supressed rainfall. The analysis of NCEP composites for week 1 lead (Fig. 12), suggests that the model simulates fairly well the observed pattern shown in Fig. 11, although it locates no OLR over SACZ and Atlantic Ocean which seems to be the reason for weaker wave train simulation by the model. This probably explains the slower tendency of the OLR anomalies dissipation over the SAF monsoon region in the model.

4 Summary and conclusions

The performance of global operational state-of-the-art S2S project models in simulating SAF monsoon subseasonal anomalies was evaluated. This unprecedented comparative analysis provides a unique opportunity for improving the current knowledge about the ability of these models in representing the weekly precipitation anomalies and their associated circulation over SAF, indicating possible shortcomings in the models. Two deterministic forecast quality metrics (linear correlation, and normalized root mean square error) are employed for verifying the hindcasts quality for different forecast lead times (weeks 1–4) during the austral summer (DJF) season over the S2S common period (1999–2010). All models showed higher performance in week 1, with rapid scores decrease in the following weeks, and maintaining meaningful signal mainly in the tropics (Figs. 1,2), which can be attributed to MJO or sea surface temperature over tropical Indian and equatorial eastern Pacific Oceans. Broad-scale weekly monsoon rainfall over SAF is predictable to about a week ahead (for correlation values exceeding 0.5), while its associated circulation is predictable to about 3 weeks lead time. This discrepancy in lead time suggests the potential for extending the useful prediction of monsoon rainfall to longer lead time if model errors associated with the prediction of the MJO and the local influence of the MJO in the monsoon could be alleviated (Marshall and Hendon 2015).

Since some of the S2S models simulate poorly the observed monsoon subseasonal variability, some criteria are applied to select some models for further analysis. According to these criteria (see section 3.1) the ECMWF, JMA, UKMO, CNRM, KMA, and NCEP (ranked in descending order) were selected as the best ones for subseasonal prediction of the SAF monsoon. Although most of the retained models fairly well reproduce the proportion of active monsoon days in each MJO phase and its modulation by MJO out to week 3 lead, not all reproduce the teleconnection patterns between South America and SAF, an important mechanism through which convective anomalies and MJO impacts over South America influence the SAF subcontinent. This is likely due to errors associated with model deficiencies in representing teleconnections (de Andrade et al. 2019). This produces deficiencies of the models in simulating regional or local responses to MJO impacts on rainfall.

The assessment of model performance provided here is a first step in extending the current forecast guidance to include probabilistic forecasts for the subseasonal timescale. The knowledge derived from this study can be used in the formation of a multimodel ensemble approach. The improved forecast capability would be of great benefit for agriculture and water resource management, upon which largely depend SAF economies.

References

Ardilouze C, Batté L, Déqué M (2017) Subseasonal-to-seasonal (S2S) forecasts with CNRM-CM: a case study on the July 2015 West-European heat wave. Adv Sci Res 14:115–121. doi: 10.5194/asr-14-115-2017

Baggett CF, Barnes EA, Maloney ED, Mundhenk BD (2017) Advancing atmospheric river forecasts into subseasonal-to-seasonal time scales. Geophys Res Lett 44:7528–7536. doi: 10.1002/2017GL074434

Bauer P, Thorpe A, Brunet G (2015) The quiet revolution of numerical weather prediction. Nature 525:47–55.

Bombardi RJ, Pegion K V., Kinter JL, et al (2017) Sub-seasonal Predictability of the Onset and Demise of the Rainy Season over Monsoonal Regions. Front Earth Sci 5:14. doi: 10.3389/feart.2017.00014

Chen M, Shi W, Xie P, et al (2008) Assessing objective techniques for gauge-based analyses of global daily precipitation. J Geophys Res 113:D04110. doi: 10.1029/2007JD009132

de Andrade FM, Coelho CAS, Cavalcanti IFA (2019) Global precipitation hindcast quality assessment of the Subseasonal to Seasonal (S2S) prediction project models. Clim Dyn 52:5451–5475.

Doblas-Reyes FJ, García-Serrano J, Lienert F, et al (2013) Seasonal climate predictability and forecasting: Status and prospects. Wiley Interdiscip Rev Clim Chang. doi: 10.1002/wcc.217

Grimm AM (2019) Madden–Julian Oscillation impacts on South American summer monsoon season: precipitation anomalies, extreme events, teleconnections, and role in the MJO cycle. Clim Dyn 1–26.

Grimm AM, Hakoyama LR, Scheibe LA. (2020) Subseasonal prediction of South American monsoon rainfall: active and break episodes, and the contribution of the MJO. Clim Dyn

Grimm AM, Reason CJC (2015) Intraseasonal Teleconnections between South America and South Africa. J Clim 28:9489–9497. doi: 10.1175/JCLI-D-15-0116.1

Harrison MSJ (1984) A generalized classification of South African summer rain-bearing synoptic systems. J Climatol 4:547–560. doi: 10.1002/joc.3370040510

Held IM, Ting M, Wang H (2002) Northern Winter Stationary Waves: Theory and Modeling. J Clim 15:2125–2144.

Hirata FE, Grimm AM (2018) Extended-range prediction of South Atlantic convergence zone rainfall with calibrated CFSv2 reforecast. Clim Dyn 50:3699–3710. doi: 10.1007/s00382-017-3836-1

Hsu H-H, Lin S-H (1992) Global Teleconnections in the 250-mb Streamfunction Field during the Northern Hemisphere Winter. Mon Weather Rev 120:1169–1190. doi: 10.1175/1520-0493(1992)120<1169:GTITMS>2.0.CO;2

Jie W, Vitart F, Wu T, Liu X (2017) Simulations of the Asian summer monsoon in the sub-seasonal to seasonal

prediction project (S2S) database. Q J R Meteorol Soc 143:2282–2295. doi: 10.1002/qj.3085

Kalnay E, Kanamitsu M, Kistler R, et al (1996) The NCEP/NCAR 40-Year Reanalysis Project. Bull Am Meteorol Soc 77:437–471. doi: 10.1175/1520-0477(1996)077<0437:TNYRP>2.0.CO;2

Lee C-Y, Camargo SJ, Vitart F, et al (2018) Subseasonal Tropical Cyclone Genesis Prediction and MJO in the S2S Dataset. Weather Forecast 33:967–988. doi: 10.1175/WAF-D-17-0165.1

Lee S-S, Moon J-Y, Wang B, Kim H-J (2017) Subseasonal Prediction of Extreme Precipitation over Asia: Boreal Summer Intraseasonal Oscillation Perspective. J Clim 30:2849–2865. doi: 10.1175/JCLI-D-16-0206.1

Li S, Robertson AW (2015) Evaluation of Submonthly Precipitation Forecast Skill from Global Ensemble Prediction Systems. Mon Weather Rev 143:2871–2889. doi: 10.1175/MWR-D-14-00277.1

Liang P, Lin H (2018) Sub-seasonal prediction over East Asia during boreal summer using the ECCC monthly forecasting system. Clim Dyn 50:1007–1022. doi: 10.1007/s00382-017-3658-1

Liebmann B, Smith CA (1996) Description of a Complete (Interpolated) Outgoing Longwave Radiation Dataset. Bull. Am. Meteorol. Soc. 77:1275–1277

Lin H, Brunet G, Derome J (2008) Forecast Skill of the Madden–Julian Oscillation in Two Canadian Atmospheric Models. Mon Weather Rev 136:4130–4149. doi: 10.1175/2008MWR2459.1

Lin H, Mo R, Vitart F, Stan C (2019) Eastern Canada Flooding 2017 and its Subseasonal Predictions. Atmosphere-Ocean 57:195–207. doi: 10.1080/07055900.2018.1547679

Liu X, Wu T, Yang S, et al (2017) MJO prediction using the sub-seasonal to seasonal forecast model of Beijing Climate Center. Clim Dyn 48:3283–3307. doi: 10.1007/s00382-016-3264-7

Liu X, Yang S, Li J, et al (2015) Subseasonal Predictions of Regional Summer Monsoon Rainfall over Tropical Asian Oceans and Land. J Clim 28:9583–9605. doi: 10.1175/JCLI-D-14-00853.1

Lorenz EN (1963) Deterministic Nonperiodic Flow. J Atmos Sci 20:130–141.

Lorenz EN (1969) Atmospheric Predictability as Revealed by Naturally Occurring Analogues. J Atmos Sci 26:636–646.

Macambaco MP (2016) Climate variations in southeastern Africa (SEA) and their possible teleconnections with South America (SA). Master Thesis at Federal University of Parana

Madden RA, Julian PR (1971) Detection of a 40–50 Day Oscillation in the Zonal Wind in the Tropical Pacific. J Atmos Sci 28:702–708. doi: 10.1175/1520-0469(1971)028<0702:DOADOI>2.0.CO;2

Mariotti A, Ruti PM, Rixen M (2018) Progress in subseasonal to seasonal prediction through a joint weather and climate community effort. npj Clim Atmos Sci 1:4. doi: 10.1038/s41612-018-0014-z

Marshall AG, Hendon HH (2015) Subseasonal prediction of Australian summer monsoon anomalies. Geophys Res Lett 42:10,913-10,919. doi: 10.1002/2015GL067086

Mason SJ, Jury MR (1997) Climatic variability and change over southern Africa: a reflection on underlying processes. Prog Phys Geogr 21:23–50. doi: 10.1177/030913339702100103

National Research Council (2010) Assessment of Intraseasonal to Interannual Climate Prediction and Predictability. National Academies Press, Washington, D.C.

Neena JM, Lee JY, Waliser D, et al (2014) Predictability of the Madden–Julian Oscillation in the Intraseasonal Variability Hindcast Experiment (ISVHE). J Clim 27:4531–4543. doi: 10.1175/JCLI-D-13-00624.1

Olaniyan E, Adefisan EA, Oni F, et al (2018) Evaluation of the ECMWF Sub-seasonal to Seasonal Precipitation Forecasts during the Peak of West Africa Monsoon in Nigeria. Front Environ Sci 6:.

Osman M, Alvarez MS (2018) Subseasonal prediction of the heat wave of December 2013 in Southern South America by the POAMA and BCC-CPS models. Clim Dyn 50:67–81. doi: 10.1007/s00382-017-3582-4

Palmer TN, Anderson DLT (1994) The prospects for seasonal forecasting—A review paper. Q J R Meteorol Soc

120:755–793. doi: 10.1002/qj.49712051802

Pohl B, Fauchereau N, Richard Y, et al (2009) Interactions between synoptic, intraseasonal and interannual convective variability over Southern Africa. Clim Dyn 33:1033–1050. doi: 10.1007/s00382-008-0485-4

Pohl B, Richard Y, Fauchereau N, et al (2007) Influence of the Madden–Julian Oscillation on Southern African Summer Rainfall. J Clim 20:4227–4242. doi: 10.1175/JCLI4231.1

Reason CJ., Landman W, Tennant W (2006) Seasonal to Decadal Prediction of Southern African Climate and Its Links with Variability of the Atlantic Ocean. Bull Am Meteorol Soc 87:941–956. doi: 10.1175/BAMS-87-7-941

Robertson AW, Camargo SJ, Sobel A, et al (2018) Summary of workshop on sub-seasonal to seasonal predictability of extreme weather and climate. npj Clim Atmos Sci 1:20178. doi: 10.1038/s41612-017-0009-1

Shukla (1998) Predictability in the midst of chaos: A scientific basis for climate forecasting. Science 282:728–31

Silvério KC, Grimm AM (2020) Southern Africa monsoon: Intraseasonal variability and monsoon indices. Clim Dyn

Vigaud N, Pohl B, Crétat J (2012) Tropical-temperate interactions over southern Africa simulated by a regional climate model. Clim Dyn 39:2895–2916. doi: 10.1007/s00382-012-1314-3

Vigaud N, Robertson AW, Tippett MK (2017a) Multimodel Ensembling of Subseasonal Precipitation Forecasts over North America. Mon Weather Rev 145:3913–3928. doi: 10.1175/MWR-D-17-0092.1

Vigaud N, Robertson AW, Tippett MK, Acharya N (2017b) Subseasonal Predictability of Boreal Summer Monsoon Rainfall from Ensemble Forecasts. Front Environ Sci 5:67. doi: 10.3389/fenvs.2017.00067

Vitart F, Ardilouze C, Bonet A, et al (2017) The Subseasonal to Seasonal (S2S) Prediction Project Database. Bull Am Meteorol Soc 98:163–173. doi: 10.1175/BAMS-D-16-0017.1

Vitart F, Robertson AW (2018) The sub-seasonal to seasonal prediction project (S2S) and the prediction of extreme events. npj Clim Atmos Sci 1:3. doi: 10.1038/s41612-018-0013-0

Vitart F, Robertson AW, Anderson DLT (2012) Subseasonal to Seasonal Prediction Project : bridging the gap between weather and climate

Vitart F, Robertson AW, S2S Steering Group (2015) Sub-seasonal to seasonal prediction: Linking weather and climate. Seamless Prediction of the Earth System: From Minutes to Months. In: Brunet G, Jones S, Ruti PM (eds) Seamless Prediction of the Earth System: From minutes to months, WMO-1156. World Meteorological Organization (WMO), Geneva, Switzerland, pp 1–483

Vuillaume JF, Dorji S, Komolafe A, Herath S (2018) Sub-seasonal extreme rainfall prediction in the Kelani River basin of Sri Lanka by using self-organizing map classification. Nat Hazards 94:385–404.

Wang L, Robertson AW (2018) Week 3–4 predictability over the United States assessed from two operational ensemble prediction systems. Clim Dyn 1–15. doi: 10.1007/s00382-018-4484-9

Wang S, Anichowski A, Tippett MK, Sobel AH (2017) Seasonal Noise Versus Subseasonal Signal: Forecasts of California Precipitation During the Unusual Winters of 2015-2016 and 2016-2017. Geophys Res Lett 44:9513–9520. doi: 10.1002/2017GL075052

Washington R, Todd M (1999) Tropical-temperate links in southern African and Southwest Indian Ocean satellite-derived daily rainfall. Int J Climatol 19:1601–1616.

Wheeler MC, Hendon HH (2004) An All-Season Real-Time Multivariate MJO Index: Development of an Index for Monitoring and Prediction. Mon Weather Rev 132:1917–1932.

White CJ, Carlsen H, Robertson AW, et al (2017) Potential applications of subseasonal-to-seasonal (S2S) predictions. Meteorol Appl 24:315–325. doi: 10.1002/met.1654

Wilks DS (2011) Statistical methods in the atmospheric sciences, 3rd edn. Elsevier/Academic Press

Zaitchik BF (2017) Madden-Julian Oscillation impacts on tropical African precipitation. Atmos Res 184:88–102.

Table 1 The main features of the S2S state-of-the-art models hindcasts

S2S Model	Time range (days)	Spatial Resolution	Hindcast Frequency	Hindcast Ensemble size	Hindcast Period	Ocean Coupled	Sea-ice Coupled	Model version
BoM	0-62	T47, L17	6/month	33	1981-2013	Yes	No	2014-01-01
CMA	0-60	T106, L40	daily	4	1994-2014	Yes	Yes	2014-05-01
CNRM	0-61	T255, L91	4/month	15	1993-2014	Yes	Yes	2014-12-01
ECCC[a]	0-32	0.45° × 0.45°, L40	weekly	4	1998-2017	No	No	On the Fly
ECMWF[a]	0-46	Tco639/Tco319, L91	2/week	11	1999-2018	Yes	No	On the Fly
HMCR[a]	0-61	1.1° × 1.4°, L28	Weekly	10	1985-2010	No	No	On the Fly
ISAC	0-32	0.86° × 0.56°, L54	6/month	5	1981-2010	No	No	2017-06-08
JMA	0-33	TL479/TL319, L100	3/month	5	1981-2012	No	No	2017-01-31
KMA[a]	0-60	N216, L85	4/month	3	1991-2010	Yes	Yes	On the Fly
NCEP	0-44	T126, L64	daily	4	1999-2010	Yes	Yes	2011-03-01
UKMO[a]	0-60	N216, L85	4/month	7	1993-2016	Yes	Yes	On the Fly

[a] Hindcasts are produced on the fly (model version is not fixed). For this type of hindcasts, we consider in this study only those produced by the model version used during June 2018 to June 2019, except UKMO for which we considered only those of the model version used during June 2018 to April 1, 2019.
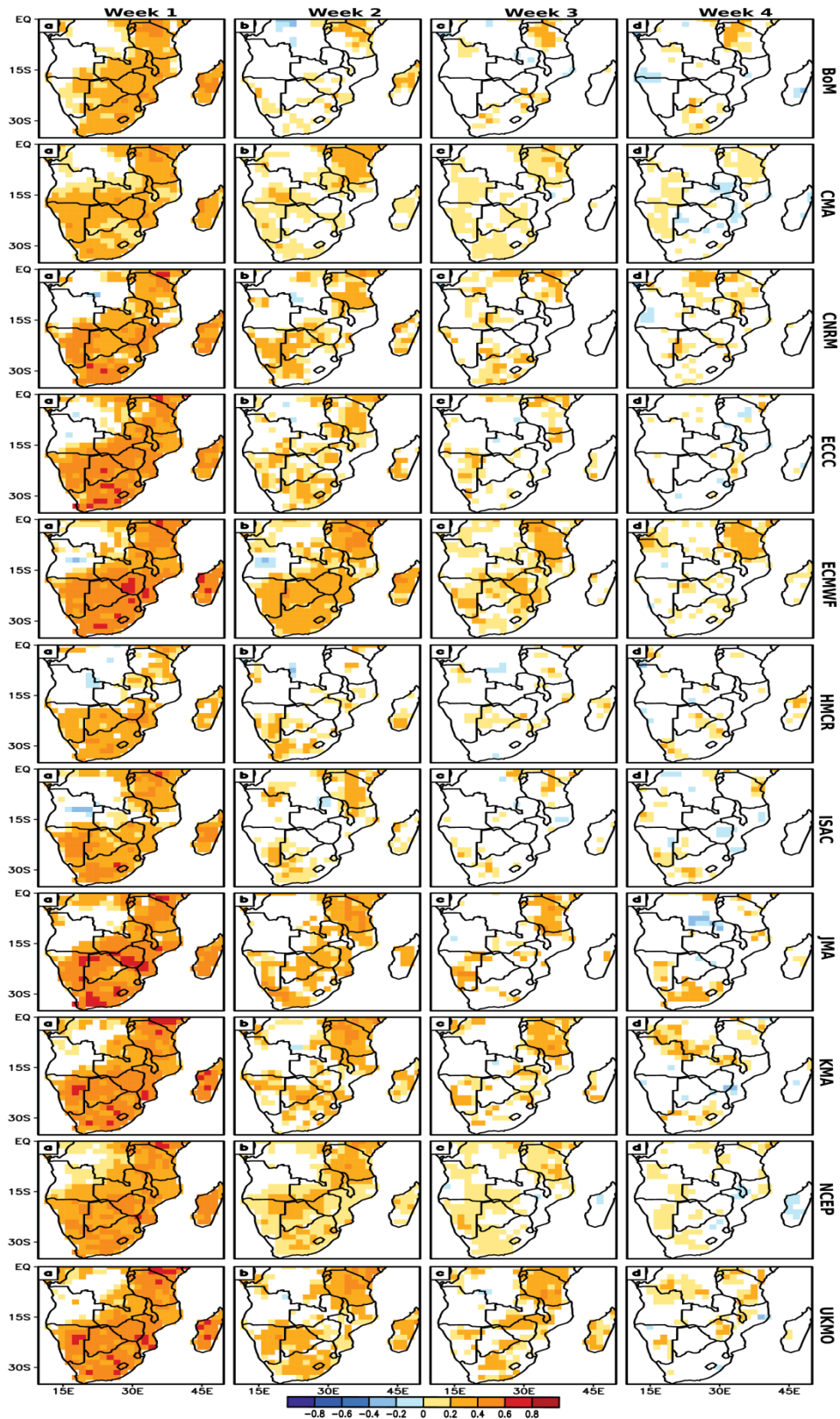
Fig. 1 Correlation between each S2S model (rows) weekly ensemble mean and observed (CPC) weekly precipitation anomalies as function of lead time for hindcasts initialized during December-January-February months over the 1999–2010 period. From left to right are: (a) week 1, (b) week 2, (c) week 3, and (d) week 4. The color bar in the bottom denotes the correlation coefficients. Only statistically significant values with confidence level better than 95 % according to Student's t test are represented
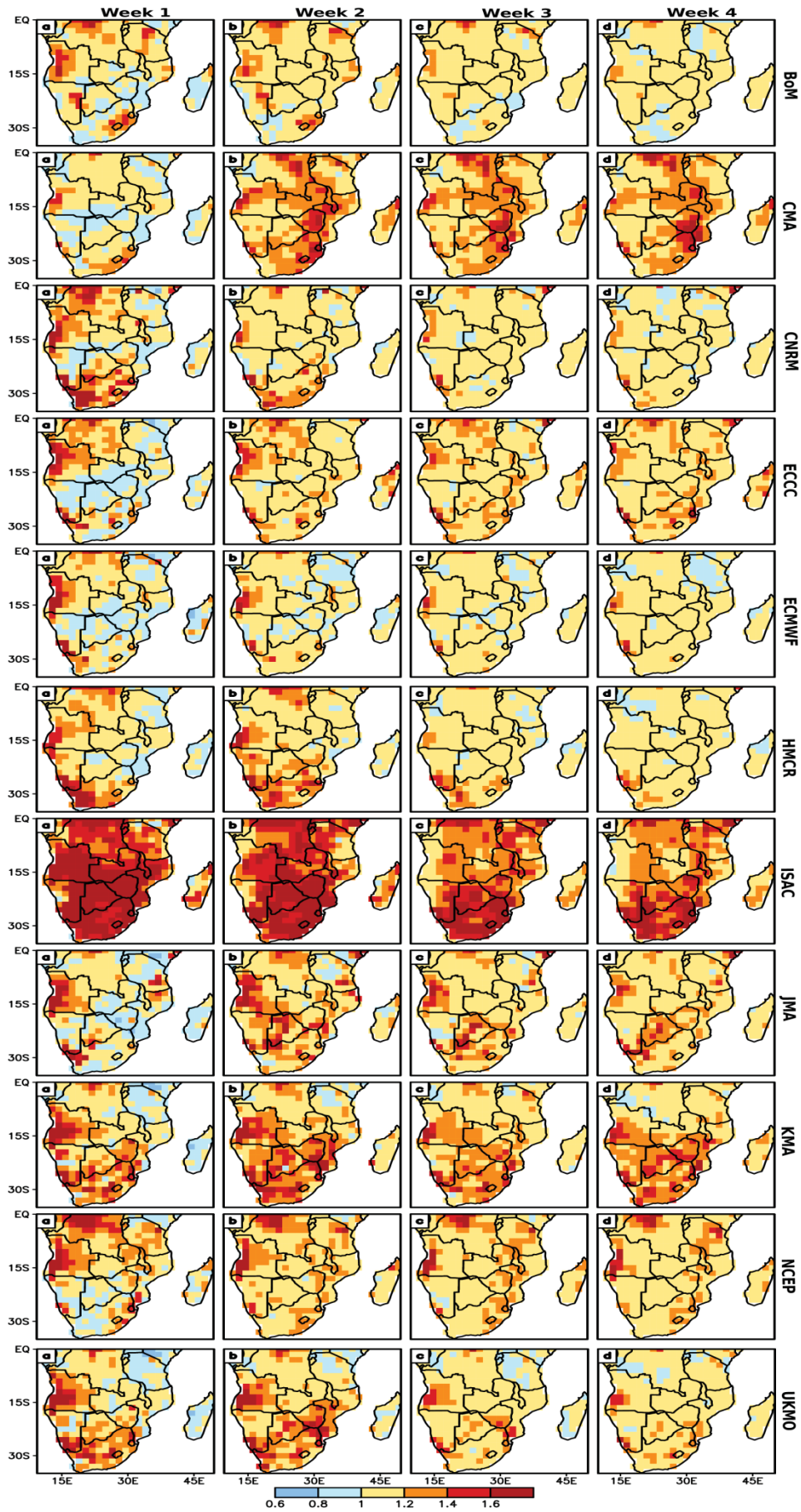
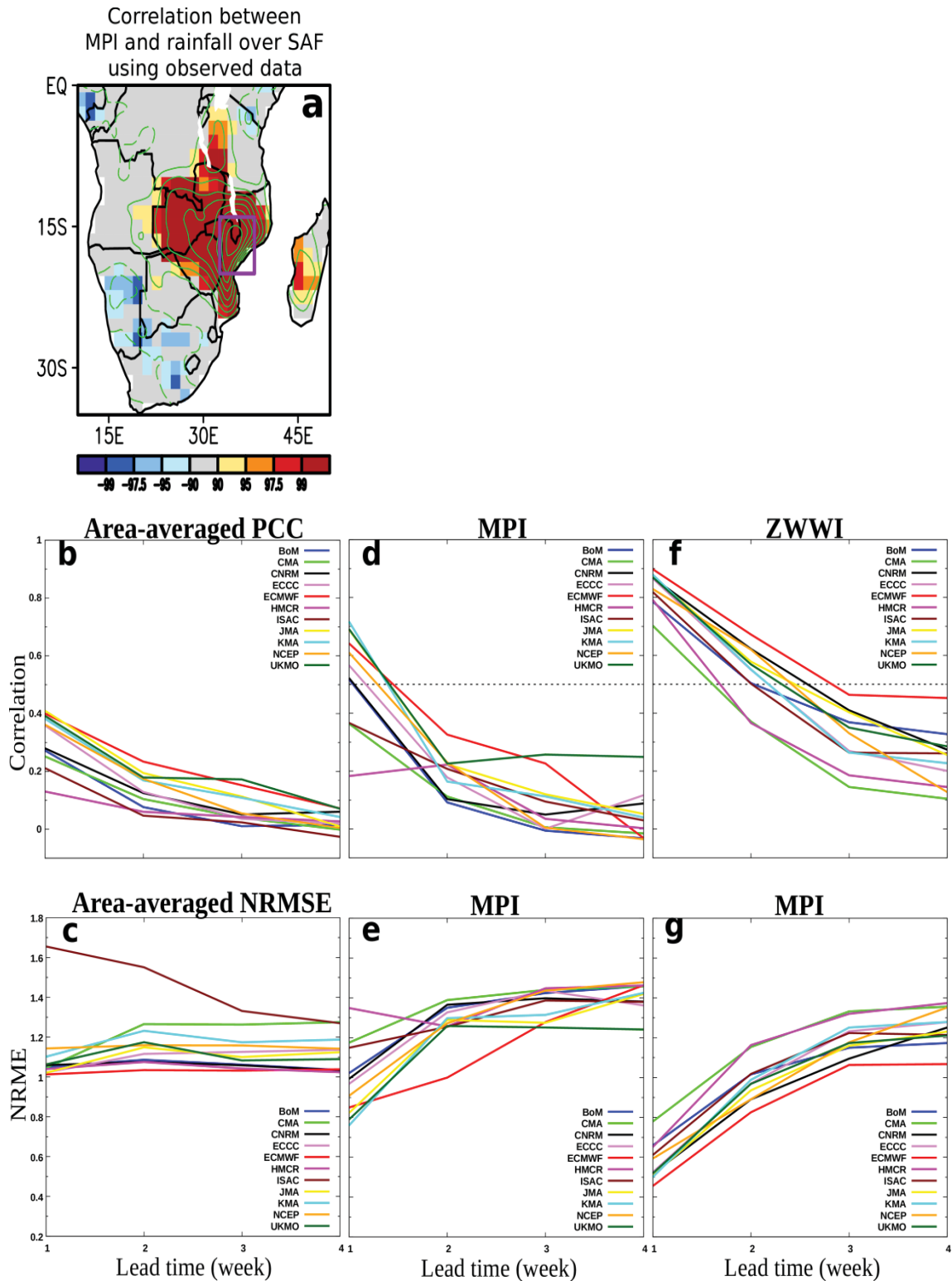Fig. 2 Similar to Fig. 1, but for normalized root mean square error (NRMSE)

Fig. 3 (a) Pearson correlation coefficient (PCC) between weekly MPI (within the purple rectangle) and weekly observed (CPC) rainfall anomalies in SAF grid points. Solid (dashed) contours denote positive (negative) PCC, with zero contour omitted and interval 0.1. The color bar in the bottom denotes the PCC confidence levels calculated according to Student's t test. (b) and (c) show, respectively, area-averaged PCC and NRMSE between observed and predicted weekly precipitation during DJF over the SAF monsoon region. (d) and (e) display, respectively, PCC and NRMSE between observed and predicted weekly MPI. (f) and (g) same as (d) and (e), but for ZWWI
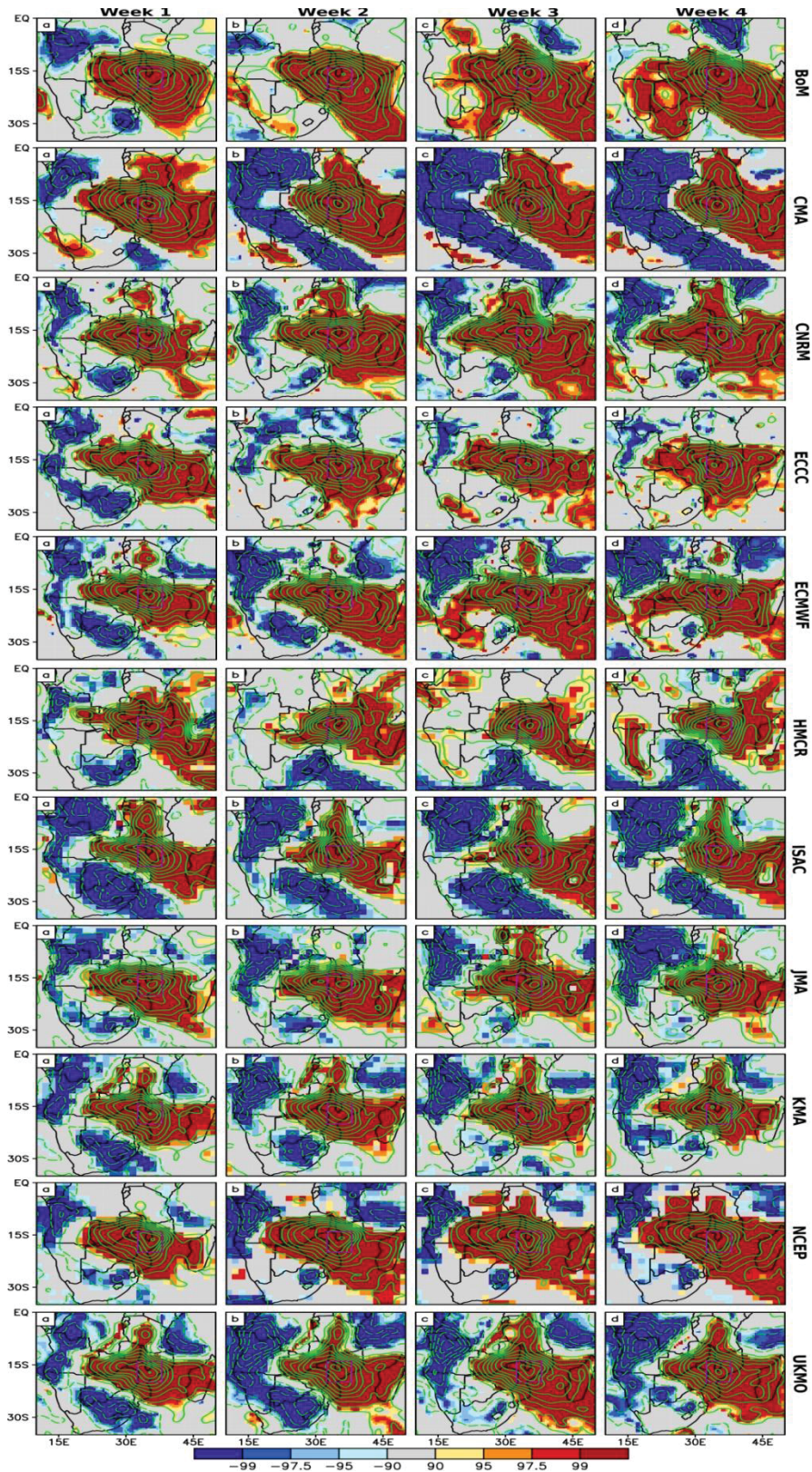
Fig. 4 Pearson correlation coefficient (PCC) between weekly observed MPI and weekly predicted rainfall anomalies over SAF grid points. From left to right are forecasts for: (a) week 1, (b) week 2, (c) week 3, and (d) week 4. Shading as represented by the color bar in the bottom denotes the PCC confidence levels calculated according to Student's t test. Solid (dashed) contours whose interval is 0.1 denote positive (negative) PCC with zero contour omitted.
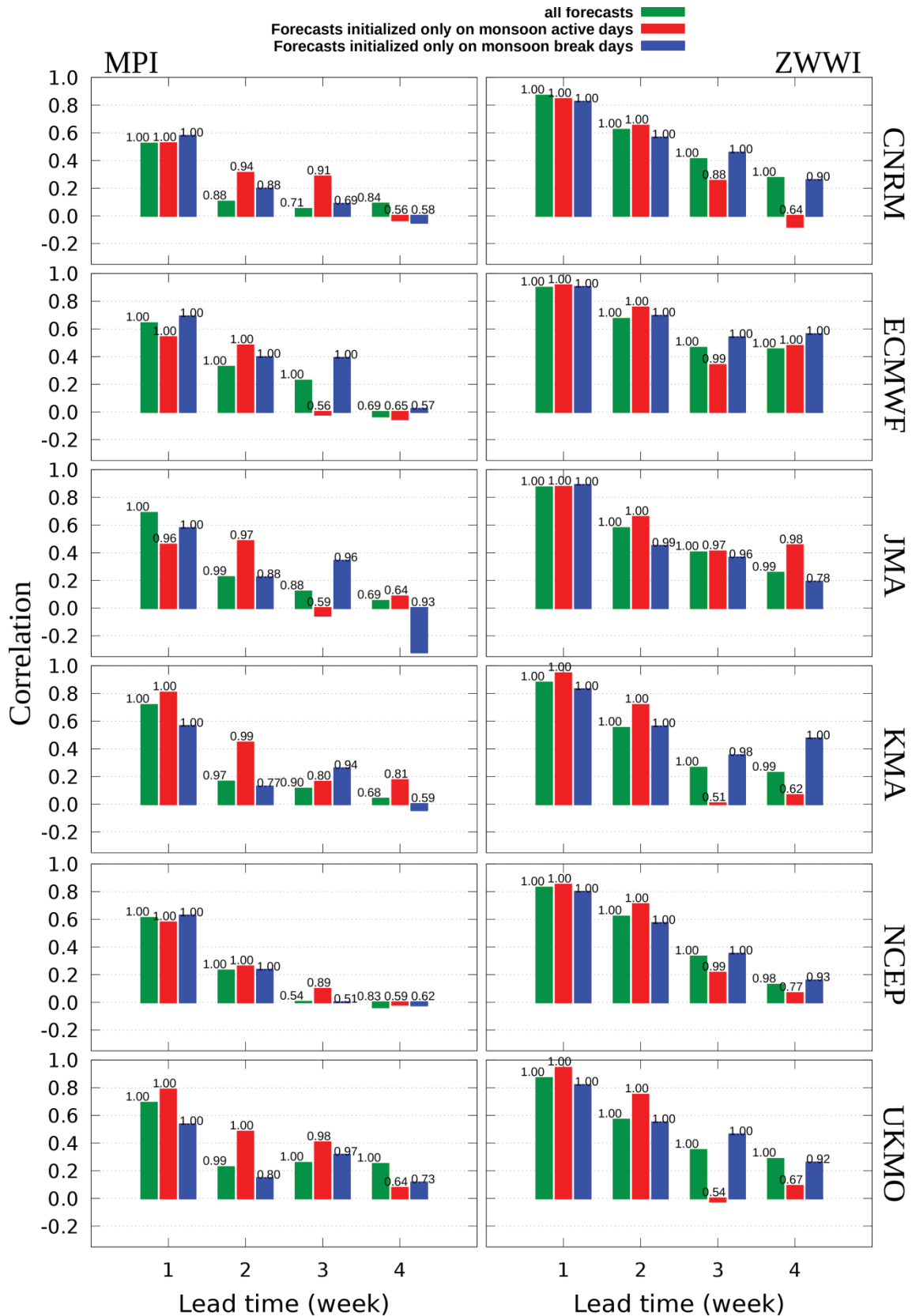
Fig. 5 Correlation assessment for predicting weekly mean monsoon rainfall (PMI, left) and monsoon U850 (ZWWI, right) indices for lead times out to 4 weeks, using the ensemble mean from all forecasts (green bars), forecasts initialized only on monsoon active days (red), and forecasts initialized only on monsoon break days (blue). Values above the bars represent the correlation confidence levels
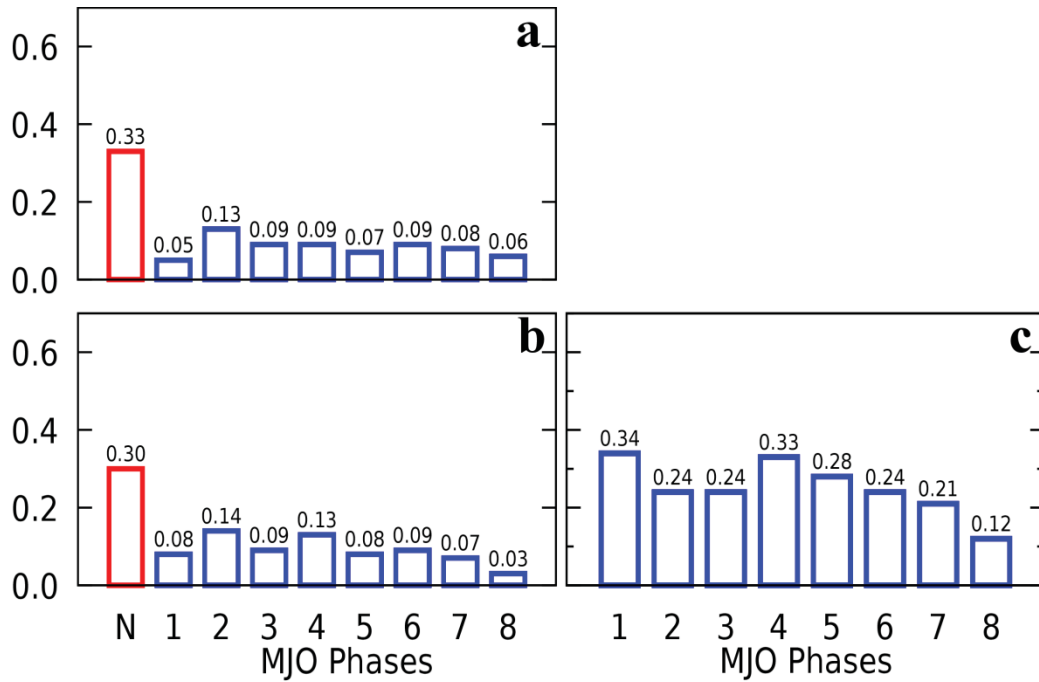
Fig. 6 (a) Proportion of days in each phase of MJO and in its neutral one with respect to the days in the sample. (b) Proportion of monsoon active days in each phase of MJO and neutral one with respect to the total monsoon active days in the sample. (c) Proportion of monsoon active days in a specific phase of MJO with respect to the days in that phase. Values above the bars denote the proportion. The letter "N" in (a) and (b) indicate proportion of days and monsoon active days in non MJO days, respectively. All proportions presented in this figure were obtained using observed data for 1999–2010
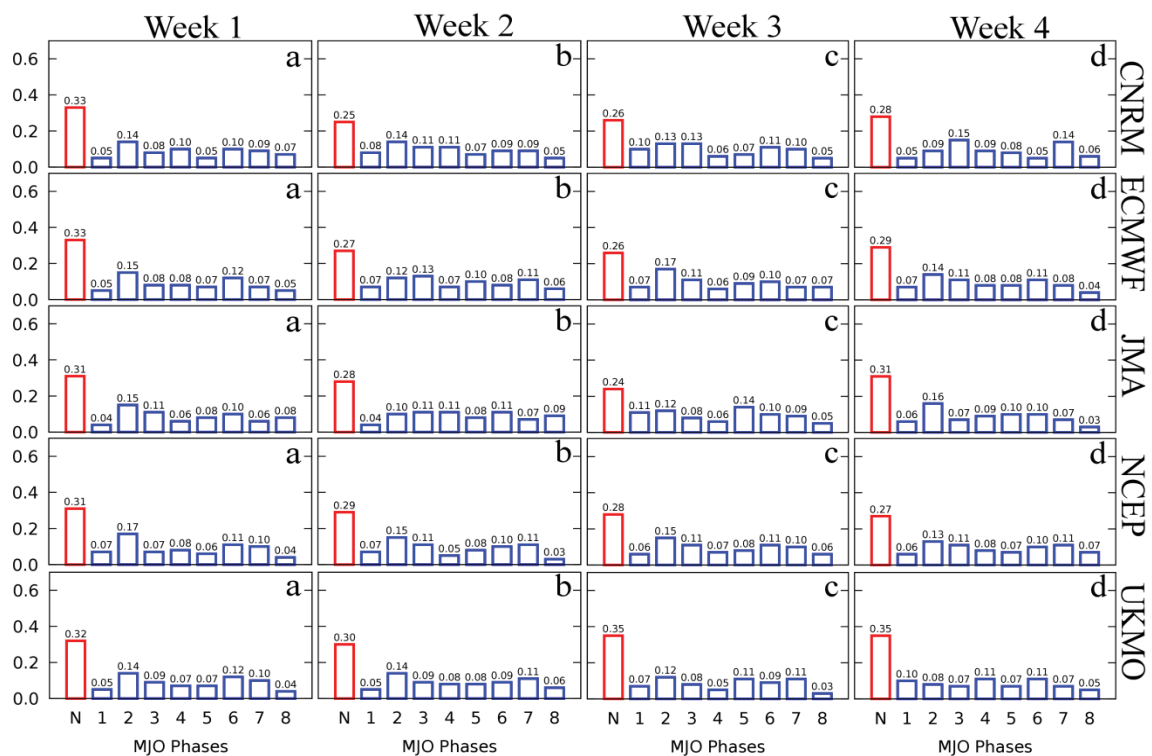

Fig. 7 Same as Fig. 6a, but for models. From left to right are: (a) week 1, (b) week 2, (c) week 3, and (d) week 4. The models are represented in each row

Fig. 8 Same as Fig. 6b, but for models. From left to right are: (a) week 1, (b) week 2, (c) week 3, and (d) week 4. The models are represented in each row
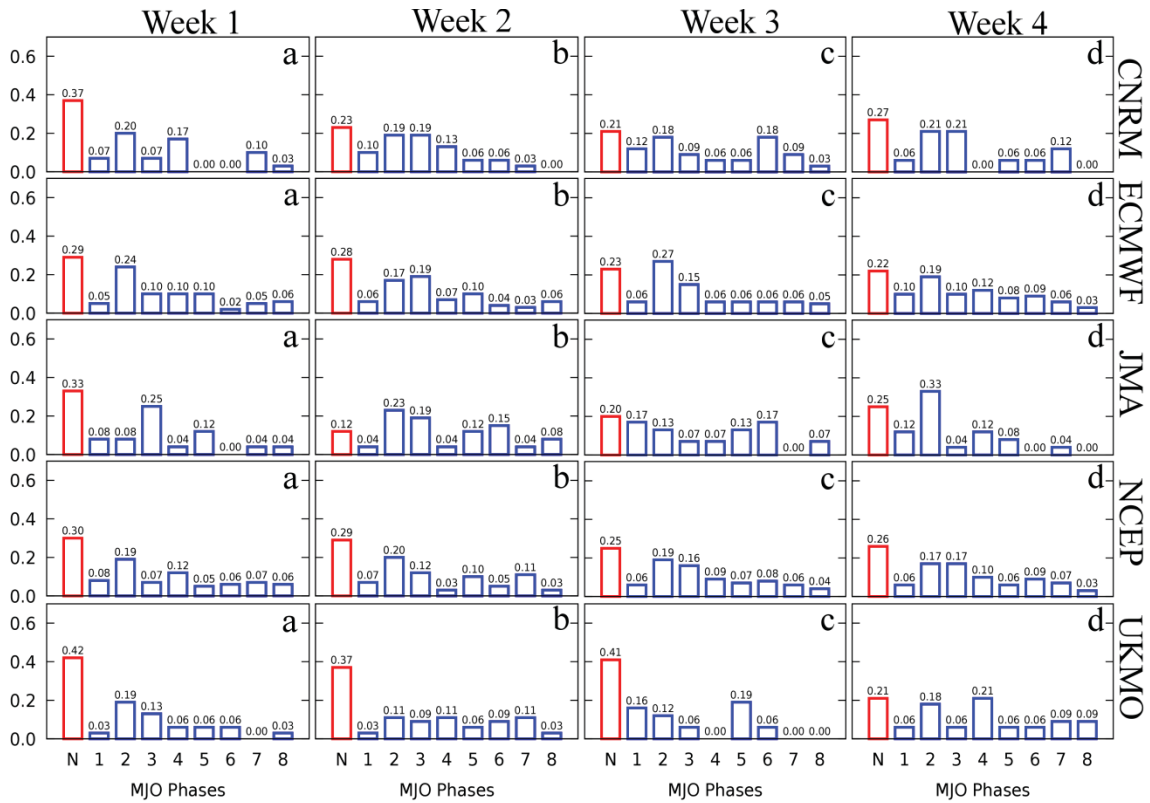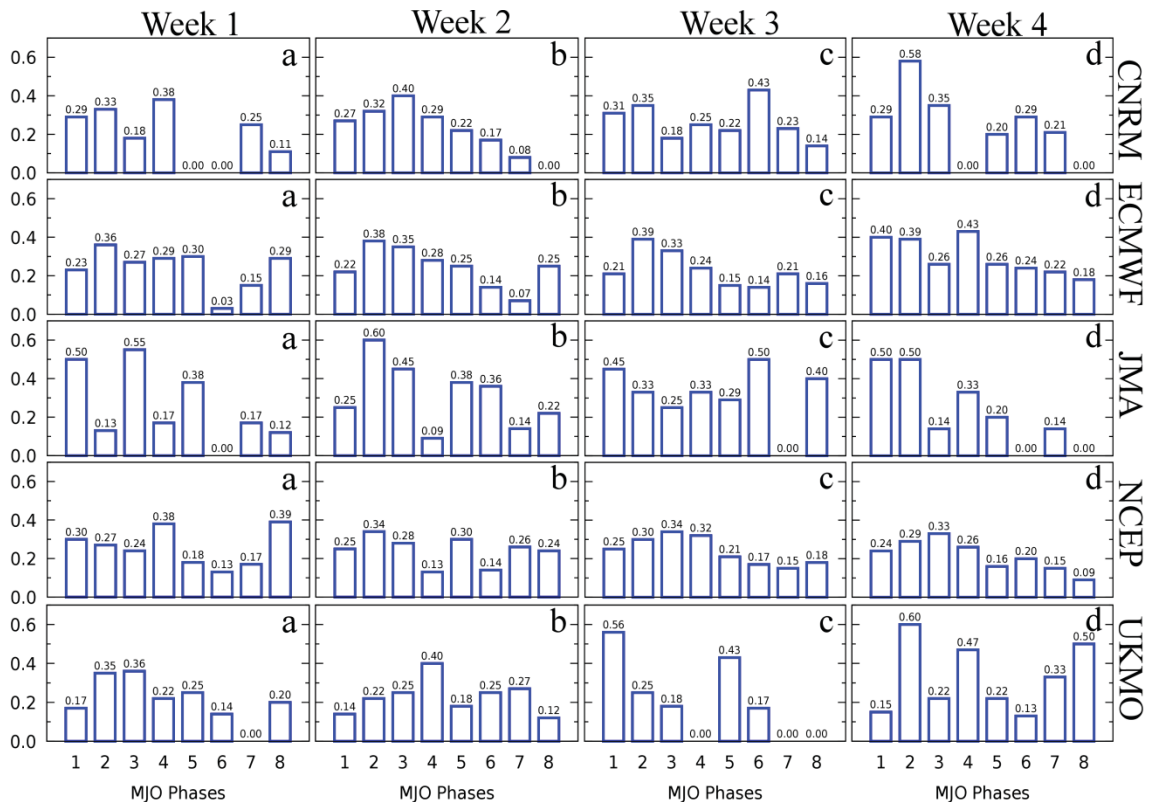

Fig. 9 Same as Fig. 6c, but for models. From left to right are: (a) week 1, (b) week 2, (c) week 3, and (d) week 4. The models are represented in each row
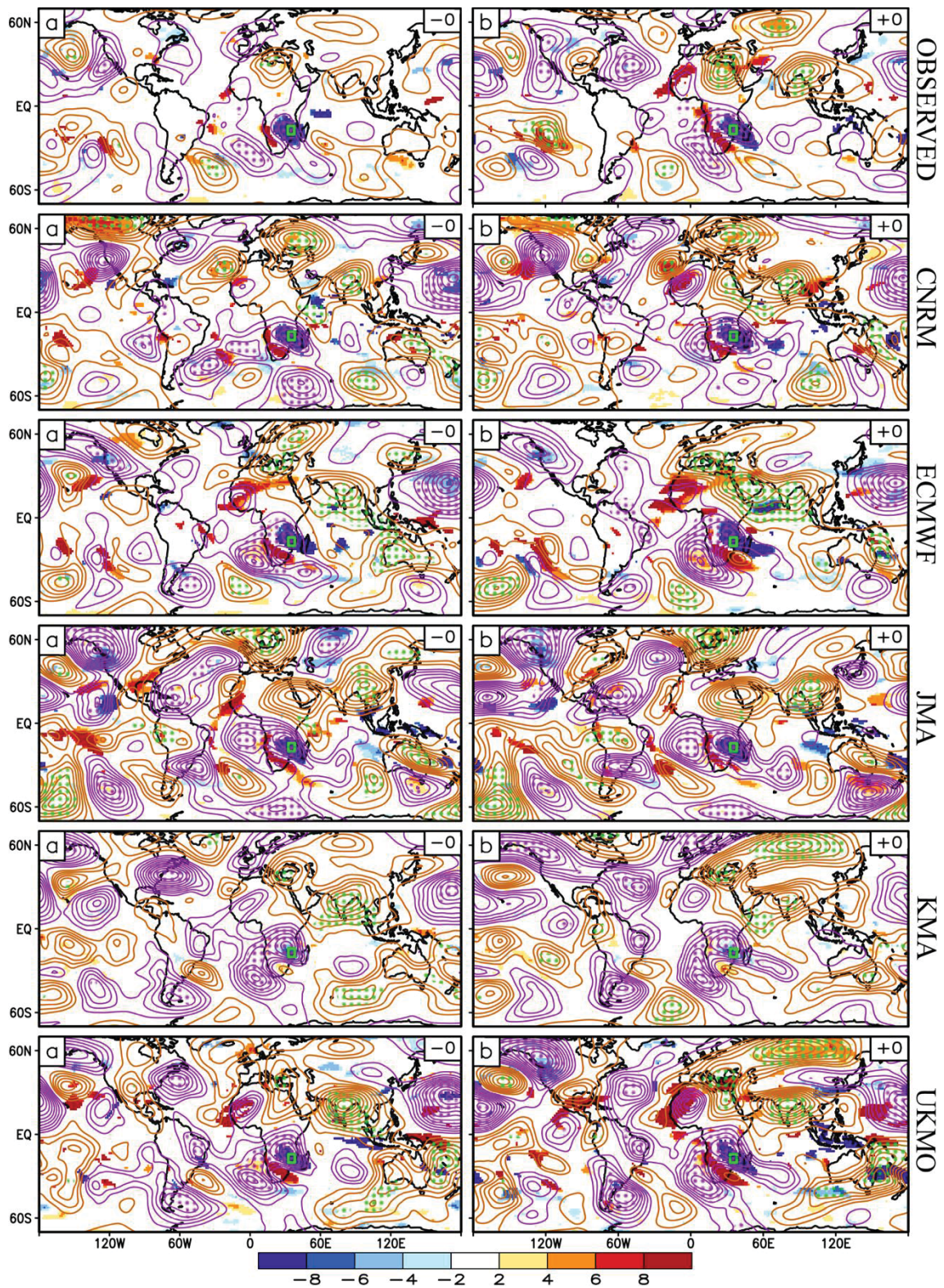
Fig. 10 Difference between anomaly composites for the MPI positive and negative phases for observed data (first row) and models' forecasts for week 1. Contours show 200 hPa eddy streamfunction and shades show either rainfall for KMA model or OLR for other models. The symbol (-0) in the top right corner of each panel (a) indicates the first day of positive phase, while the symbol (+0) indicates the last day of positive phase. Contour interval is 1.0×10^{-6} m^2 s^{-1}, and zero contour is omitted. Dark yellow (purple) contours represent positive (negative) values, with stippled areas indicating anomalies significant with confidence level above 95%. Rainfall (OLR) anomalies are indicated in the bottom colour bar. Only anomalies with confidence level above 95% are shown. In the first row we show the composites for observed data, while in the subsequent rows are the models composites for week 1 lead
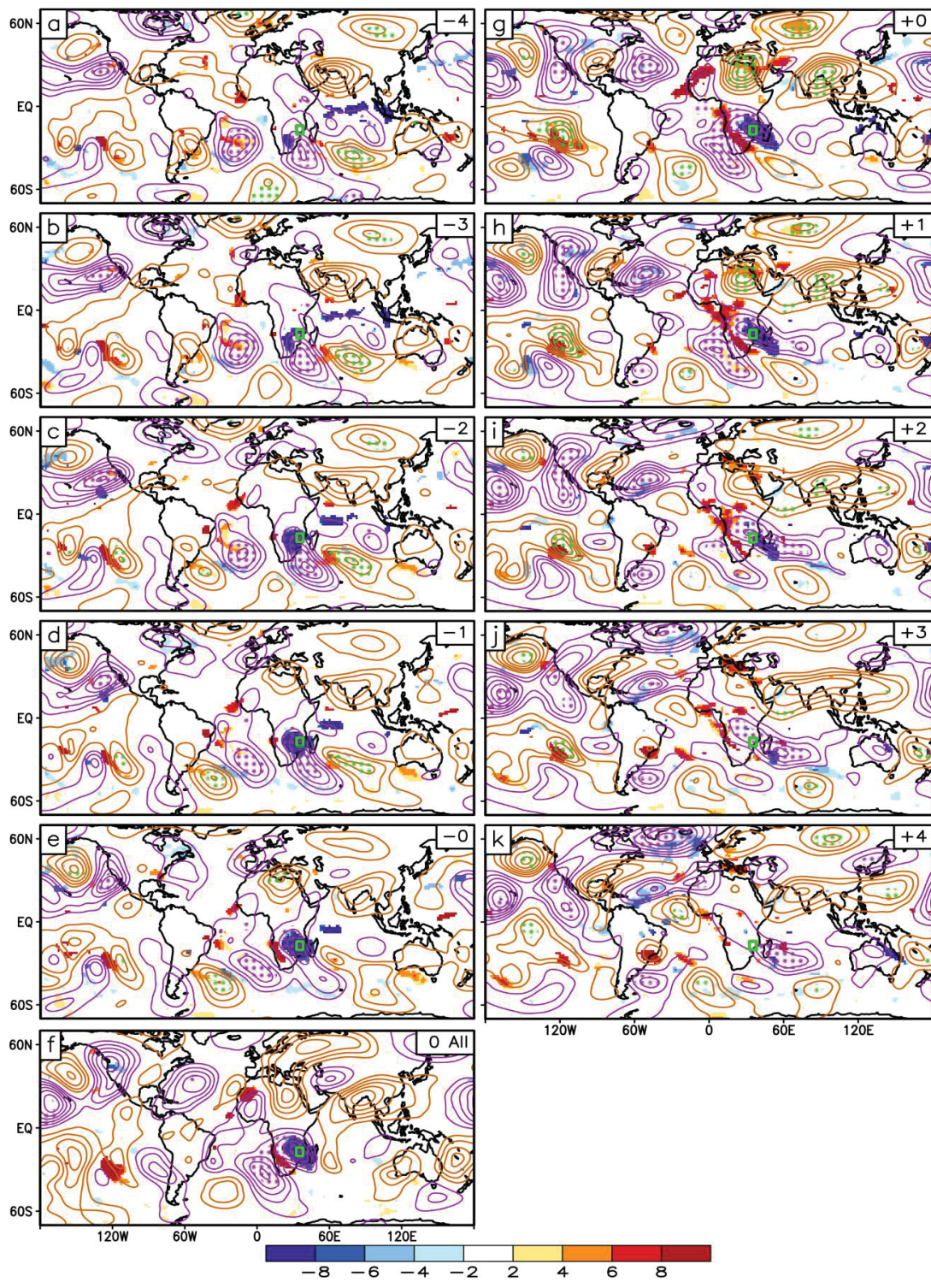
Fig. 11 Differences between observed anomaly composites for the MPI positive and negative phases, showing 200 hPa eddy streamfunction (contours) and OLR (shades). Negative numbers in the top right corner of each panel indicate the number of days before the first day of positive phase (represented by -0), while the positive numbers indicate the number of days after the last day of positive phase (represented by +0), and (0 All) represents the average over all days with positive phase. Contour interval is 1.0×10^{-6} m^2 s^{-1}, and zero contour is omitted. Dark yellow (purple) contours represent positive (negative) values, with stippled areas indicating anomalies significant with confidence level above 95%. OLR anomalies are indicated in the bottom colour bar. Only anomalies with confidence level above 95% are shown.

Fig. 12 Same as Fig. 11, but for NCEP model week 1 forecasts.

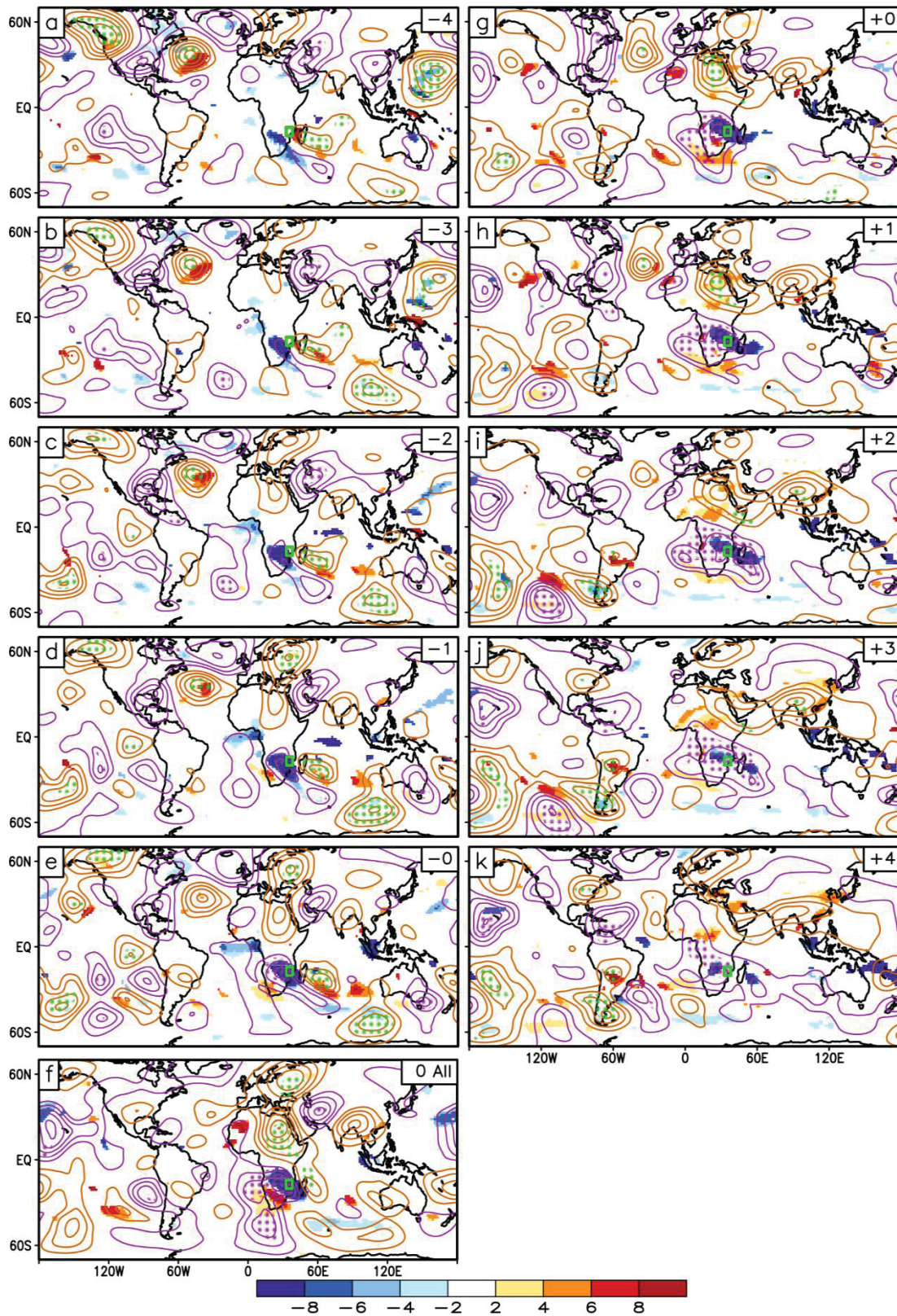## 6. Summary and concluding remarks

Climate variability, defined as the variations around the mean state of climate (either droughts or floods), can strongly impact the lives and economy of any world region including Southern Africa (SAF). Here we examined the variability in SAFM rainfall at intraseasonal timescale as this timescale is of great importance for agricultural production, water resources management, and subseasonal prediction (SG20).

The study was divided in two parts: diagnostic analysis and model assessment, whose results were based on observed (gauge) and models output, respectively. In the first part, gridded gauge daily rainfall anomalies for the period 1979–2005 were used as basic data, while in second part the S2S project models reforecasts for the S2S commom period (1999–2010) were considered as basic data. In both parts, the study concentrated on DJF season, when highest rainfall occurs in SAF.

As our emphasis is on subseasonal (intraseasonal) timescale, in the first part, the rainfall anomalies were submitted to Lanczos band pass filter to retain oscilations in three selected intraseasonal frequency bands (10–25, 10–90 and 20–90 days), for which were separately calculated S-mode Empirical Orthogonal Functions (EOFs) with varimax rotation option, in order to identify the variability modes of precipitation in each frequency band. Different frequency bands were used to analyse the contribution to intraseasonal variability over the study domain.

The EOF analysis revealed 4 most important and similar modes of variability at intraseasonal timescales in all selected bands.

Correlation analysis between timeseries of each retained rotated EOF (REOF) in all three bands and both low-level zonal and meridional wind's components at all SAF grid points shows that enhanced precipitation in all modes (REOFs) is associated with an anomalous cyclonic circulation near the maximum rainfall center. The anomalous circulation related with REOF3 and REOF4 appears to be more associated with variations in monsoon circulation (enhanced NWM, NEM, and even the SETW, besides the MCT), favourable for enhanced monsoon rainfall in the core monsoon region. Furthermore, the spatial patterns (factor loadings) of these two modes together encompass the monsoon core region over SAF (particularly Mozambique). Nonethless, the REOF3 was retained for further analysis, as it represents alone most of

variability in the core monsoon region (MPI box).

As this thesis builds upon the hypothesis that the subseasonal monsoon rainfall anomalies over SAF, particularly, Mozambique are in part modulated by the MJO, a well-known intraseasonal leading mode of tropical variability and the main source for subseasonal predictability, power spectral density (PSD) analysis was applied to 10–90 days (the total ISV) REOF3 time series in order to determine the prevailing periods in this mode, and if there exist periods at MJO frequency band. Results of PSD confirmed the existence of statistically significant MJO related peaks, although they appeared weaker compared to those within the 10–30-days band, suggesting that the latter ones likely contribute more significantly to SAFM rainfall ISV. The most significant oscillations in different ISV frequency bands exhibit periods around 12, 22–24 and 50 days, also found previously in ISV of monsoon rainfall over South America (SA). The 12-day oscillation is associated with the quasi-biweekly oscillation originated from Rossby waves in the extratropical westerly belt propagating into SAF. Lead-lag composite anomalies keyed to positive and negative phases of the 20–90 days REOF3 confirm that a 22–24 days variability mode and the MJO are associated with these oscillations, besides indicating the influence of convective activity over SA on eastward propagating atmospheric waves (tropical and extratropical) to SAF or on waves that originate from subtropical South Pacific that reach SAF. This suggests that the MJO impacts are likely propagated into SAF via teleconnections just described instead being directly produced in the region.

Based on the understanding gained from the climatology and the ISV leading modes, a monsoon precipitation index (MPI) was proposed to help characterizing, monitoring and predicting active and break monsoon days in southern African monsoon domain predominantly over land. Since circulation is better simulated than precipitation by models (MARSHALL and HENDON, 2015), several circulation indices related with MPI was also proposed. Analysis of convection and circulation anaomalies associated with MPI showed that it reflects adequately the monsoon precipitation variability in the core monsoon region over SAF.

In the second part of this study, using the MPI and one of the suggested monsoon circulation indices, the predictive ability of all 11 S2S project models in simulating monsoon active and break periods over SAF for the commom S2S period (1999–2010) is assessed. Although the models can forecast the local large-scale zonal wind anomalies for lead times up to 3 weeks, predictive ability of monsoon rainfall anomalies was found to be limited to a week. The

model's rank showed ECMWF, JMA, UKMO, CNRM, KMA, and NCEP, as the top scoring ones, although they fail in reproducing the MJO impacts on monsoon active periods. It was found that the observed monsoon active periods in the S2S project models are associated with an eastward propagating wave train originating from convective activity over subtropical South Pacific (around 130°E, 35°E) that seems to be modulated by convection over SA and the Atlantic Ocean. All retained models tended to reproduce the convective anomalies associated with observed monsoon active periods, although most of these models failed in reproducing their associated circulation anomalies. This was found to be likely associated with the inherent unpredictability of the extratropical variability and errors related with model deficiencies in representing teleconnections.

Overall, the results derived from this study respond properly the proposed goal of the research, as it not only helped improving our knowledge about the country's intraseasonal climate variability including the neighbouring ones, but it also helped identifying strengths and weaknesses of the S2S models and, consequently, their adequacy for operational forecasting over Mozambique, and other countries in the SAF region, wich can consequently help to minimize the impacts of recurrent weather-climate events in the region.

7. Caveats and recommendations for future studies

The present study was proposed to advance our understanding on variability of regional rainfall at intraseasonal timescale, and assess its prediction by the S2S project models. The emphasis was placed on intraseasonal variability because it is of great importance for agricultural production, water resources management, and subseasonal prediction.

The results revealed four patterns of variability modes at this time scale. The pattern of one of them (20–90 day-band mode) was found to represent well the variability of SAFM, which allowed thus to propose an index (monsoon precipitation index, MPI) to help characterizing, monitoring and predicting active and break monsoon days in southern African monsoon domain predominantly over land. To complement the information represented by MPI, several monsoon circulation indices have been also proposed. Although the models can predict the local large-scale zonal wind anomalies (as represented by circulation index) for lead times up to 3 weeks, predictive ability of monsoon rainfall anomalies was found to be limited to a week.

Nonethless, identifying and acknowledging the study's limitations and making a proposal for further study is an essential part of a research work. In this regard, some limitations of this research study have been identified and recommendations for further research are made.

One limitation to our work was the unavailability of Mozambique gauge data after 2005, as it prevented the extension of the analysis to the most recent period, forcing us to use CPC data as observed data for models verification.

Some recommendations can be made regarding the extension of this work, as follows

i.   With respect to the paper01 in which the rainfall intraseasonal leading modes of variability were obtained using observed (gauge) data for the period 1979–2005, it would be interesting to extend this analysis for all SAF subcontinent using gauge data in order to get a realistic picture of rainfall variability patterns in the region. We are aware of how difficult it is getting data in SAF countries, but the job of colleting them should be initiated. The same is applied for paper02, for which grided data (CPC) for S2S commom period (1999–2010) were used due to unavailability of Mozambique gauge data after 2005 to the authors. Thus, it is recommended to verify in future the possibility of using gauge data for results obtained in paper02.

ii.   Although the region of definition of the MPI also display great synoptic and interannual variability, it would be interesting to verify if this index also represents well the variability for

longer time scales (for example interannual, interdecadal), using preferentially observed (gauge) data. In this case, the index may become more useful, as it will show versatility.

iii. Regarding the retained models, we recommend to verify their performance by considering a multimodel ensemble aproach. This can provide guidance about using either the multimodel ensemble results or the forecast of the best model (e.g., ECMWF).

Finally, we recommend to performe all points above (i, ii, and iii) for all other seasons, particularly, September-November (SON) and March-May (MAM) as the wet season extends from September/October through March/April.

References

ARCHER, E. R. M.; LANDMAN, W. A.; TADROSS, M. A.; et al. Understanding the evolution of the 2014–2016 summer rainfall seasons in southern Africa: Key lessons. **Climate Risk Management**, v. 16, p. 22–28, 2017.

BARCLAY, J. J.; JURY, M. R.; LANDMAN, W. Climatological and structural differences between wet and dry troughs over southern Africa in the early summer. **Meteorology and Atmospheric Physics**, v. 51, n. 1–2, p. 41–54, 1993.

BEHERA, S. K.; YAMAGATA, T. Subtropical SST dipole events in the southern Indian Ocean. **Geophysical Research Letters**, v. 28, n. 2, p. 327–330, 2001.

BLAMEY, R. C.; REASON, C. J. C. Mesoscale convective complexes over Southern Africa. **Journal of Climate**, v. 25, n. 2, p. 753–766, 2012.

BLAMEY, R. C.; REASON, C. J. C. The role of mesoscale convective complexes in southern Africa summer rainfall. **Journal of Climate**, v. 26, n. 5, p. 1654–1668, 2013.

CHEN, M.; SHI, W.; XIE, P.; et al. Assessing objective techniques for gauge-based analyses of global daily precipitation. **Journal of Geophysical Research**, v. 113, n. D4, p. D04110, 2008.

CHREE, C. III. Some phenomena of sunspots and of terrestrial magnetism at Kew Observatory. **Philosophical Transactions of the Royal Society of London. Series A, Containing Papers of a Mathematical or Physical Character**, v. 212, n. 484–496, p. 75–116, 1913.

CHREE, C. VI. Some phenomena of sunspots and of terrestrial magnetism.— Part II. **Philosophical Transactions of the Royal Society of London. Series A, Containing Papers of a Mathematical or Physical Character**, v. 213, n. 497–508, p. 245–277, 1914.

COOK, K. H. The South Indian Convergence Zone and Interannual Rainfall Variability over Southern Africa. **Journal of Climate**, v. 13, n. 21, p. 3789–3804, 2000.

COOK, K. H. A Southern Hemisphere Wave Response to ENSO with Implications for Southern Africa Precipitation. **Journal of the Atmospheric Sciences**, v. 58, n. 15, p. 2146–2162, 2001.

D'ABRETON, P. C. **The dynamics and energetics of tropical-temperature troughs over Southern Africa**, 1992. University of the Witwatersrand, Johannesburg.

DIALLO, I.; GIORGI, F.; STORDAL, F. Influence of Lake Malawi on regional climate from a double-nested regional climate model experiment. **Climate Dynamics**, v. 50, n. 9–10, p. 3397–3411, 2018.

DIEPPOIS, B.; POHL, B.; ROUAULT, M.; et al. Interannual to interdecadal variability of winter and summer southern African rainfall, and their teleconnections. **Journal of Geophysical**

Research: Atmospheres, v. 121, n. 11, p. 6215–6239, 2016.

DUCHON, C. E. Lanczos Filtering in One and Two Dimensions. **Journal of Applied Meteorology**, v. 18, n. 8, p. 1016–1022, 1979.

DYER, T. G. J.; TYSON, P. D. Estimating Above and Below Normal Rainfall Periods over South Africa, 1972–2000. **Journal of Applied Meteorology**, v. 16, n. 2, p. 145–147, 1977.

EHRENDORFER, M. A regionalization of Austria's precipitation climate using principal component analysis. **Journal of Climatology**, v. 7, n. 1, p. 71–89, 1987.

FAUCHEREAU, N.; POHL, B.; REASON, C. J. C.; ROUAULT, M.; RICHARD, Y. Recurrent daily OLR patterns in the Southern Africa/Southwest Indian Ocean region, implications for South African rainfall and teleconnections. **Climate Dynamics**, v. 32, n. 4, p. 575–591, 2009.

GAVRILOV, N. I.; ISAEVA, A. N.; FITOUNI, L. L. **The People's Republic of Mozambique: A Handbook.** Institute ed. Moscow, Russia, 1986.

GRIMM, A. M. Madden–Julian Oscillation impacts on South American summer monsoon season: precipitation anomalies, extreme events, teleconnections, and role in the MJO cycle. **Climate Dynamics**, p. 1–26, 2019.

GRIMM, A. M.; REASON, C. J. C. Does the South American Monsoon Influence African Rainfall? **Journal of Climate**, v. 24, n. 4, p. 1226–1238, 2011.

GRIMM, A. M.; SABOIA, J. P. J. Interdecadal Variability of the South American Precipitation in the Monsoon Season. **Journal of Climate**, v. 28, n. 2, p. 755–775, 2015.

HANNACHI, A.; JOLLIFFE, I. T.; STEPHENSON, D. B. Empirical orthogonal functions and related techniques in atmospheric science: A review. **International Journal of Climatology**, v. 27, n. 9, p. 1119–1152, 2007.

HARRIS, I.; JONES, P. D.; OSBORN, T. J.; LISTER, D. H. Updated high-resolution grids of monthly climatic observations - the CRU TS3.10 Dataset. **International Journal of Climatology**, v. 34, n. 3, p. 623–642, 2014. John Wiley & Sons, Ltd.

HARRISON, M. S. J. The Annual Rainfall Cycle Over the Central Interior of South Africa. **South African Geographical Journal**, v. 66, n. 1, p. 47–64, 1984a. Taylor & Francis Group.

HARRISON, M. S. J. A generalized classification of South African summer rain-bearing synoptic systems. **Journal of Climatology**, v. 4, n. 5, p. 547–560, 1984b.

HART, N. C. G.; REASON, C. J. C.; FAUCHEREAU, N. Tropical–Extratropical Interactions over Southern Africa: Three Cases of Heavy Summer Season Rainfall. **Monthly Weather Review**, v. 138, n. 7, p. 2608–2623, 2010.

HART, N. C. G.; REASON, C. J. C.; FAUCHEREAU, N. Cloud bands over southern Africa: seasonality, contribution to rainfall variability and modulation by the MJO. **Climate Dynamics**, v. 41, n. 5–6, p. 1199–1212, 2013.

HELD, I. M.; TING, M.; WANG, H. Northern Winter Stationary Waves: Theory and Modeling. **Journal of Climate**, v. 15, n. 16, p. 2125–2144, 2002.

HERMES, J. C.; REASON, C. J. C. Variability in sea-surface temperature and winds in the tropical south-east Atlantic Ocean and regional rainfall relationships. **International Journal of Climatology**, v. 29, n. 1, p. 11–21, 2009.

HOELL, A.; FUNK, C.; MAGADZIRE, T.; ZINKE, J.; HUSAK, G. El Niño–Southern Oscillation diversity and Southern Africa teleconnections during Austral Summer. **Climate Dynamics**, v. 45, n. 5–6, p. 1583–1599, 2015.

HOELL, A.; FUNK, C.; ZINKE, J.; HARRISON, L. Modulation of the Southern Africa precipitation response to the El Niño Southern Oscillation by the subtropical Indian Ocean Dipole. **Climate Dynamics**, v. 48, n. 7–8, p. 2529–2540, 2017.

HOTELLING, H. Analysis of a complex of statistical variables into principal components. **Journal of Educational Psychology**, v. 24, n. 6, p. 417–441, 1933.

HSU, H.-H.; LIN, S.-H. Global Teleconnections in the 250-mb Streamfunction Field during the Northern Hemisphere Winter. **Monthly Weather Review**, v. 120, n. 7, p. 1169–1190, 1992.

INAM. Informação Sobre a Situação Meteorológica Nacional. Disponível em: <https://www.fac ebook.com/meteo.maputo/>. Acesso em: 26/4/2019.

INE. Resultados definitivos do IV Recenseamento Geral da População e Habitação de 2017 (Censo 2017). Disponível em: <http://www.ine.gov.mz/>. Acesso em: 4/5/2019.

INGC. Ponto de Situação: Ciclone IDAI (Dados preliminares até 12 de Abril de 2019). Disponível em: <https://www.facebook.com/INGC.Mocambique/photos/a.304579886870732/32 8819124446808/?type=3&theater>. Acesso em: 20/4/2019.

JACKSON, S. P. Climates of Southern Africa. **South African Geographical Journal**, v. 33, n. 1, p. 17–37, 1951.

JOLLIFFE, I. T.; CADIMA, J. Principal component analysis: a review and recent developments. **Philosophical transactions. Series A, Mathematical, physical, and engineering sciences**, v. 374, n. 2065, p. 20150202, 2016. The Royal Society.

JURY, M. R. Inter-annual climate modes over southern Africa from satellite cloud OLR 1975?1994. **Theoretical and Applied Climatology**, v. 57, n. 3–4, p. 155–163, 1997.

KAISER, H. F. The varimax criterion for analytic rotation in factor analysis. **Psychometrika**, v.

23, n. 3, p. 187–200, 1958. Springer-Verlag.

KALNAY, E.; KANAMITSU, M.; KISTLER, R.; et al. The NCEP/NCAR 40-Year Reanalysis Project. **Bulletin of the American Meteorological Society**, v. 77, n. 3, p. 437–471, 1996.

KIM, G.; AHN, J. B.; KRYJOV, V. N.; et al. Global and regional skill of the seasonal predictions by WMO Lead Centre for Long-Range Forecast Multi-Model Ensemble. **International Journal of Climatology**, v. 36, n. 4, p. 1657–1675, 2016.

LEVEY, K. M.; JURY, M. R. Composite Intraseasonal Oscillations of Convection over Southern Africa. **Journal of Climate**, v. 9, n. 8, p. 1910–1920, 1996.

LI, L.; DIALLO, I.; XU, C. Y.; STORDAL, F. Hydrological projections under climate change in the near future by RegCM4 in Southern Africa using a large-scale hydrological model. **Journal of Hydrology**, 2015.

LIEBMANN, B.; ALLURED, D. Daily Precipitation Grids for South America. **Bulletin of the American Meteorological Society**, v. 86, n. 11, p. 1567–1570, 2005.

LIEBMANN, B.; SMITH, C. A. Description of a Complete (Interpolated) Outgoing Longwave Radiation Dataset. **Bulletin of the American Meteorological Society**, 1996.

LINDESAY, J. A.; JURY, M. R. Atmospheric circulation controls and characteristics of a flood event in central South Africa. **International Journal of Climatology**, v. 11, n. 6, p. 609–627, 1991.

VAN LOON, H. A half-yearly variation of the circumpolar surface drift in the Southern Hemisphere. **Tellus**, v. 23, n. 6, p. 511–516, 1971. Informa UK Limited.

LORENZ, E. N. **Empirical orthogonal functions and statistical weather prediction. Statistical Forecasting Project**. Cambridge, Massachusetts, 1956.

LYON, B.; MASON, S. J. The 1997–98 Summer Rainfall Season in Southern Africa. Part I: Observations. **Journal of Climate**, v. 20, n. 20, p. 5134–5148, 2007.

MABHAUDHI, T.; MPANDELI, S.; MADHLOPA, A.; et al. Southern Africa's Water–Energy Nexus: Towards Regional Integration and Development. **Water**, v. 8, n. 6, p. 235, 2016.

MACAMBACO, M. P. **Climate variations in southeastern Africa (SEA) and their possible teleconnections with South America (SA).**, 2016. Master Thesis at Federal University of Parana.

MACRON, C.; POHL, B.; RICHARD, Y.; BESSAFI, M. How do tropical temperate troughs form and develop over Southern Africa? **Journal of Climate**, v. 27, n. 4, p. 1633–1647, 2014.

MACRON, C.; RICHARD, Y.; GAROT, T.; et al. Intraseasonal Rainfall Variability over

Madagascar. **Monthly Weather Review**, v. 144, n. 5, p. 1877–1885, 2016.

MADDEN, R. A.; JULIAN, P. R. Detection of a 40–50 Day Oscillation in the Zonal Wind in the Tropical Pacific. **Journal of the Atmospheric Sciences**, v. 28, n. 5, p. 702–708, 1971.

MAKARAU, A. **Intra-seasonal oscillatory modes of the southern Africa summer circulation**, 1995. UCT.

MAKARAU, A.; JURY, M. R. Seasonal cycle of convective spells over southern Africa during austral summer. **International Journal of Climatology**, v. 17, n. 12, p. 1317–1332, 1997.

MANATSA, D.; MATARIRA, C. H.; MUKWADA, G. Relative impacts of ENSO and Indian Ocean dipole/zonal mode on east SADC rainfall. **International Journal of Climatology**, v. 31, n. 4, p. 558–577, 2011.

MANHIQUE, A. J. **The South Indian Convergence Zone and relationship with rainfall variability in Mozambique**, 2008. University of Cape Town.

MANHIQUE, A. J.; REASON, C. J. C.; SILINTO, B.; et al. Extreme rainfall and floods in southern Africa in January 2013 and associated circulation patterns. **Natural Hazards**, v. 77, n. 2, p. 679–691, 2015.

MARSHALL, A.G.; HENDON, H. H. Subseasonal prediction of Australian summer monsoon anomalies. **Geophys Res Lett**, v. 42, n. 24, p. 10,913–10,919, 2015

MASON, S. J. South African Journal of Science - Temporal variability of sea surface temperatures around Southern Africa: a possible forcing mechanism for the 18-year rainfall oscillation? **South African Journal of Science**, v. 86, n. 5–6, p. 243–252, 1990.

MASON, S. J.; JOUBERT, A. M.; COSIJN, C.; CRIMP, S. . Review of seasonal forecasting techniques and their applicability to Southern Africa. **Water SA**, v. 22, n. 3, p. 203–209, 1996.

MASON, S. J.; JURY, M. R. Climatic variability and change over southern Africa: a reflection on underlying processes. **Progress in Physical Geography**, v. 21, n. 1, p. 23–50, 1997.

MCHUGH, M. J.; ROGERS, J. C. North Atlantic Oscillation Influence on Precipitation Variability around the Southeast African Convergence Zone. **Journal of Climate**, v. 14, n. 17, p. 3631–3642, 2001.

MEIJERING, E. A chronology of interpolation: from ancient astronomy to modern signal and image processing. **Proceedings of the IEEE**, v. 90, n. 3, p. 319–342, 2002.

MITCHELL, J. J. M.; AND DZERDZEEVSKII, B.; AND FLOHN, H.; et al. **Climatic change: report of a working group of the Commission for Climatology. WMO technical note No. 79**. Geneva, Switzerland: WMO, 1966.

NICHOLSON, S. E. The nature of rainfall variability over Africa on time scales of decades to millenia. **Global and Planetary Change**, v. 26, n. 1–3, p. 137–158, 2000.

NICHOLSON, S. E.; KIM, J. The relationship of the el Niño–Southern Oscillation to African rainfall. **International Journal of Climatology**, v. 17, n. 2, p. 117–135, 1997.

NICHOLSON, S. E.; KLOTTER, D.; CHAVULA, G. A detailed rainfall climatology for Malawi, Southern Africa. **International Journal of Climatology**, v. 34, n. 2, p. 315–325, 2014.

OCHA. **The 2014/2015 Southern Africa Flood Season. Issue 18. May 2015**. South Africa, 2015.

OETTLI, P.; TOZUKA, T.; IZUMO, T.; ENGELBRECHT, F. A.; YAMAGATA, T. The self-organizing map, a new approach to apprehend the Madden–Julian Oscillation influence on the intraseasonal variability of rainfall in the southern African region. **Climate Dynamics**, v. 43, n. 5–6, p. 1557–1573, 2014.

PEARSON, K. LIII. On lines and planes of closest fit to systems of points in space. **The London, Edinburgh, and Dublin Philosophical Magazine and Journal of Science**, v. 2, n. 11, p. 559–572, 1901. Informa UK Limited.

PINTO, I.; LENNARD, C.; TADROSS, M.; et al. Evaluation and projections of extreme precipitation over southern Africa from two CORDEX models. **Climatic Change**, v. 135, n. 3–4, p. 655–668, 2016. Springer Netherlands.

POHL, B.; DIEPPOIS, B.; CRÉTAT, J.; LAWLER, D.; ROUAULT, M.; et al. From Synoptic to Interdecadal Variability in Southern African Rainfall: Toward a Unified View across Time Scales. **Journal of Climate**, v. 31, n. 15, p. 5845–5872, 2018.

POHL, B.; FAUCHEREAU, N.; RICHARD, Y.; ROUAULT, M.; REASON, C. J. C. Interactions between synoptic, intraseasonal and interannual convective variability over Southern Africa. **Climate Dynamics**, v. 33, n. 7–8, p. 1033–1050, 2009.

POHL, B.; RICHARD, Y.; FAUCHEREAU, N.; et al. Influence of the Madden–Julian Oscillation on Southern African Summer Rainfall. **Journal of Climate**, v. 20, n. 16, p. 4227–4242, 2007.

RAMAGE, C. S. **Monsoon meteorology**. New York: Academic Press, 1971.

REASON, C. J .; LANDMAN, W.; TENNANT, W. Seasonal to Decadal Prediction of Southern African Climate and Its Links with Variability of the Atlantic Ocean. **Bulletin of the American Meteorological Society**, v. 87, n. 7, p. 941–956, 2006. American Meteorological Society.

REASON, C. J. C. Warm and cold events in the southeast Atlantic/southwest Indian Ocean region and potential impacts on circulation and rainfall over southern Africa. **Meteorology and Atmospheric Physics**, v. 69, n. 1–2, p. 49–65, 1998. Springer Wien.

REASON, C. J. C. Subtropical Indian Ocean SST dipole events and southern African rainfall. **Geophysical Research Letters**, v. 28, n. 11, p. 2225–2227, 2001.

REASON, C. J. C. Sensitivity of the southern African circulation to dipole sea-surface temperature patterns in the south Indian Ocean. **International Journal of Climatology**, v. 22, n. 4, p. 377–393, 2002.

REASON, C. J. C.; ALLAN, R. J.; LINDESAY, J. A.; ANSELL, T. J. ENSO and climatic signals across the Indian Ocean Basin in the global context: part I, interannual composite patterns. **International Journal of Climatology**, v. 20, n. 11, p. 1285–1327, 2000.

REASON, C. J. C. AND; KEIBEL, A. Tropical Cyclone Eline and Its Unusual Penetration and Impacts over the Southern African Mainland. **Weather and Forecasting**, v. 19, p. 789–805, 2004.

REASON, C. J. C.; JAGADHEESHA, D. A model investigation of recent ENSO impacts over southern Africa. **Meteorology and Atmospheric Physics**, v. 89, n. 1–4, p. 181–205, 2005.

REASON, C. J. C.; MULENGA, H. Relationships between South African rainfall and SST anomalies in the Southwest Indian Ocean. **International Journal of Climatology**, v. 19, n. 15, p. 1651–1673, 1999.

REASON, C. J. C.; ROUAULT, M. ENSO-like decadal variability and South African rainfall. **Geophysical Research Letters**, v. 29, n. 13, p. 1638, 2002. John Wiley & Sons, Ltd.

REASON, C. J. C.; SMART, S. Tropical south east Atlantic warm events and associated rainfall anomalies over Southern Africa. **Frontiers in Environmental Science**, v. 3, n. MAY, 2015.

RICHARD, Y.; FAUCHEREAU, N.; POCCARD, I.; ROUAULT, M.; TRZASKA, S. 20th century droughts in southern Africa: spatial and temporal variability, teleconnections with oceanic and atmospheric conditions. **International Journal of Climatology**, v. 21, n. 7, p. 873–885, 2001.

RICHARD, Y.; TRZASKA, S.; ROUCOU, P.; ROUAULT, M. Modification of the southern African rainfall variability/ENSO relationship since the late 1960s. **Climate Dynamics**, v. 16, n. 12, p. 883–895, 2000.

RICHMAN, M. B. Rotation of principal components. **Journal of Climatology**, v. 6, n. 3, p. 293–335, 1986.

ROBERTSON, A. W.; CAMARGO, S. J.; SOBEL, A.; VITART, F.; WANG, S. Summary of workshop on sub-seasonal to seasonal predictability of extreme weather and climate. **npj Climate and Atmospheric Science**, v. 1, n. 1, p. 20178, 2018. Nature Publishing Group.

SABOIA, J. P. J. **Variabilidade interdecadal de precipitação na América do Sul**, 2010. Master thesis at Federal University of Paraná.

SCHNEIDER, U.; ZIESE, M.; MEYER-CHRISTOFFER, A.; et al. The new portfolio of global precipitation data products of the Global Precipitation Climatology Centre suitable to assess and quantify the global water cycle and resources. **Proceedings of the International Association of Hydrological Sciences**, v. 374, p. 29–34, 2016.

SILVA, W. P. DA. **Climate variability on hydrological time series: identification, origins and contribution to extreme events**, mar. 2018. Curitiba-Paraná, Brazil: Master thesis at Federal University of Paraná (UFPR).

SILVÉRIO, K. C.; GRIMM, A. M. Southern Africa monsoon: Intraseasonal variability and monsoon indices. **Climate Dynamics**, 2020.

TALJAARD, J. J. Change of rainfall distribution and circulation patterns over Southern Africa in summer. **Journal of Climatology**, v. 6, n. 6, p. 579–592, 1986.

TODD, M. C.; WASHINGTON, R.; PALMER, P. I. Water vapour transport associated with tropical-temperate trough systems over southern Africa and the southwest Indian Ocean. **International Journal of Climatology**, v. 24, n. 5, p. 555–568, 2004.

TORRANCE, J. D. Malawi, Rhodesia and Zambia. In: J. F. Griffiths (Org.); **Climates of Africa. World Survey of Climatology, Vol. 10**. p.409–460, 1972. Amsterdam, Netherlands: Elsevier.

TYSON, P. D. Atmospheric circulation variations and the occurrence of extended wet and dry spells over Southern Africa. **Journal of Climatology**, v. 1, n. 2, p. 115–130, 1981.

TYSON, P. D.; PRESTON-WHYTE, R. A. **The weather and climate of southern Africa**. 2. ed. ed. Cape Town; Oxford: Oxford University Press, 2000.

VITART, F. **The Sub-seasonal to Seasonal (S2S) Prediction Project "Bridging the gap between weather and climate"**. Pretoria, South Africa, 2016.

VITART, F.; ARDILOUZE, C.; BONET, A.; et al. The Subseasonal to Seasonal (S2S) Prediction Project Database. **Bulletin of the American Meteorological Society**, v. 98, n. 1, p. 163–173, 2017.

VITART, F.; ROBERTSON, A. W. The sub-seasonal to seasonal prediction project (S2S) and the prediction of extreme events. **npj Climate and Atmospheric Science**, v. 1, n. 1, p. 3, 2018.

WALKER, J. A.; LINDESAY, N. D. Preliminary observations of oceanic influences on the February March 1988 floods in central South Africa. **South African Journal of Science**, v. 85, n. 3, p. 164–169, 1989.

WANG, B.; DING, Q. Global monsoon: Dominant mode of annual variation in the tropics. **Dynamics of Atmospheres and Oceans**, v. 44, n. 3–4, p. 165–183, 2008.

WANG, B.; LIU, J.; KIM, H.-J.; WEBSTER, P. J.; YIM, S.-Y. Recent change of the global monsoon precipitation (1979–2008). **Climate Dynamics**, v. 39, n. 5, p. 1123–1135, 2012.

WASHINGTON, R.; PRESTON, A. Extreme wet years over southern Africa: Role of Indian Ocean sea surface temperatures. **Journal of Geophysical Research Atmospheres**, v. 111, n. 15, p. 1–15, 2006.

WASHINGTON, R.; TODD, M. Tropical-temperate links in southern African and Southwest Indian Ocean satellite-derived daily rainfall. **International Journal of Climatology**, v. 19, n. 14, p. 1601–1616, 1999.

WEBSTER, P. J.; MAGAÑA, V. O.; PALMER, T. N.; et al. Monsoons: Processes, predictability, and the prospects for prediction. **Journal of Geophysical Research: Oceans**, v. 103, n. C7, p. 14451–14510, 1998. John Wiley & Sons, Ltd.

WHITE, C. J.; FRANKS, S. W.; MCEVOY, D. Using subseasonal-to-seasonal (S2S) extreme rainfall forecasts for extended-range flood prediction in Australia. **Proceedings of the International Association of Hydrological Sciences**, v. 370, p. 229–234, 2015.

WILKS, D. S. **Statistical methods in the atmospheric sciences**. 3rd ed. AMSTERDAM: Academic Press, 2011.

XIE, Z.; DUAN, A.; TIAN, Q. Weighted composite analysis and its application: an example using ENSO and geopotential height. **Atmospheric Science Letters**, v. 18, n. 11, p. 435–440, 2017.

YIM, S.-Y.; WANG, B.; LIU, J.; WU, Z. A comparison of regional monsoon variability using monsoon indices. **Climate Dynamics**, v. 43, n. 5–6, p. 1423–1437, 2014.

ZAITCHIK, B. F. Madden-Julian Oscillation impacts on tropical African precipitation. **Atmospheric Research**, v. 184, p. 88–102, 2017. Elsevier.

ZHANG, C. Madden–Julian Oscillation: Bridging Weather and Climate. **Bulletin of the American Meteorological Society**, v. 94, n. 12, p. 1849–1870, 2013.

ZHANG, S.; WANG, B. Global summer monsoon rainy seasons. **International Journal of Climatology**, v. 28, n. 12, p. 1563–1578, 2008. John Wiley & Sons, Ltd.

ZHISHENG, A.; GUOXIONG, W.; JIANPING, L.; et al. Global Monsoon Dynamics and Climate Change. **Annual Review of Earth and Planetary Sciences**, v. 43, n. 1, p. 29–77, 2015.

ZHOU, J.; LAU, K.-M. Does a Monsoon Climate Exist over South America? **Journal of Climate**, v. 11, n. 5, p. 1020–1040, 1998.